Frequency-dependent coupling in responses to oscillatory inputs in networks of electrically coupled nodes: Gap junction networks and spatially extended neurons

Andrea Bel [1], Ulises Chialva[1], Horacio G. Rotstein [2 *†]

[1] Departamento de Matemática,
Universidad Nacional del Sur (UNS) and CONICET
Bahía Blanca, Argentina
[2] Federated Department of Biological Sciences
New Jersey Institute of Technology and Rutgers University
Newark, NJ, USA

September 12, 2025

Abstract

Neuronal filters describe the neuronal information processing building blocks where specific frequency components of the output are enhanced over others. The result of the interaction of neuronal filters across nodes in a network is captured by the frequency-dependent amplitude and phase-difference coupling coefficients (CCs), respectively, which extend the notion of the steady-state CC to include frequency-dependent processes. These metrics are shaped by the interplay of the participating ionic and synaptic currents and the external inputs. The underlying biophysical and dynamic mechanisms are largely unknown beyond electrically coupled passive cells. In this paper, we investigate the mechanism of interaction of cellular neuronal filters in electrically coupled networks. We use biophysically plausible (conductance-based) mathematical modeling, numerical simulations, analytical calculations and dynamical systems tools. We focus on a family of models that include gap junction connected cells and compartmental models of spatially extended neurons. We consider a network of two electrically connected nodes receiving oscillatory inputs. This is the minimal network architecture that allows for a systematic study of the biophysical and dynamic mechanisms that shape the CC profiles. The participating neurons are either passive cells (low-pass filters) or resonators (band-pass filter) and exhibit lagging or mixed leading-lagging phase-shift responses as the input frequency increases. First, we use linear models to understand how the participating building blocks (e.g., conductances, negative and positive feedback effects) operating at the single node level give rise to the amplitude and phase CC profiles with band-pass filtering properties. Then, we extend our investigation and use linearized models of nonlinear of neurons with biophysically realistic ionic currents to investigate (to the linear level of approximation) how the presence of cellular ionic currents and cellular resonance/phasonance contribute to shaping the corresponding (amplitude and phase) CC profiles and determine their preferred coupling frequencies. Motivated by experimental results on subthreshold resonance in hippocampal CA1 pyramidal cells, we use three ionic currents: persistent sodium (amplifying), mixed sodium-potassium h- (resonant and hyperpolarization-activated) and M-type slow potassium (resonant and depolarization-activated). Finally, we extend our investigation to include the model nonlinearities to understand how the CC profiles are shaped by the interaction between the pre-J and post-J cells, and not just the post-J cells as it is the case for linear models. For gap junction connected networks, the connectivity is typically symmetric, while for compartmental models is asymmetric as the result of the different geometries of the participating

*Graduate Faculty, Graduate Program in Neuroscience (GPN), Center for Molecular and Behavioral Neuroscience (CMBN), Rutgers University.
†Corresponding Researcher, CONICET, Argentina.

compartments. We investigate the effects of asymmetric connectivity to understand how the compartmental geometry interacts with the neuronal biophysical properties to shape the CC profiles and determine the preferred coupling frequencies. The formalism and tools we develop and use in this paper can be extended to larger networks with an arbitrary number of nodes, to spatially extended multicompartment neuronal models, and to neurons having other types of ionic currents such as the T-type calcium current. The principles that emerge from our study are directly applicable to these scenarios. Our results make experimentally testable predictions and have implications for the understanding of spike transmission, synchronic firing and coincidence detection in electrically coupled networks in the presence of oscillatory inputs.

1 Introduction

Neuronal circuits are impacted by external inputs that often have oscillatory components spanning a range of frequencies (f). The frequency-dependent output is shaped by the complex interaction between the input and the cellular and synaptic properties. Neuronal filters describe the information processing building blocks where specific frequency components of the output are enhanced over others [1–6]. Therefore neuronal filters play a crucial role in shaping neuronal communication and how the brain process information, generates rhythmic activity and performs complex computations [3, 4, 7–18].

In this paper we investigate the mechanism of interaction of cellular neuronal filters in electrically coupled networks. We use biophysically plausible (conductance-based) mathematical modeling, numerical simulations, analytical calculations and dynamical systems tools. We focus on gap junction connected cells and compartmental models of spatially extended neurons. While, biologically, these are different objects, they belong to the same family of mathematical models of electrically coupled nodes that express neuronal amplitude and phase filters and are subject to inputs with frequency components within certain range, and therefore can be investigated within the same framework.

Two of the most common types of neuronal filters are low-pass (LPFs; e.g., Figs. 1-A1, -B1) and band-pass (BPFs; e.g., Figs. 1-A2, -B2) filters. BPFs are closely linked to the concept of neuronal resonance [1, 4, 19], defined as the ability of a neuronal system to exhibit a maximal response (e.g., subthreshold membrane potential) to periodic inputs at a preferred (resonant), non-zero frequency (or frequency band). In contrast, LPFs describe a preference for inputs in the lowest frequency band. The associated frequency-dependent phase (phase-shift) profiles can be entirely positive (e.g., Figs. 1-C1), indicating a lagging response for all input frequencies, or transition from negative to positive as the input frequency increases (e.g., Figs. 1-C2), indicating a mixed leading-lagging response and exhibiting phasonance at the (nonzero) frequency at which the phase vanishes. In both cases, the phase monotonically increases for frequencies above the phasonant frequency. Resonance and phasonance are related phenomena, and when they coexist, the resonant and phasonant frequency do not necessarily coincide [20, 21].

Electrical synapses mediated by gap junctions are ubiquitous in the nervous system and coexist with chemical (excitatory and inhibitory) synapses [22–34]. The metric usually used to characterize the strength of electrical synapses is the coupling coefficient (CC) $K = \Delta V_2/\Delta V_1$ [23–26, 28, 35–44, 44]. It is measured by injecting a step current into one cell and computing the ratio of the steady state voltage deflections of the indirectly (ΔV_2; post-J) and directly (ΔV_1; pre-J) stimulated cells. The larger K, the stronger the degree to which the pre-J and post-J cells are electrically coupled. Note that in this context (Fig. 2), we used the terms pre-J and post-J cells although electrical transmission mediated by gap junctions is reciprocal [40].

The magnitude of the CC is determined by the electrical connectivity and the cellular properties and can be altered by neuromodulators and additional synaptic inputs that affect the components of the CC [43, 45]. To the linear level of description, K varies between 0 to 1, increases monotonically with the gap junction conductance (g_c) and decreases monotonically with the post-J membrane (g_L) and ionic conductances (g_2) (e.g., in passive cells supplemented with a positive or negative feedback terms). These dependences occur in a balanced, homeostatic manner on the combined parameters g_L/g_c and g_2/g_c. This characterization determines the efficiency of electrical transmission for heterogeneous network and establishes a path in the flow of information in gap junction connected networks. Electrical transmission is more efficient from the higher to the lower conductances as compared to the reverse direction.

The analysis of more realistic scenarios involving time-dependent inputs and the effects of the intrinsic cellular time constants requires the extending the notion of CC to include the response of gap junction networks (electrically coupled networks mediated by gap junctions) to oscillatory inputs [24,32,40,43]. This leads to the frequency-dependent (amplitude) coupling and phase-difference coefficient profiles defined as $K(f) = A_2(f)/A_1(f)$ and the $\Delta\Phi(f) = \Phi_2(f) - \Phi_1(f)$, respectively, where $A_{1/2}(f)$ and $\Phi_{1/2}(f)$ are the amplitude and phase profiles of the pre-J and post-J cells (described in detail in Section 2.6.1). For more complex signals, this definition can be further extended to be the quotient of the (complex) Fourier transforms of the post-J and pre-J responses. For passive cells, the $K(f)$ profile are LPFs [23–29, 36, 40, 41, 46–50], indicating that the signal transmission is more efficient and the coupling is stronger for the slower than for the faster membrane potential fluctuations. The $\Delta\Phi$ profile are positive and monotonically increasing. These two profiles depend on a combination of the intrinsic cellular properties and the gap junction connectivity.

Theoretical studies have mainly focused on models based on linear circuit theory. For linear systems, $K(f)$ and $\Delta\Phi(f)$ depend on the biophysical properties of the post-J cell and the gap junction conductance, and are independent of the biophysical properties of the pre-J and the input amplitude [43] (revisited in Section 3.1.1). Furthermore, modeling studies have largely used passive cell models (but see [32,43,49,51–53]). Being linear and one-dimensional, the $K(f)$ and $\Delta\Phi(f)$ profiles for electrically coupled passive cells are a modulated version of the corresponding response profiles for the post-J cell and therefore remain LPFs(K) and positive ($\Delta\Phi$), respectively.

However, neurons possess a variety of ionic currents that are inherently nonlinear and their dynamics involve a multiplicity of time scales. It is largely unknown how the $K(f)$ and $\Delta\Phi(f)$ profiles are shaped by the participating building blocks when the above mentioned assumptions are relaxed (but see [43]). It is unclear how the properties of the pre-J cell and the input amplitude affect the $K(f)$ and $\Delta\Phi(f)$ profiles (in addition to the properties of the post-J cell and the gap junction conductance) when the neurons operate away from the linear regime.

The generation of cellular resonance and phasonance in individual cells requires the interplay of negative and positive feedback effects mediated by the gating variables associated to the intrinsic slow resonant currents (e.g., hyperpolarization-activated mixed-cation I_h, M-type slow potassium I_M and T-type calcium I_{CaT} inactivation) and fast amplifying currents (e.g., persistent sodium I_{Nap} and $I_{Ca,T}$ activation), which oppose and favor changes in voltage, respectively [1, 20, 21]. The presence of amplifying and resonant ionic currents regulate the frequency-dependent coupling by increasing the $K(f)$ profile [32, 49, 51] or by causing $K(f)$ profile to be a BPF [32, 52], indicating the existence of an intermediate frequency band at which the transmission of information is more efficient than for other frequencies. However, a systematic study of how presence cellular resonance and phasonance in the participating cells shape the K and $\Delta\Phi$ profiles is lacking.

Multicompartment models of spatially extended neurons have been used to investigate the neuronal resonant properties distributed along the somato-dendritic axis and how the neuronal intrinsic ionic currents affect the response to, and propagation of spatially localized inputs [5, 54–62]. In an intriguing set of results [54, 55], it was experimentally demonstrated that two different types of subthreshold theta resonances [54, 55, 63–65] coexist along the somato-dendritic axis n hippocampal CA1 pyramidal cells (*in vitro*): (i) a perisomatic resonance generated by a slow-potassium M-type current (I_M) and amplified by a persistent sodium current (I_{Nap}), and (ii) a dendritic resonance generated by a hyperpolarization-activated mixed-cation (sodium and potassium) current or h-current (I_h). The mechanisms that control the interaction between these two types of resonances are not well understood.

We address these issues in this paper. We consider a network of two electrically connected neurons mediated by gap junctions receiving external inputs (Fig. 2). This is the minimal network architecture that allows for a systematic study of the biophysical and dynamic mechanisms that shape the $K(f)$ and $\Delta\Phi(f)$ profiles. The participating neurons are either passive cells (LPFs; 1D; Fig. 1-A1) or resonators (BPFs; 2D; Fig. 1-A2) and exhibit positive (Fig. 1-C1) or mixed negative-positive (Fig. 1-C2; phasonators) phase responses. We begin our study by using linear models to understand how the participating building blocks (e.g., conductances, negative and positive feedback effects) operating at the single node level control the $K(f)$ and $\Delta\Phi(f)$ profiles. We then turn our attention to linear models as linearized models of nonlinear of neurons with biophysically realistic ionic currents and investigate (to the linear level of approximation) how the presence of cellular ionic currents and cellular resonance and phasonance contribute to shaping the $K(f)$ and $\Delta\Phi(f)$ profiles. We use I_{Nap}, I_h and I_{Ks} motivated by the experimental results mentioned above and pre-

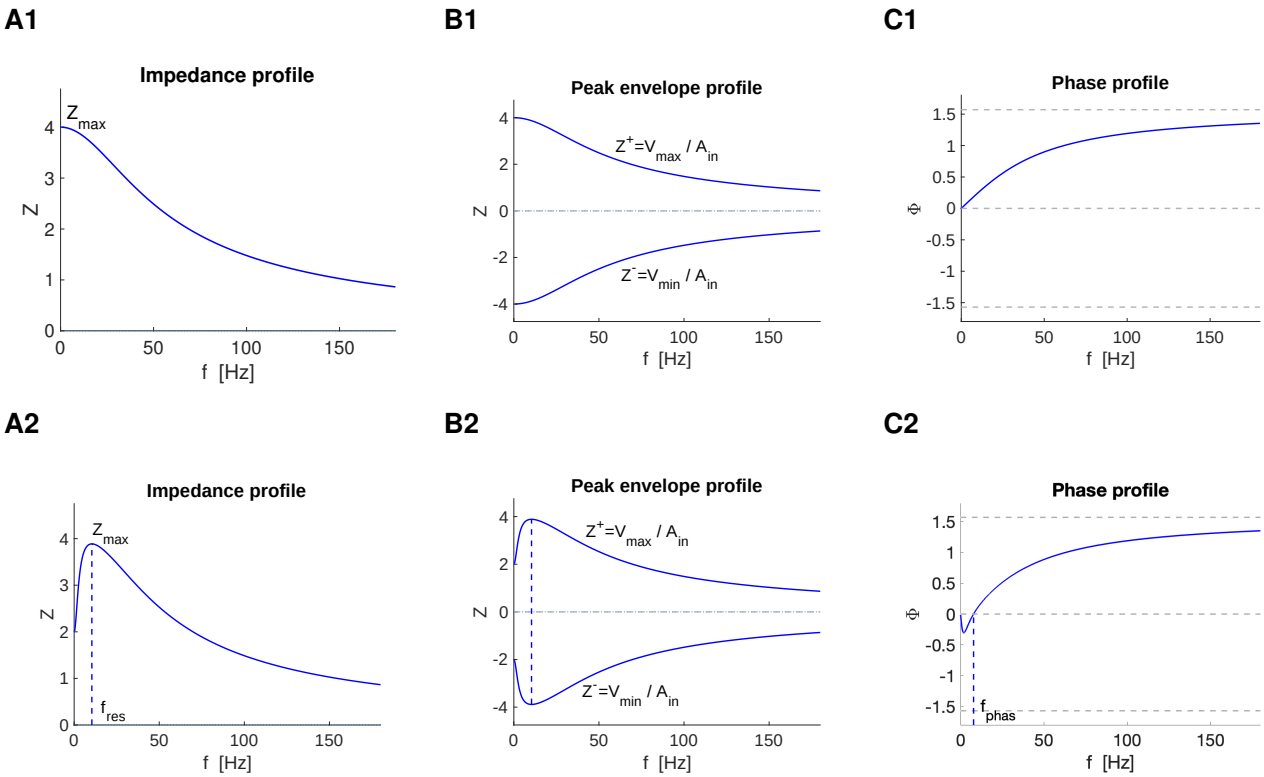

Figure 1: **Schematic diagrams of the impedance (A), peak envelope (B) and phase (C) profiles for a passive cell (low-pass filter, LPF, and lagging response; top) and a cell exhibiting resonance (band-pass filter; BPF) and phasonance (leading-lagging response) (bottom). A. A1.** $Z_{max} = Z(0)$. **A2.** Resonance refers to the ability of a cell to exhibit peak in $Z(f)$ at a non-zero (resonant) frequency f_{res}. **B1 - B2** V_{max}/V_{min} are the steady state peak /trough (maximum/minimum) voltage response values to the oscillatory inputs. Z^+ and Z^- are the upper and lower Z-envelope profiles, respectively. **C1.** Phasonance refers to the ability of a cell to exhibit a zero phase (phase-shift, $\Phi = 0$) response at a non-zero (phasonant) frequency f_{phas}. The voltage response lags for $f > f_{phas}$ and leads for $f < f_{phas}$.

vious studies [21, 66, 67]. We then extend our investigation to include the model nonlinearities to understand how the $K(f)$ and $\Delta\Phi(f)$ profiles are shaped by the interaction between the pre-J and post-J cells, and not just the post-J cells as for linear models. For gap junction connected networks, the connectivity is typically symmetric, while for compartmental models is asymmetric as the result of the different geometries of the participating compartments [68, 69]. We investigate the effects of asymmetric connectivity to understand how the compartmental geometry interacts with the neuronal biophysical properties to shape the $K(f)$ and $\Delta\Phi(f)$ profiles.

The formalism and tools we develop and use in this paper can be extended to larger networks with an arbitrary number of nodes, to spatially extended multicompartment neuronal models and to models having ionic currents with regenerative and restorative processes such as the ($I_{Ca,T}$) activation and inactivation.

Our results make experimentally testable predictions and have implications for the understanding of spike transmission, synchronic firing and coincidence detection in electrically coupled networks in the presence of oscillatory inputs.

Table 1 summarizes the notation used throughout the paper.

Table 1: Glossary

Context	Symbol	Meaning
Neuronal filters	LPF	Low-pass filter: see Fig. 1-A1
	BPF	Band-pass filter: see Fig. 1-A2
Electrically coupled network	pre-J	The node that directly receives the input (Fig. 2, left node)
	post-J	The node that indirectly receives the input (Fig. 2, right node)
		Nodes: Cells or compartments
Index	pre-J	$k = 1$
	post-J	$k = 2$
Frequency	f	Input frequency (in Hz)
	f_{res}	Resonant frequency
	f_{phas}	Phasonant frequency
	Ω	$= 2\,\pi\, f/T_{scale}$ $\quad (T_{scale} = 1000$ ms)
Single cell response profiles	$\mathbf{Z}(\mathbf{f})$	Complex impedance
	$Z(f)$, $A(f)$	Impedance amplitude
	$\Phi(f)$	Impedance phase
	$V_{max}(f)$	Peak envelope
	$V_{min}(f)$	Trough envelope
	$\hat{\mathbf{Z}}(f)$	Extended (complex) impedance
	$\hat{Z}(f)$	Extended impedance amplitude
	$\hat{\Phi}(f)$	Extended impedance phase
Individual cell (network) response profiles: cell k	$A_k(f)$	Amplitude response
	$\Phi_k(f)$	Phase response
	$\mathbf{A}_k(f)$	Complex amplitude response
	$\mathbf{Z}_k(f)$	Complex network impedance
	$\hat{\mathbf{Z}}_k^0(f)$	Extended (complex) impedance
	$\hat{Z}_k(f)$	Extended impedance amplitude
	$\hat{\Phi}_k(f)$	Extended impedance phase)
	$f_{res,k}$	Resonant frequency
	$f_{phas,\Delta\Phi}$	Phasonant frequency
Coupling and phase-difference coefficients	$K(f)$	Coupling coefficient
	$\Delta\Phi(f)$	Phase-difference coefficient
	$f_{res,K}$	Resonant (peak) frequency for K
	$f_{phas,K}$	Phasonance (zero-phase) frequency for $\Delta\Phi$

2 Methods

We consider a network of two electrically connected neurons mediated by gap junctions receiving external inputs (Fig. 2). With minimal modifications, the formalism we use describes two-compartment neurons receiving external inputs. The dynamics of the individual neurons are described by reduced, linearized [20, 21] or quadratized [70–72] biophysical (conductance-based) models of Hodgkin-Huxley (HH) type [69, 73]. The models include non-spiking ionic currents such as the persistent sodium current (I_{Nap}), the hyperpolarization-activated mixed-cation (I_h) current, the M-type slow-potassium current (I_{Ks}). I_{Nap} is regenerative (amplifying, favors changes in voltage, provides positive

feedback effects) and has fast dynamics, and it is assumed to be slaved to voltage, while I_h and I_{Ks} are restorative (resonant, oppose changes in voltage, provide negative feedback effects and have slower dynamics [66, 67, 71, 74, 75].

We refer the reader to S1 (Supplementary Material) for a description of the HH models and for the details on the linearization and quadratization processes as well as for the formulas linking the biophysical parameters with the parameters of the reduced (linearized or quadratized) models.

We use the following units for all the models in this paper: mV for voltage, ms for time, μF/cm^2 for capacitance, μA/cm^2 for current, mS/cm^2 for the maximal conductances and Hz for frequency.

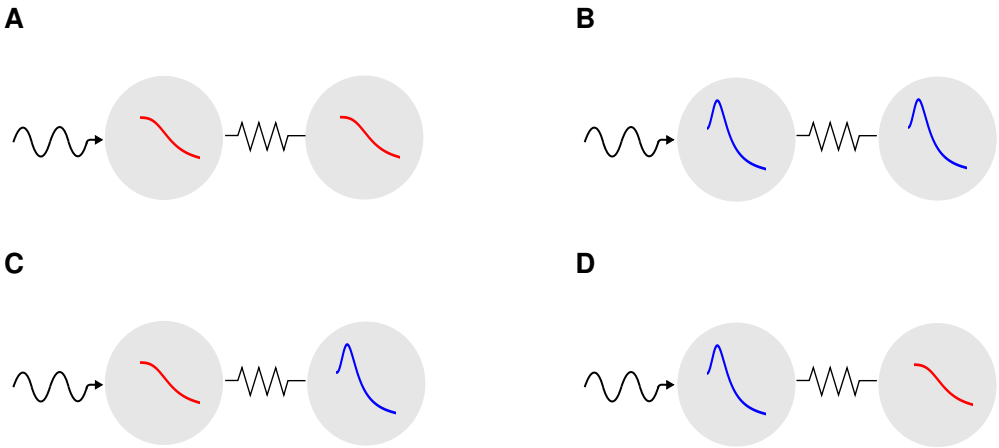

Figure 2: **Schematic diagrams of electrically coupled cells receiving oscillatory inputs.** The individual cells (disconnected) can have one-dimensional (1D, red) or two-dimensional (2D, blue) dynamics and exhibit either a low-pass filter (LPF; e.g., passive cells, red, see Fig. 1-A1) or a band-pass filter (BPF; e.g., resonators, blue, see Fig. 1-A2). The oscillatory inputs arrives to only one of the cells and are propagated to the second cell. We refer to the cell that receives the input as the pre-J cell and to the other cell as the post-J cell. In our models we use the indices $k = 1$ (pre-J) and $k = 2$ (post-J) cell. The same diagrams represent two-compartment models receiving oscillatory input to only one compartment. The filtering properties of the two connected cells may qualitatively differ from these of the individual (disconnected cells).

2.1 Networks of electrically coupled linearized cells

The linearized network model is described by (see Section S1.3)

$$C_k \frac{dv_k}{dt} = -g_{L,k}\, v_k - g_k\, w_k + g_c\,(v_j - v_k) + I_{in,k}(t), \tag{1}$$

$$\tau_k \frac{dw_k}{dt} = v_k - w_k, \tag{2}$$

for $k, j = 1, 2$. In eqs. (1)-(2), t is time, v_k represent the membrane potential, w_k represent the gating variable, C_k are the capacitances, $g_{L,k}$ are the linearized leak maximal conductances, g_k are the ionic current linearized conductances, τ_k are the linearized time constants for the linearized gating variables w_k, g_c is the gap junction coupling coefficient, and $I_{in,k}(t)$ are time-dependent input currents. The linearized component of the ionic currents with instantaneously fast dynamics (e.g., I_{Nap}) are incorporated in $g_{L,k}$. For two-compartment models with different connectivity coefficients, we use the notation $g_c = g_{c,kj}$.

Note that the heterogeneity due to different values of the biophysical parameters in the original conductance-based model is translated into the linearized model both explicitly and implicitly through the equilibria ($\bar{V}_1$ and $\bar{V}_2$) of the original system. Unless stated otherwise, we use $C_1 = C_2 = 1$ for all models in this paper.

2.2 Networks of electrically coupled quadratized cells

The quadratized network model is given by (see Section S1.4)

$$\frac{dv_k}{dt} = av_k^2 - w_k + g_c\,(v_j - v_k) + I_{in,k}(t), \tag{3}$$

$$\frac{dw_k}{dt} = \epsilon\,[\,\alpha\,v_k - \lambda - w_k\,], \tag{4}$$

for $k, j = 1, 2$, $k \neq j$, where $a > 0$ captures the effects of an amplifying current, g_c represents the gap junction coupling coefficient, ϵ is the inverse of the time constant of the resonant gating variable, $\alpha \geq 0$ represents the strength of the negative feedback (resonant) current, and λ is a combination of parameters including, and having the same sign as I_{app} in the original biophysical model. Increasing (decreasing) values of I_{app} cause λ to increase (decrease) and displaces the w-nullcline to the right (left), thus favoring (opposing) the generation of subthreshold oscillations and spikes (Fig. 3). Geometrically, a controles the curvature of the parabolic v-nullcline, α controls the slope of the w-nullcline, ϵ represents the time scale separation between the two variables, and λ controls the displacement of the w-nullcline with respect to the v-nullcline. As for the linear models, for two-compartment models with different connectivity coefficients, we use the notation $g_c = g_{c,kj}$.

Nonlinearities of parabolic type in the subthreshold voltage regime are generated in the presence of regenerative/amplifying currents (e.g., I_{Nap}). The resulting voltage nullclines of parabolic type are shaped by the interplay of these and the other participating ionic currents (e.g., I_h, I_{Ks}).

Quadratization of biophysically plausible models of HH type extends the notion of linearization to include the parabolic-like properties of the V-nullcline in the subthreshold regime and therefore capture more realistic aspects of the dynamics of these models, which can be missed by the corresponding linearization [70–72, 74, 76, 77]. In contrast to linearization, which is carried out around the model's fixed point (determined by the intersection of the model's nullclines), quadratization is done around the extremum (minimum or maximum) of the V-nullcline of quadratic type and the resulting quadratized nullcline is always concave up.

The process of quadratization [70, 71] consists of expanding the right-side of the (original) biophysical model's differential equations into Taylor series around the minimum/maximum (V_e, $x_{1,e}$) of the parabolic-like V-nullcline in the subthreshold regime, neglecting all the terms with power bigger than two in the equation for V and bigger than one in the equation for x_1, and translating the minimum/maximum of the V-nullcline to the origin. The description of the quadratization process as well as the definition of the quadratized parameters below in terms of the parameters of biophysically realistic (conductance-based) models of Hodgkin-Huxley type are presented in the Supplementary material S1.4. Additional details are provided in [70–72] for 2D and 3D models. A Comparison between the original (biophysical) I_{Nap} + I_h and I_{Nap} + I_{Ks} models (see below) and their quadratization is shown in Fig. S6-A3 and -B3 [72]. A detailed description of the process for 3D models of HH type including time-dependent external currents and synaptic inputs is presented in [70] and also discussed in [72] in the context of reduced neuronal models.

While the assumption that the V-nullcline is parabolic-like in the subthreshold regime (e.g., Fig. 2 in [70] and Fig. 7 in [72]) is a rather general property of the type of models of HH described above, in certain, also rather general parameter regimes, these models can have V-nullclines of cubic-type [66, 67] around which (not around the parabolic component of the cubic-like nullcline) relevant subthreshold behavior such as subthreshold oscillations are generated.

2.3 The $\mathbf{I_{Nap}}$ + $\mathbf{I_h}$ and $\mathbf{I_{Nap}}$ + $\mathbf{I_{Ks}}$ conductance-based models

The I_{Nap} + I_h and I_{Nap} + I_{Ks} models [66, 71] are conductance-based models of Hodgkin-Huxley type [73] in the subthreshold voltage regime that involve the interaction of the two active ionic currents that define them. Both models include two variables: the voltage V and a gating variable associated to the slower I_h or I_{Ks} currents. The dynamics of I_{Nap} is assumed to be instantaneously fast (slaved to voltage). The mathematical formulation is presented in Section

S1.1 together with the parameter values we use in this paper. The two models are adapted versions of the models presented in [75, 78] (see also [66, 67, 70–72]).

Both the I_{Nap} + I_h and I_{Nap} + I_{Ks} models involve the interaction of a restorative current, I_h and I_{Ks}, having a resonant gating variable, and the same regenerative current, I_{Nap}, having an amplifying gating variable. Because all these currents have a single gating variable, we refer to them as resonant and amplifying currents, correspondingly. They provide a positive (I_{Nap}) and slower negative (I_h and I_{Ks}) feedback effects, favoring and opposing changes in voltage, respectively.

The two models have V-nullclines of quadratic type or are quasi-linear in the subthreshold regime for the parameter sets considered in this paper (Figs. S4, and S6-A1 and -B1) (see also [70], Fig. 2, and [72], Fig. 7). Note that while the two models describe the interplay of a resonant (I_h or I_{Ks}) and an amplifying current (I_{Nap}), the nullclines are qualitatively a mirror image of each other: the V-nullcline is concave down for the I_{Nap} + I_h model (Fig. S4) and concave up for the I_{Nap} + I_{Ks} model (Figs. S1.2.4). The process of quadratization (see Section S1.4) uncovers the qualitative similarity of the phase-plane diagrams for both models (Fig. S6) (except for the concavity differences between the nullclines for the slow gating variable).

Figs. S4 and S1.2.4 illustrate the dynamics of the I_{Nap} + I_h and I_{Nap} + I_{Ks} models, respectively. In the subthreshold regime, the models have a stable fixed-point, towards which trajectories evolve, and sometimes an additional, unstable fixed-point. The system transitions from quasi-linear (in a vicinity of the stable fixed-point) to parabolic-like as some control parameter (e.g, I_{app}, G_p, G_h) and the dynamics are modified accordingly. Increasing values of certain parameters (e.g., I_{app}, G_h, G_p) cause a Hopf bifurcation near the knee of the V-nullcline where the fixed-point looses stability and moves to the “right branch" of the parabolic-like nullcline. Trajectories leaving the subthreshold regime is interpreted as the onset of a spike. When the models are supplemented with a return mechanism to the subthreshold regime, they are referred to as models of quadratic integrate-and-fire type with adaptation [72, 74, 76].

The I_{Nap} model is a 1D reduced version of the 2D models discussed above, which does not include any slow ionic current. It is described in Section S1.2 in the Supplementary Material by eqs. (S1) with $I_1 = 0$ and $I_2 = I_{Nap}$ (eq. S3). Analogously to the other two models, it has parabolic-like or quasi-linear speed (dV/dt vs. V) curve in the subthreshold regime. The dynamics of the I_{Nap} model are illustrated in Fig. S2 in the Supplementary Material. For low enough values of G_p, the model develops nonlinearities of parabolic type, but remains quasi-linear in a vicinity of the stable fixed-point (blue dot at the intersection of the speed curve). The trajectories (not shown) move along the V axis and converge to these fixed points. As G_p increases, the nonlinearities become more pronounced in a vicinity of the stable fixed-point, For the saddle-node bifurcation value of G_p, the fixed-points cease to exist and trajectories leave the subthreshold regime. This is interpreted as the onset of a spike and if the model is endowed with a return mechanism to the subthreshold regime, it becomes a model of quadratic integrate-and-fire type [72] (the well-known quadratic integrate-and-fire model [79, 80] has a purely parabolic speed curve)

2.4 Single cell voltage response to oscillatory inputs: low- and band-pass filters

The voltage response of a neuron receiving an oscillatory input current (with frequency f) is typically measured in terms of the impedance $\mathbf{Z}(f)$, a complex quantity with amplitude $Z(f) = |\mathbf{Z}(f)|$ and phase $\Phi(f)$. Following others, we refer to $Z(f)$ simply as the impedance. Passive cells are low-pass filters (LPFs; e.g., Figs. 1-A1) and exhibit a lagged response (e.g., Figs. 1-C1). More complex cells can be band-pass filters (BPFs; e.g., Figs. 1-A2) and exhibit a lagged/leading response (e.g., Figs. 1-C2). A system exhibits *resonance* if $Z(f)$ peaks at a non-zero (resonant) frequency f_{res} (e.g., Figs. 1-A2) and *phasonance* if $\Phi(f)$ vanishes at a non-zero (phasonant) frequency f_{phas} (e.g., Figs. 1-C2).

The generation of cellular resonance requires the interplay of negative and positive feedback effects mediated by the gating variables associated to the intrinsic, resonant (e.g., I_h, I_{Ks}) and amplifying (I_{Nap}) ionic currents, respectively.

The resonant properties of 2D linear and nonlinear neuronal systems, including their relationship between the cellular intrinsic biophysical properties and the dynamic mechanism of generation of resonance have been investigated

extensively by us and other authors [20,21,71,81]. In the Supplementary Material S2 we present the analytical expressions of $Z(f)$ and $\Phi(f)$ for linear (1D and 2D) neuronal models receiving a sinusoidal input current of the form

$$I_{in}(t) = A_{in}\,\sin(\Omega\,t) \qquad \text{with} \qquad \Omega = \frac{2\pi f}{1000}. \tag{5}$$

For nonlinear systems we define the peak envelope impedance profile (Fig. 1-B) [81,82] as

$$Z^{ENV}(f) = \frac{V_{max}(f) - V_{min}(f)}{2A_{in}} \tag{6}$$

where $V_{max}(f)$ and $V_{min}(f)$ are the peak and trough envelope profiles, respectively, defined as the maximum and minimum values, respectively, of the steady-state oscillatory voltage $V_{out}(f)$ as a function of the input frequency f. For linear systems, $Z^{ENV}(f) = Z(f)$. Similarly, the phase Φ is computed as the distance between the peaks of the output and closest input normalized by period, and f_{phas} is the non-zero frequency where Φ vanishes. These quantities extend the concept of impedance and phase to nonlinear systems under certain conditions (the input and output frequencies coincide and the output amplitude is uniform across cycles for a given input with constant amplitude).

2.5 Network voltage response to oscillatory inputs

We now consider a two-cell network (Fig. 2) receiving sinusoidal inputs of the form (5) $I_{in,k}(t) = A_{in,k}\sin(\Omega\,t)$ ($k = 1,2$). In this paper, we consider inputs to only one cell (cell 1); i.e., $I_{in,1}(t) = A_{in}\sin(\Omega\,t)$ and $I_{in,2}(t) = 0$. For generality, in the Supplementary Material S3 we provide the calculations using linear networks of N cells, each having 2D linear dynamics and sinusoidal inputs to all cells in the network.

2.5.1 Networks of linear nodes

For networks having linear nodes and linear connectivity, the voltage response of each cell has the form $V_{out,k}(t;f) = A_k(f)\sin(\Omega\,t - \Phi_k(f))$. The amplitude $A_k(\Omega)$ and phase $\Phi_k(\Omega)$ are the component of the complex network voltage amplitude response $\mathbf{A}_k(f)$ derived in Section S3

$$\mathbf{Z}_1(\Omega) = \frac{\mathbf{A_1}(\Omega)}{A_{in,1}} = \frac{1}{1 - g_c^2\,\hat{\mathbf{Z}}^{\mathbf{0}}_{\mathbf{1}}(\Omega)\,\hat{\mathbf{Z}}^{\mathbf{0}}_{\mathbf{2}}(\Omega)}\,\hat{\mathbf{Z}}^{\mathbf{0}}_{\mathbf{1}}(\Omega) \tag{7}$$

and

$$\mathbf{Z}_2(\Omega) = \frac{\mathbf{A_2}(\Omega)}{A_{in,1}} = \frac{g_c\,\hat{\mathbf{Z}}^{\mathbf{0}}_{\mathbf{1}}(\Omega)}{1 - g_c^2\,\hat{\mathbf{Z}}^{\mathbf{0}}_{\mathbf{1}}(\Omega)\,\hat{\mathbf{Z}}^{\mathbf{0}}_{\mathbf{2}}(\Omega)}\,\hat{\mathbf{Z}}^{\mathbf{0}}_{\mathbf{2}}(\Omega), \tag{8}$$

where $\hat{\mathbf{Z}}^{\mathbf{0}}_{\mathbf{k}}(\Omega)$ ($k = 1,2$) are the extended (complex) impedances of the individual (disconnected) nodes in the network obtained from eq. (S32) in the Supplementary Material S2 by substituting the parameters $g_{L,k}$ by $g_{L,k} + g_c$

$$\hat{\mathbf{Z}}^0_k(f) = \frac{\mathbf{Q}_k(\Omega)}{\mathbf{P}_{k,c}(\Omega)} \tag{9}$$

where

$$\mathbf{P}_{k,c}(\Omega) = P_k(\Omega; g_c) = g_{L,k} + g_k + g_c - C_k\tau_k\Omega^2 + i\,\Omega\,(g_{L,k}\tau + g_c\tau + C_k) \tag{10}$$

and

$$\mathbf{Q}_k(\Omega) = 1 + i\,\Omega\,\tau_k, \tag{11}$$

for $k = 1, 2$. This captures the fact that the gap junction current includes a “self-connectivity" term, which is incorporated into the autonomous part of the corresponding nodes k. The extended amplitude impedance and phase profiles are given by eqs. (S53)-(S54) in Section S3.1.

2.5.2 Networks of nonlinear nodes: network impedance and peak envelope profiles

For nonlinear networks we adapt the tools defined in the previous section by adding the appropriate indices and referring to the corresponding quantities for the individual (disconnected) cells by adding a superscript "0". In contrast to linear systems, the voltage response for nonlinear systems is not symmetric. Therefore, while the impedance amplitude captures the frequency content of the voltage response signal, it does not necessarily describe the frequency-dependent prope rties of the peak and trough envelope profiles. Because neuronal signal occurs via voltage threshold-like mechanisms, we will look at the peak envelope profiles $V_{max,k}(f)$ for $k = 1, 2$

2.6 Coupling coefficient: Frequency-dependent profiles and preferred communication frequencies

2.6.1 Amplitude and phase

We extend the notion of the (steady state) coupling coefficient in response to constant (DC) inputs [23–25, 28, 35] to include the frequency-dependent effects in response to oscillatory inputs by defining the amplitude coupling coefficient

$$K(f) = \frac{V_{max,2}(f) - \bar{v}_2}{V_{max,1}(f) - \bar{v}_1} \tag{12}$$

where $(\bar{v}_1, \bar{v}_2)$ is the fixed point of system (1)-(2), when unperturbed and the phase-difference coupling coefficient

$$\Delta\Phi(f) = \Phi_2(f) - \Phi_1(f). \tag{13}$$

For linear systems ($\bar{v}_1 = \bar{v}_2 = 0$), $K(f)$ and $\Delta\Phi(f)$ are the components of the following complex quantity

$$\mathbf{K}(f) = \frac{\mathbf{Z}_2(f)}{\mathbf{Z}_1(f)} = \frac{Z_2(f)}{Z_1(f)}\, e^{-[\,\Phi_2(f)-\Phi_1(f)\,]} = \frac{A_2(f)}{A_1(f)}\, e^{-[\,\Phi_2(f)-\Phi_1(f)\,]} = K(f)\, e^{-\Delta\Phi(f)}. \tag{14}$$

From (7)-(8),

$$K(f) = g_c\, \hat{Z}_2^0(f) \qquad \text{and} \qquad \Delta\Phi = \hat{\Phi}_2^0(f). \tag{15}$$

2.6.2 K-resonance and $\Delta\Phi$-phasonance

We define K-resonance as the ability of the coupling coefficient $K(f)$ to exhibit a peak at a non-zero input frequency $f_{res,K}$, and $\Delta\Phi$-phasonance as the ability of the frequency-dependent coupling phase $\Delta\Phi(f)$ to vanish for a nonzero input frequency $f_{phas,\Delta\Phi}$.

From eq. (12), a necessary condition for the existence of K-resonance (or K-antiresonance) is given by

$$V'_{max,2}(f)(V_{max,1}(f) - \bar{v}_1) - V'_{max,1}(f)(V_{max,2}(f) - \bar{v}_2) = 0, \tag{16}$$

for some value $f > 0$.

We characterize the $K(f)$ profile by using two attributes: (i) the resonant frequency $f_{res,K}$, defined as the peak frequency of $K(f)$, and (ii) the resonance amplitude $Q_K = K_{max} - K(0)$. If the K profile does not exhibit resonance, then $f_{res,K} = Q_K = 0$. We characterize the $\Delta\Phi(f)$ profile by using the phasonant frequency $f_{phas,\Delta\Phi}$.

2.7 Electrically coupled neuronal compartments

The mathematical formulation of two-compartment models of spatially extended cells (e.g., dendritic, somato-dendritic) having linear dynamics is as described in Sections 2.1 and 2.2 with g_c substituted by g_c/σ_k ($k = 1, 2$) with $\sigma_1 + \sigma_2 = 1$, where σ_k represents the fraction of the total cell area taken up by the corresponding compartment [83–85]. For linearized models, because of the possible asymmetry between the two compartments, there is a constant membrane potential effect due to the differences in the resting potential of the two compartments.

For two-compartment models of linear nodes where the input arrives only to one of the compartments (compartment 1), the complex network voltage amplitude response presented in Section 2.5.1 extends to (see also Section S3)

$$\mathbf{A_1}(\Omega) = \frac{\sigma_1\sigma_2}{\sigma_1\sigma_2 - g_c^2\,\hat{\mathbf{Z}}_{\mathbf{1}}^{\mathbf{0}}(\Omega)\,\hat{\mathbf{Z}}_{\mathbf{2}}^{\mathbf{0}}(\Omega)}\,\hat{\mathbf{Z}}_{\mathbf{1}}^{\mathbf{0}}(\Omega)\,A_{in,1} \tag{17}$$

and

$$\mathbf{A_2}(\Omega) = \frac{g_c\,\sigma_1\,\hat{\mathbf{Z}}_{\mathbf{1}}^{\mathbf{0}}(\Omega)}{\sigma_1\sigma_2 - g_c^2\,\hat{\mathbf{Z}}_{\mathbf{1}}^{\mathbf{0}}(\Omega)\,\hat{\mathbf{Z}}_{\mathbf{2}}^{\mathbf{0}}(\Omega)}\,\hat{\mathbf{Z}}_{\mathbf{2}}^{\mathbf{0}}(\Omega)\,A_{in,1}, \tag{18}$$

where $\hat{\mathbf{Z}}_{\mathbf{k}}^{\mathbf{0}}(\Omega) = \hat{\mathbf{Z}}_{\mathbf{k}}^{\mathbf{0}}(\Omega; g_c/\sigma_k)$ ($k = 1, 2$) are the extended (complex) impedances of the individual (disconnected) nodes in the network obtained from eq. (S32) in the Supplementary Material S2 by substituting the parameters $g_{L,k}$ by $g_{L,k} + g_c/\sigma_k$. This can be straightforwardly extended to more detailed formulations involving the geometric (length, area) and biophysical properties of neuronal compartments and a larger number of compartments [68, 69].

It follows that

$$K(f; g_c/\sigma_2) = \frac{g_c}{\sigma_2}\,\hat{Z}_2^0(f; g_c/\sigma_2) \qquad \text{and} \qquad \Delta\Phi(f; g_c/\sigma_2) = \hat{\Phi}_2^0(f; g_c/\sigma_2). \tag{19}$$

2.8 Numerical simulations

To compute the numerical solutions we used a Runge-Kutta method of order 4 [86] with a time step $\Delta t = 0.01$ ms. Smaller values of Δt have been used to check the accuracy of the results. All neural models and metrics, including phase-plane analysis, were implemented in MATLAB (The Mathworks, Natick, MA). The codes are available at `https://github.com/BioDatanamics-Lab/Coupling_Coefficient-25_05`.

3 Results

3.1 Steady-state coupling coefficient K in response to constant inputs

3.1.1 Linear models: revisited

The steady-state response of the electrically coupled linear cells (1)-(2) to a constant (DC) inputs I_1 ($I_2 = 0$) is given by

$$\bar{v}_1 = \frac{(g_{L,2} + g_2 + g_c)\,I_1}{(g_{L,1} + g_1 + g_c)\,(g_{L,2} + g_2 + g_c) - g_c^2} \tag{20}$$

and

$$\bar{v}_2 = \frac{g_c\,I_1}{(g_{L,1} + g_1 + g_c)\,(g_{L,2} + g_2 + g_c) - g_c^2} \tag{21}$$

for the pre-J and post-J cells, respectively.

The coupling coefficient is therefore given by

$$K = \frac{v_2}{v_1} = \frac{g_c}{g_{L,2} + g_2 + g_c}. \tag{22}$$

As reported before for networks of passive cells ($g_2 = 0$) [43,44][1], K is independent of the input current and the intrinsic properties of the pre-J cell, and varies between 0 and 1. For networks of 2D linear cells, K is affected by g_2 in addition to$g_{L,2}$ and it remains independent of the intrinsic properties of the pre-J cell.

Note that if the connectivity coefficients are different, as it is usually the case for two-compartment models, then

$$\bar{v}_1 = \frac{(g_{L,2} + g_2 + g_{c,12})\, I_1}{(g_{L,1} + g_1 + g_{c,12})\,(g_{L,2} + g_2 + g_{c,21}) - g_{c,12} g_{c,21}} \tag{23}$$

and

$$\bar{v}_2 = \frac{g_{c,12}\, I_1}{(g_{L,1} + g_1 + g_{c,12})\,(g_{L,2} + g_2 + g_{c,21}) - g_{c,12} g_{c,21}} \tag{24}$$

for the pre-J and post-J cells, respectively, and

$$K = \frac{v_2}{v_1} = \frac{g_{c,21}}{g_{L,2} + g_2 + g_{c,21}}. \tag{25}$$

3.1.2 Quadratic models

Our analytical results for networks of weakly nonlinear cells (Section S4) show that as the result of the presence of nonlinearities, K is no longer independent of I_1 and is (weakly) affected by the intrinsic properties of both the pre- and post-J cells (Section S4.1). Here, we test these ideas for the quadratic model (3)-(4).

The dynamics of the quadratic model is illustrated in Fig. 3. Changes in the values of the constant (DC) input current are monotonically reflected in the parameter λ. In our simulations, we first determined a baseline value of λ, λ_{base} and computed the stationary voltage response $v_{ss,base}$ of the individual cells to this value. We then computed λ as $\lambda = \lambda_{base} + \Delta\lambda$ and used $v_{ss,base}$ as the initial condition in our simulations (blue dots in Fig. (right column).

Fig. 4-A illustrates the response of the pre-J (v_1) and post-J (v_2) cells for values of g_c that increase from panel A1 to panel A2. Fig. 4-B shows curves of K as a function of $\Delta\lambda$ for representative scenarios. In contrast to linear models, there is a dependence of K on λ, which is more pronounced for the larger values of g_c. Comparison between panels B1 and B2 illustrate that the dependence of K on λ is independent on ϵ. Comparison between panels B1 and B3 illustrate that the dependence of K on λ is more pronounced and the values of K are larger the smaller α (all other parameters fixed). Finally, comparison between panels B1 and B4 illustrate that the dependence of K on λ is slightly more pronounced and the values of K are larger the smaller a (all other parameters fixed).

3.2 Response to oscillatory inputs: Electrically coupled linear cells

Linear models of single neurons exhibit a variety of amplitude and phase profiles in response to oscillatory inputs (e.g., Fig. 1) [1,20,21,87–89] (see Section S2). Neuronal linearized models encode information about the inherently nonlinear biophysical properties of neurons and networks. Therefore, linearized models can be used to analyze the nonlinear dependence of the $K(f)$ and $\Delta\Phi(f)$ filtering properties on the resonant and amplifying mechanisms operating at the single cell level by tracking the changes in the (linearized) model parameters as the result of the changes in the levels of the interacting ionic currents. While the response for each set of parameter values is linear, the variation of the responses as the parameters are recalculated for each biophysical scenario capture nonlinear effects such as the nonlinear amplification that occurs near threshold.

[1] Cite others

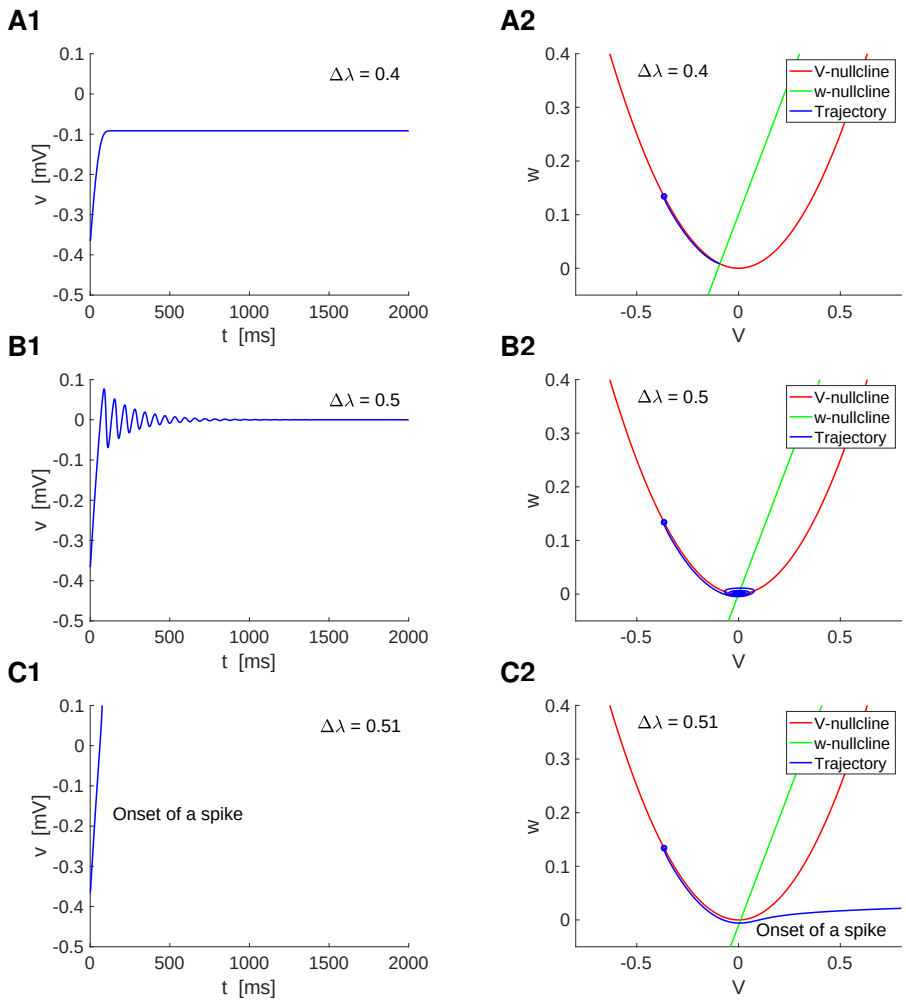

Figure 3: **Response of a single cell quadratic model to constant inputs: Voltage traces and phase-plane diagrams.** We used the model (3)-(4) for a single cell ($g_c = 0$) with $a = 1$, $\alpha = 1$ and $\epsilon = 0.01$. The initial conditions (blue dots) were determined as the steady-state response to a baseline value of λ: $\lambda_{base} = -0.5$ and the values of λ were determined as $\lambda = \lambda_{base} + \Delta\lambda$. **Left Column.** Voltage traces. **Right column.** Phase-plane diagrams. The V-nullclines (red) are the curves satisfying $w = a\,v^2$ and the w-nullclines (green) are the lines satisfying $w = \alpha\,v - \lambda$. The fixed-point is determined by the intersection between the two nullclines. The trajectories (blue) are initially located at the blue dot and evolve towards the fixed-point. **A.** $\Delta\lambda = 0.4$ ($\lambda = -0.1$). The model exhibits an almost monotonic increase to the steady state value of v (there is an imperceptible overshoot at low values of t). **B.** $\Delta\lambda = 0.5$ ($\lambda = 0$). The model exhibits subthreshold oscillations around the steady-state value of v. **C.** $\Delta\lambda = 0.51$ ($\lambda = 0.1$). The model produces the onset of spikes when the trajectory increases unboundedly and escapes the subthreshold voltage regime. The model ceases to be a good approximation to any biophysical model. A voltage reset mechanism is needed to bring the trajectory back to the subthreshold regime.

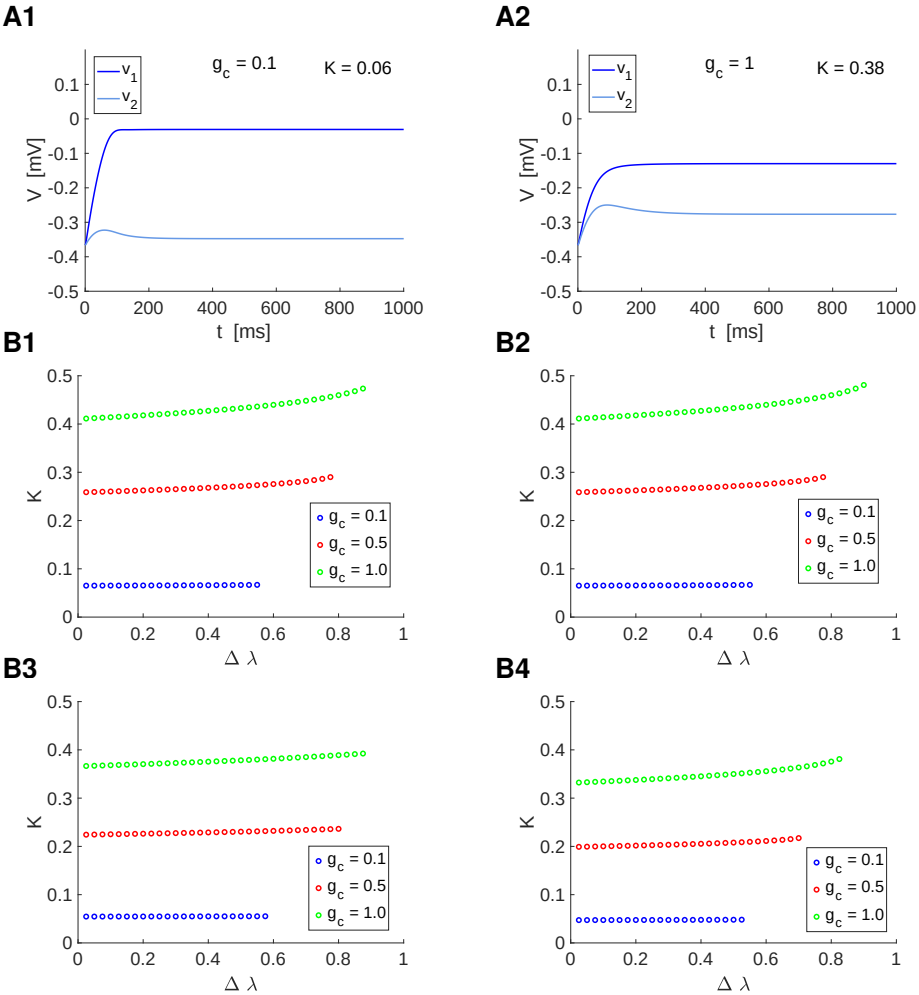

Figure 4: **Response of a single cell quadratic model to constant inputs: Coupling coefficient.** We used the model (3)-(4) with $a = 1$, $\alpha = 1$ and $\epsilon = 0.01$. The initial conditions were determined as the steady-state response to a baseline value of λ: $\lambda_{base} = -0.5$ and the values of λ were determined as $\lambda = \lambda_{base} + \Delta\lambda$. **A.** Voltage traces for representative examples and $\lambda = 0.5$. **A1.** $g_c = 0.1$. **A2.** $g_c = 1$. **B.** Dependence of K on $\lambda = \lambda_{base} + \Delta\lambda$ for representative values of g_c, ϵ, α and a. **B1.** $a = 1$, $\alpha = 0.25$, $\epsilon = 0.01$. **B2.** $a = 1$, $\alpha = 0.25$, $\epsilon = 0.1$. **B3.** $a = 1$, $\alpha = 1$, $\epsilon = 0.01$. **B4.** $a = 2$, $\alpha = 0.25$, $\epsilon = 0.01$.

Here we analyze the response of electrically coupled linear cells to oscillatory inputs. We use these results in the next section to analyze the response of biophysical models to oscillatory inputs. The expressions for the linearized conductances g_L and g in terms of the biophysical parameters of the original (biophysical) model are presented in Section S1.3 by eqs. (S14) and (S15).

For purely linear networks (linear nodes and linear connectivity) of the form (1)-(2), the network complex amplitude response to oscillatory inputs for the pre-J ($\mathbf{A}_1$) and post-J ($\mathbf{A}_2$) cells are given by eqs. (7) and (8), respectively (see Section S3 for details on the formulas and their derivation). The numerators describe the response of the directly activated pre-J cell and the indirectly activated post-J cell, respectively, modulated by the presence of the gap junction via de extended impedances ($\hat{\mathbf{Z}}_1$ and $\hat{\mathbf{Z}}_2$). The denominators, describe the interaction between the two cells in response to the oscillatory input.

From eqs. (15), the CC $K(f)$ for linear systems is proportional to the extended impedance of the post-J cell and the phase-difference coefficient $\Delta\Phi(f)$ is equal to the extended phase of the post-J cell. Both quantities are independent of the input amplitude (A_{in}) to the pre-J cell and of the intrinsic properties of the pre-J cell. While the formulas are valid for both cells, here we focus on $g_{L,2}$ and g_2 for the post-J cell since the $K(f)$- and $\Delta\Phi(f)$-profiles depend on these parameters.

3.2.1 Passive cells

For two electrically coupled passive cells (1)-(2) ($g_k = 0, k = 1, 2$) (Fig. 2-A), the coupling and phase-difference coefficient profiles are given, respectively, by

$$K(f; g_c) = \frac{g_c}{\sqrt{(g_{L,2} + g_c)^2 + \Omega^2}} \tag{26}$$

and

$$\Delta\Phi(f; g_c) = \tan^{-1}\left(\frac{\Omega}{g_{L,2} + g_c}\right) \tag{27}$$

The calculations are presented in the Supplementary material S2, eqs. (S38) and (S39).

The $K(f)$-profiles are LPFs (Fig. 5, left) and the $\Delta\Phi(f)$ profile are monotonically increasing (Fig. 5, right), indicating that the lag difference between the two cells is monotonically increasing. Therefore, the results from this Section remain true when the pre-J cells is a resonator (Fig. 2-D).

Fig. 5-A illustrates the dependence of the $K(f)$- and $\Delta\Phi(f)$-profiles on g_c and $g_{L,2}$. The network A-profiles (individual cells) are LPFs (Fig. 5-A1). Increasing values of $g_{L,2}$ (for fixed values of g_c) attenuate the A-profiles and make them shallower. Increasing values of g_c (for fixed values of $g_{L,2}$) also make the $K(f)$-profiles shallower, but amplify them, as expected. In the first case, the recruitment of the post-J cell is stronger, which in turn weakens the response of the pre-J cell (Fig. 5-B1), while in the second case, the response of the two cells is weaker as $g_{L,2}$ increases (Fig. 5-C1).

The network Φ-profiles are monotonically increasing (Fig. 5-A2). Increasing values of $g_{L,2}$ (for fixed values of g_c) and increasing values of g_c (for fixed values of $g_{L,2}$) reduce the rate of increase of the $\Delta\Phi(f)$ profiles, indicating that the response oscillations' peaks for the two cells are closer the larger the input frequency. The stronger recruitment of the post-J cell as g_c increases (Fig. 5-B1) is accompanied by a reduction in both the network phases and phase-difference for each input frequency f (Fig. 5-B2). A similar effect is produced by increasing values of $g_{L,2}$.

3.2.2 Linear (2D) resonators: Interplay of positive and negative feedback effects

Resonators refer to cells that exhibit resonance [1]. For simplicity, here, we include in this category cells that exhibit resonance both in the absence or presence of damped subthreshold oscillations [20, 21] where the fixed-points are nodes and foci, respectively (i.e., we do not distinguish between resonators and damped oscillators). Resonators may

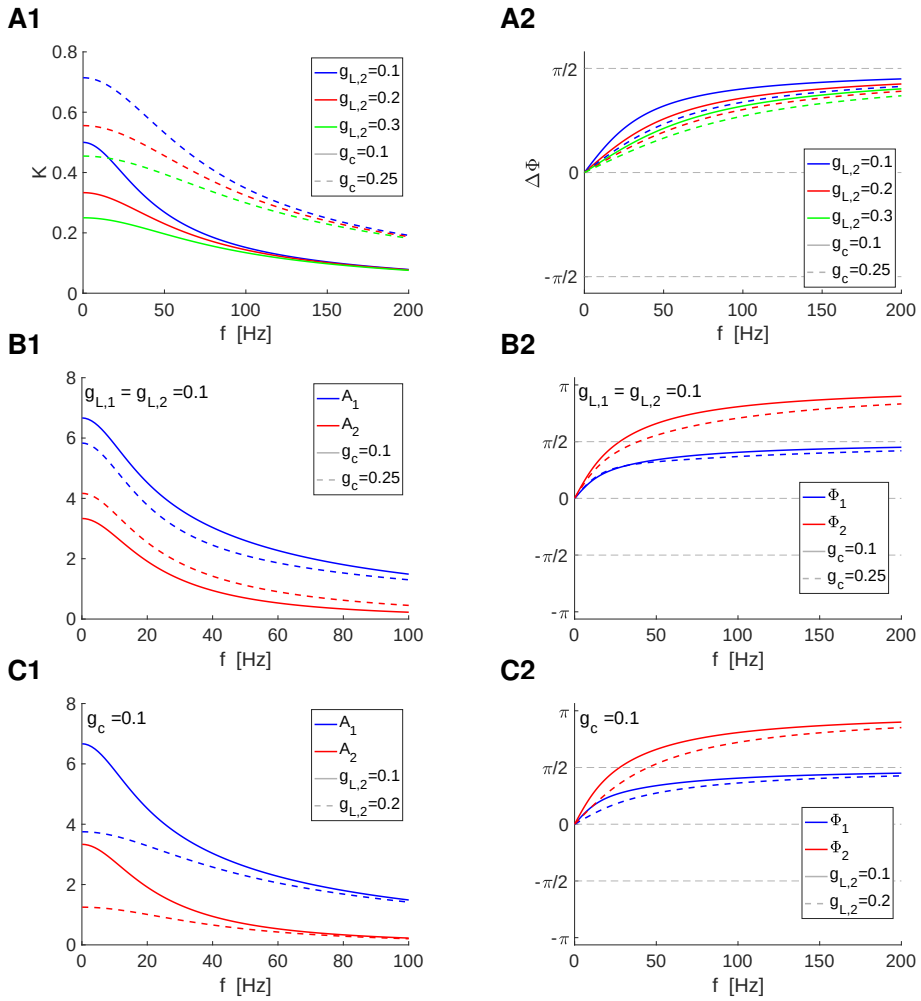

Figure 5: **Response of two electrically coupled passive cells to oscillatory inputs for representative parameter values.** The linear model is given by eqs. (1)-(2) with $g_1 = g_2 = 0$. Cells 1 and 2 are the pre-J and post-J cells, respectively. **A.** Coupling and phase-difference coefficients. **A1.** Coupling coefficient K given by eq. (26). **A2.** Phase-difference coefficient $\Delta\Phi$ given by eq. (27). **B.** Amplitude and phase responses for the pre-J (blue) and post-J (red) cells for representative values of $g_{L,1}$, $g_{L,2}$ and g_c. The blue curves and red curves correspond to the solid- and dashed-blue curves in panels A, respectively. These quantities were computed using eqs. (7)-(8) with $g_1 = g_2 = 0$. **B1.** Amplitude responses. **B2.** Phase responses. **C.** Amplitude and phase responses for the pre-J (blue) and post-J (red) cells for representative values of $g_{L,1}$, $g_{L,2}$ and g_c. The blue curves and red curves correspond to the solid- and dashed-blue curves in panels A, respectively. These quantities were computed using eqs. (7)-(8) with $g_1 = g_2 = 0$. **C1.** Amplitude responses. **C2.** Phase responses.

also show phasonance [20, 21]. Resonance, phasonance and oscillations require the interplay of positive and slower negative feedback effects that favor and oppose changes of voltage, respectively. In the linearized models (1)-(2), the negative feedback is represented by $g_k > 0$ ($k = 1, 2$) and the positive feedback is embedded in the parameters $g_{L,k}$.

For two electrically coupled 2D linear cells (1)-(2) ($g_k > 0, k = 1, 2$) (Fig. 2-B), the coupling and phase-difference coefficient profiles are given, respectively, by

$$K(f; g_c) = g_c \sqrt{\frac{1 + \tau_2^2\,\Omega^2}{(g_{L,2} + g_2 + g_c - \tau_2\,\Omega^2)^2 + (g_{L,2}\,\tau_2 + g_c\tau_2 + 1)^2\,\Omega^2}} \tag{28}$$

and

$$\Delta\Phi(f; g_c) = \tan^{-1}\left(\frac{1 - \tau_2 g_2 + (\tau_2\,\Omega)^2}{g_{L,2} + g_2 + g_c + (g_{L,2} + g_c)(\tau_2\,\Omega)^2}\Omega\right). \tag{29}$$

The calculations are presented in the Supplementary material S2, eqs. (S33) and (S34) with $C = 1$. These results in this Section remain true when the pre-J cells is passive (Fig. 2-C).

Fig. 6 illustrates the $K(f)$ and $\Delta\Phi(f)$ profiles for representative scenarios. We focus on individual cells that exhibit resonance (e.g., Fig. 6-D1, dashed-blue) and phasonance (e.g., Fig. 6-D2, dashed-blue). The $K(f)$ profiles are BPFs(f (Fig. 6-A1 to -C1), exhibiting K-resonance, and the $\Delta\Phi(f)$ profiles show $\Delta\Phi$-phasonance (e.g., Fig. 6-A2 to C2) in most cases considered. As mentioned above, these profiles are determined by the parameter of the post-J cell and g_c, and are independent of the input amplitude and the properties of the post-J cell.

Figs. 6-A1 to -C1 show the dependence of the $K(f)$-profiles on the resonant linearized conductance g_2, the time constant τ_2 of the resonant gating variable, the linearized leak conductance $g_{L,2}$ and the gap junction coefficient g_c. Increasing values of g_2 attenuate the $K(f)$ profiles and increase the K-resonant frequency $f_{res,K}$ (Fig. 6-A1 to -C1). Increasing values of g_c attenuate the $K(f)$ profile with no significant change in $f_{res,K}$ (Fig. 6-A1 to -C1). Increasing values of τ_2 shift $f_{res,K}$ to lower values, amplify the $K(f)$ profiles and make the peakier (compare (Figs. 6-A1 and B1). Increasing values of $g_{L,2}$ attenuate the $K(f)$ profiles and make them shallower, with no significant differences in $f_{res,K}$ (compare (Figs. 6-A1 and C1).

Figs. 6-B1 to -D1 show the dependence of the $\Delta\Phi$-profiles on g_2, τ_2, $g_{L,2}$ and g_c. Increasing values of g_2, shift the phasonant frequency f_{phas} to the right and make the changes in the $\Delta\Phi$-profiles more pronounced, particularly for the lower frequencies (Fig. 6-A2 to -C2). For the parameter values in Fig. 6-A and $g_2 = 0.1$, the system exhibits K-resonance, but not $\Delta\Phi$-phasonance (solid blue). Increasing values of g_c decreases the rate of change of the $\Delta\Phi$ profiles. Increasing values of τ_2 shift f_{phas} to lower values (compare (Figs. 6-A2 and B2). Increasing values of $g_{L,2}$ has a similar effect as increasing the values of g_c (compare (Figs. 6-A2 and C2).

3.3 Response to oscillatory inputs: Electrically coupled linearized $\mathbf{I_{Nap}}$ + $\mathbf{I_h}$ and $\mathbf{I_{Nap}}$ + $\mathbf{I_{Ks}}$ cells

We now turn to the analysis of the dependence of the $K(f)$ and $\Delta\Phi(f)$ profiles of biophysically plausible electrically coupled (nonlinear) cells on their biophysical constitutive properties by using the results for the electrically coupled linear resonators discussed above. We primarily focus on the K-resonant and $\Delta\Phi$-phasonant properties. The I_{Nap} + I_h and I_{Nap} + I_{Ks} models and their dynamics are described in Section 2.3 (see also Sections S1.1 and Fig. S4). The linearized I_{Nap} + I_h and I_{Nap} + I_{Ks} models have the form (1)- (2) with g_L and g ($g_{L,2}$ and g_2) defined by eqs. (S14) and (S15) in terms of the biophysical parameters of the corresponding nonlinear models. Our results are presented in Figs. 8 and 10 (I_{Nap} + I_h model) and Figs. 10 and 11 (I_{Nap} + I_{Ks} model). Fig. 7 shows the results for the I_{Nap} model, a reduced model lacking the slower negative feedback currents.

While both I_h and I_{Ks} are resonant, I_h is hyperpolarization-activated and depolarizing, while I_{Ks} is depolarization-activated and hyperpolarizing (Fig. S1). These differences are reflected in the geometry of the phase-plane diagram, which are qualitatively mirror images of each other (Figs. S4, S1.2.4 and S6-A1). The parabolic V-nullclines are concave up for the I_{Nap} + I_h model (e.g., Fig. S4-A3, Fig. S6-A1) and concave down for the I_{Nap} + I_{Ks} model (e.g.,

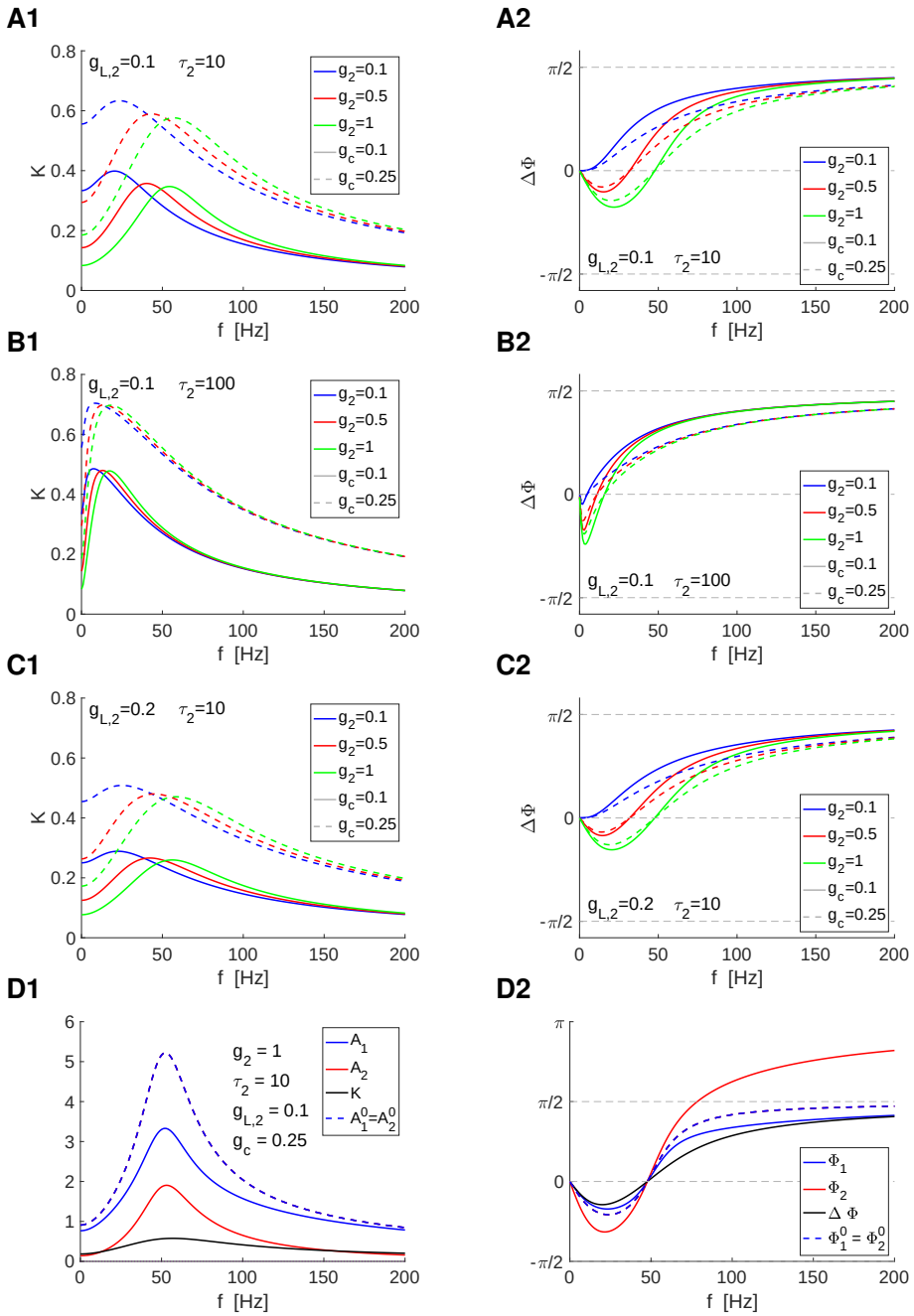

Figure 6: **Response of two electrically coupled resonators to oscillatory inputs for representative parameter values.** The linear model is given by eqs. (1)-(2). The pre-J and post-J cells (1 and 2, respectively) are identical. **A1, B1, C1.** Coupling coefficients $K(f)$ given by eq. (28). **A2, B2, C2.** Phase-difference coefficient $\Delta\Phi(f)$ given by eq. (29). **D.** Network amplitude (A_1 and A_2, panel D1) and phase (Φ_1 Φ_2, panel D2) responses computed from the complex responses $\mathbf{A_1}$ and $\mathbf{A_2}$ given by eqs. (7)-(8) for the parameter values used for the solid-green curves in panels A. Superimposed to these profiles are the amplitudes of the individual cells (A_1^0 and A_2^0, dashed-blue in panel D1) and the coupling coefficient K (panel D1), and the phase of the individual cells (Φ_1^0 and Φ_2^0, dashed-blue in panel D2) and the phase-difference coefficient $\Delta\Phi$ (panel D2).

Fig. S1.2.4-A3, Fig. S6-B1). In previous work [21, 66], we showed that these differences translate to differences in some of the models' oscillatory properties. Here we examine the $K(f)$ and $\Delta\Phi(f)$ profiles for the two models when electrically coupled and their dependence on the model parameters, and uncover the differences between the two models particularly in the parabolic-like nonlinear regimes.

The excitability level is determined by a combination of the model parameters. For relatively low excitability levels, the fixed-point is relatively far away from the knee of the V-nullcline and the system is in a quasi-linear regime (e.g., Figs. S4-A1 and -A2 and Figs. S1.2.4-A1 and -A2). As the excitability level increases, the fixed-point first moves towards the knee of the V-nullcline and the parabolic-like nonlinearities become increasingly dominant (e.g., Figs. S4-A3 and S6-A1 and Figs. S1.2.4-A3 and Fig. S6-B1), particularly so in a close vicinity of the bifurcation that produces the onset of spikes. This is reflected in the linearized conductances g_L and g ($g_{L,2}$ and g_2) both explicitly and implicitly through the equilibrium $\bar{V}$. Importantly, changes in G_h or G_q (maximal conductances associated to the resonant currents) explicitly affect both linearized conductances, while changes in G_p (maximal conductance associated to the amplifying current) explicitly affects only the linearized leak conductance g_L.

3.3.1 Linearized $\mathbf{I_{Nap}}$ model

The I_{Nap} model (Sections 2.3 and S1.2) is a nonlinear 1D model extending the passive cell to include I_{Nap} (nonlinear, instantaneously fast). The dynamics of the I_{Nap} model are illustrated in Fig. S2.

The passive cell can be thought of as the linearization of the I_{Nap} model with

$$g_L = G_L + G_p\, p_\infty(\bar{V}) + G_p\, p'_\infty(\bar{V})\,(\bar{V} - E_{Na}) \tag{30}$$

where G_L and G_p are the leak and persistent sodium maximal conductances of the original biophysical model and $\bar{V}$ is the equilibrium voltage in the subthreshold regime (if it exists). The last term in eq. (30) is negative, characterizing the amplifying nature of the I_{Nap} gating variable.

We analyze the dependence of the K- and $\Delta\Phi$-profiles as well as cells' response profiles on the model parameters G_L and G_p (to the linear level of approximation) by analyzing the dependence of g_L on these parameters both directly and indirectly through the changes they produced on the equilibrium $\bar{V}$.

The dependence of g_L on G_L is straightforward. The dependence of g_L on G_p involves two terms with opposite signs, positive (second) and negative (third). While g_L increases linearly with G_L, it decreases with increasing values of G_p (Fig. 7) because of the dominance of the last term over the second one. Geometrically, the dV/dt vs. V curve becomes shallower as G_p increases. Therefore, increasing values of G_p has the same effect on the network response profiles as decreasing values of g_L in Fig. 3. In particular, increasing values of G_p produces the expected amplification of the K-profiles and cause the increase of the $\Delta\Phi$ profiles to be more pronounced.

3.3.2 Linearized $\mathbf{I_{Nap}}$ + $\mathbf{I_h}$ model

A summary of our findings is presented in Tables 2 and 3 (middle columns). Briefly, increasing levels of I_{app} cause the model to transition from the quasi-linear to the parabolic-like regimes as the fixed-point moves up along the left branch of the V-nullcline towards its knee. As this happens, both g_L and g decrease (Figs. 8-B and -C) for fixed values of G_h and G_p. Increasing values of I_{app} cause an amplification of the $K(f)$ profiles (Figs. 9-A1 and -B1), a decrease in the K-resonant frequencies, and a slight increase in the $\Delta\Phi(f)$ profiles (Figs. 9-A2 and -B2). This is more pronounced for $G_p = 0.5$ than for $G_p = 0.1$ (compare Figs. 9-A1 and -B1). Increasing values of G_p also cause both g_L and g decrease (Figs. 8-A) and therefore the effects are similar to increasing values of I_{app} (compare Figs. 9-A and -B).

The nonlinear effects become apparent for the largest values of I_{app} and G_p for which the fixed-point of the individual cells is located in a close vicinity of the knee of the parabolic-like nullcline, while for lower values of I_{app} and G_p the system is in a quasi-linear regime.

The dependence of the linearized conductances with G_h is more complex. Increasing values of G_h cause an increase in g for all values of G_p as expected from a resonant conductance (a maximal conductances associated to a

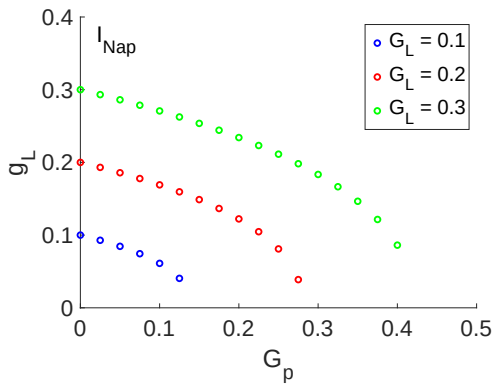

Figure 7: $\mathbf{I_{Nap}}$ **model: Dependence of the linearized conductance** $\mathbf{g_L}$ **on the biophysical conductances** $\mathbf{G_p}$ **and** $\mathbf{G_L}$. We used eq. (30) with the parameter values presented in Section S1.2 and $I_{app} = 0$.

resonant current) (Fig. 8-A2). However, the dependence of g_L with G_h switches for some intermediate value of G_p. For the higher values of G_p, g_L decreases with increasing values of G_h (from light-salmon to blue in Fig. 8-A1) for the higher values of G_p, while for the lower values of G_p, g_L increases with increasing values of G_h. This behavior implies that the K-profile is nonlinearly amplified by increasing values of G_h for the higher values of G_p (Fig. 9-C1, solid), while it is attenuated by increasing values of G_h for the lower values of G_p where the model is quasi-linear (Fig. 9-C1, dashed). Similarly, as G_h increases, the K-resonant frequency decreases for the higher values of G_p and increases for the lower values of G_p. A qualitatively switch in behavior occurs for the $\Delta\Phi$-profiles (Fig. 9-C2).

In other words, the presence of I_{Nap} in the nonlinear regime causes the resonant current I_h to amplify the K-profile, while it would otherwise attenuate it in the quasi-linear regime where the levels of I_{Nap} are lower.

3.3.3 Linearized I_{Nap} + I_{Ks} model

A summary of our findings is presented in Tables 2 and 3 (right columns). Briefly, increasing levels of I_{app} cause the individual neurons to transition from quasi-linear to parabolic-like as the fixed-point moves down along the left branch of the V-nullcline towards its knee. As this happens, g_L decreases for the higher values of G_p (Fig. 10-B1) and increases for the lower values of G_p (Fig. 10)-C1), while g increases for all values of G_p (Fig. 10)-B2 and -C2). This behavior is qualitatively similar for fixed representative values of G_q and G_p although in some cases the dependencies with I_{app} are weak. As I_{app} increases for the higher values of G_p, the K-profiles are amplified for the higher values of G_q (Fig. 11-A1, solid) and attenuated for the lower values of G_q (Fig. 11-A1, dashed). In contrast, for the lower values of G_p, the K-profiles are attenuated for all values of G_q as I_{app} increases (Fig. 11-B1). In both cases, the K-resonant frequency increases with increasing values of I_{app}. A similar type of switch can be observed in the $\Delta\Phi$-profiles although they are minimally affected and the differences are almost imperceptible (Figs. 11-A2 and -B2).

For fixed values of I_{app} and G_p, both g_L and g increase with increasing values of G_q (Fig. 10-A to -C). The K-profiles are attenuated and the K-resonant frequency increases with increasing values of G_q (Fig. 11-C1). For fixed values of I_{app} and G_q, both g_L and g increase with increasing values of G_p (Fig. 10-A1). As expected, the K-profiles are amplified by increasing values of G_p (Fig. 11-C1).

Note that for certain parameter regimes the $\Delta\Phi(f)$ profile is always positive and therefore the network does not

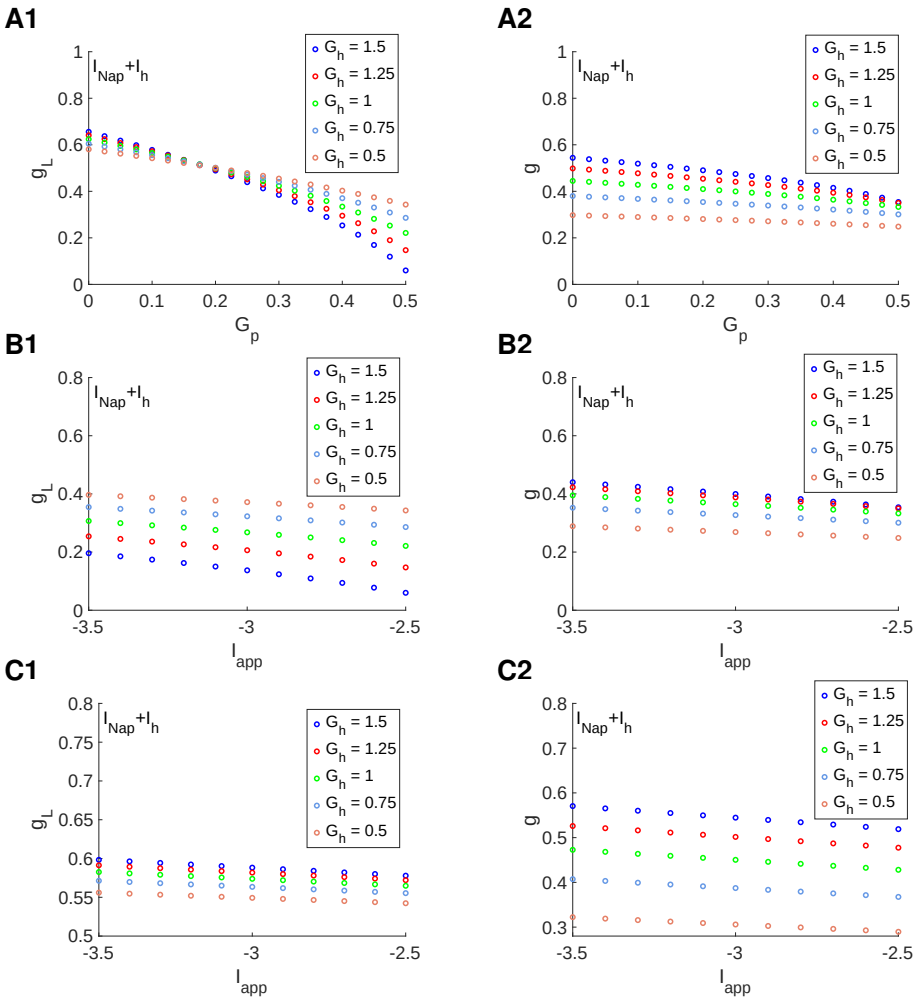

Figure 8: **Dependence of the linearized conductances ($\mathbf{g_L}$ and $\mathbf{g}$) on the biophysical maximal conductances ($\mathbf{G_p}$ and $\mathbf{G_h}$) and $\mathbf{I_{app}}$ for the $\mathbf{I_{Nap}}$+$\mathbf{I_h}$ model for representative parameter values.** We used the biophysical model (S1)-(S2) with the parameter values presented in Section S1.2 and linear model (1)-(2). The linearization process is described in Section S1.3 **A.** g_L and g as a function of G_p and G_h for $G_L = 0.5$ and $I_{app} = -2.5$. **B.** g_L and g as a function of I_{app} for $G_L = 0.5$ and $G_p = 0.5$. **C.** g_L and g as a function of I_{app} for $G_L = 0.5$ and $G_p = 0.1$.

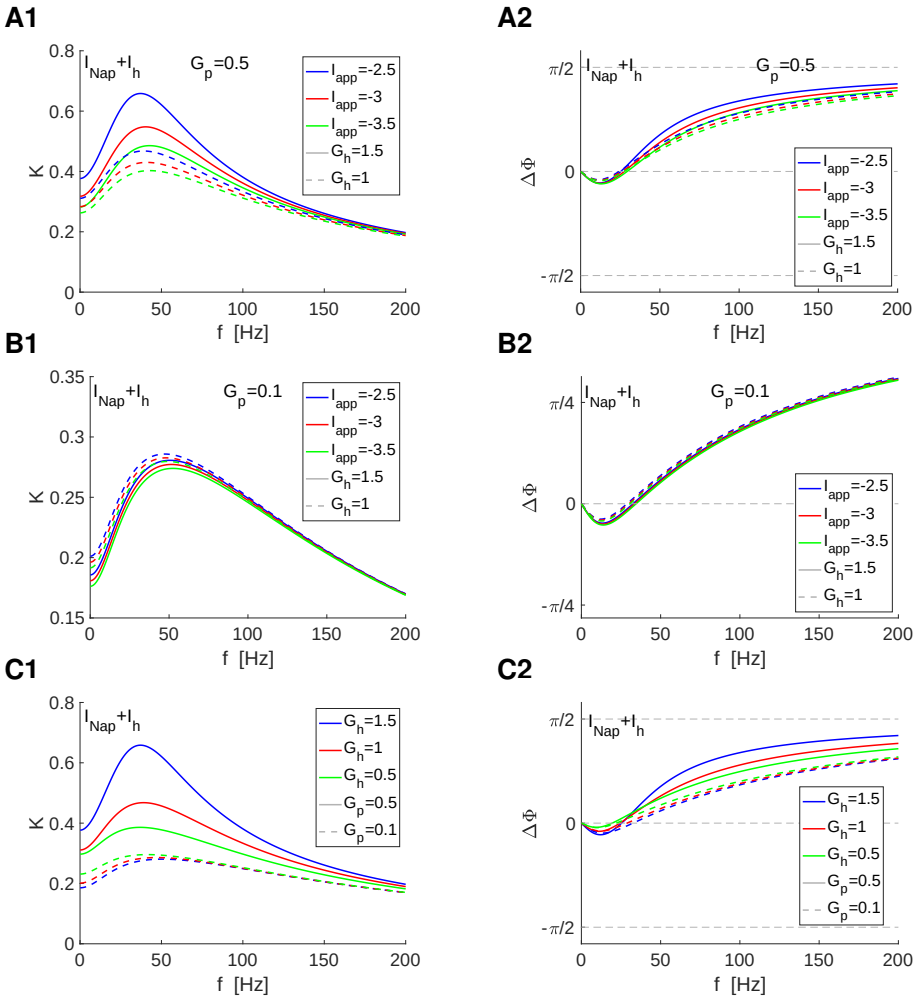

Figure 9: **$\mathbf{K}$- and $\mathbf{\Delta\Phi}$- profiles for the $\mathbf{I_{Nap}}$ + $\mathbf{I_h}$ model for representative parameter values.** We used eqs. (28)- (29) for the biophysical I_{Nap} + I_h model (S1)-(S2) with the parameter values presented in Section S1.2. The linearization process leading to the linearized model (1)-(2) is described in Section S1.3. **Left column.** K-profiles. **Right column.** $\Delta\Phi|$-profiles. **A.** $G_p = 0.5$, $G_L = 0.5$. **B.** $G_p = 0.1$, $G_L = 0.5$. **C.** $I_{app} = -2.5$, $G_L = 0.5$.

exhibit $\Delta\Phi$-phasonance (e.g, Fig. 11-B2).

3.3.4 The electrically coupled $\mathbf{I_{Nap}}$ + $\mathbf{I_h}$ and $\mathbf{I_{Nap}}$ + $\mathbf{I_{Ks}}$ cells have different response properties that are captured by the linearized models

Together, the results of the previous two sections highlight the fact that although the two biophysical models involve the interplay of resonant and amplifying currents, there exist significant qualitative differences between the models' $K(f)$ and $\Delta\Phi(f)$ profiles and their dependence with the model parameters and levels of excitability. As expected, the two biophysical models have a relatively similar dependence with the levels of the participating currents (model parameters) in the quasi-linear regimes where the excitability levels are relatively low and the behavior is dominated by the resonant currents (I_h and I_{Ks}). However, this changes significantly when the excitability levels are higher and the models are in a nonlinear, parabolic-like regime in the presence of higher levels of I_{Nap}. In these regimes, the synergistic interaction between the resonant and amplifying currents produce unexpected results that cannot be predicted from the quasi-linear behavior nor from the nature of the resonant currents such as the amplifying effects of the resonant current I_h. The similarities and differences between the two models are summarized in Tables 2 and 3.

As X increases		
	I_{Nap} + I_h	I_{Nap} + I_{Ks}
X = I_{app}	- g_L decreases (Fig. 8-B1, -C1)	- g_L decreases for the higher values of G_p (Fig. 10-B1) - g_L increases for the lower values of G_p (Fig. 10-C1)
	- g decreaes (Fig. 8-B2, -C2)	- g increases for all values of G_p (Fig. 10-B2, -C2)
X = G_h / G_q	- g_L decreases for the higher values of G_p (Fig. 8-B1) - g_L increases for the lower values of G_p (Fig. 8-C1)	- g_L increases for all values of G_p (Fig. 10-B1, -C1)
	- g increases for all values of G_p (Fig. 8-B2, -C2)	- g increases for all values of G_p (Fig. 10-B2, -C2)
X = G_p	- g_L decreases for all values of G_h (Figs. 8-A1)	- g_L decreases for all values of G_q (Fig. 10-A1)
	- g decreases for all values of G_h (Figs. 8-A2)	- g increases for all values of G_q (Fig. 10-A2)

Table 2: **Dependence of the linearized conductances $\mathbf{g_L}$ and $\mathbf{g}$ on the biophysical parameters $\mathbf{I_{app}}$, $\mathbf{G_p}$, and $\mathbf{G_h}$ / $\mathbf{G_q}$.**

3.4 Electrically coupled two-compartmental models of spatially extended neurons: Effects of asymmetry in the connectivity

Here, we extend our investigation to two-compartment neuron models having asymmetric connectivity and network heterogeneity. More specifically, we consider two-compartment models of linear or linearized cells where the oscillatory input arrives only to one of the compartments (indexed by 1). The coupling coefficient $K(f; g_c/\sigma_2) = g_c/\sigma_2\, \hat{Z}_2^0(f; g_c/\sigma_2)$ and the phase-difference coefficient $\Delta\Phi(f; g_c/\sigma_2) = \hat{\Phi}_2^0(f; g_c/\sigma_2)$ for two-compartment linear models are presented in Section 2.7 where $\hat{Z}_2^0$ and $\hat{\Phi}_2^0$ are the extended impedances of the individual (disconnected) compartments. Both depend on the ratio of g_c/σ_2 where g_c represents the factor in the coupling strength between the two compartments

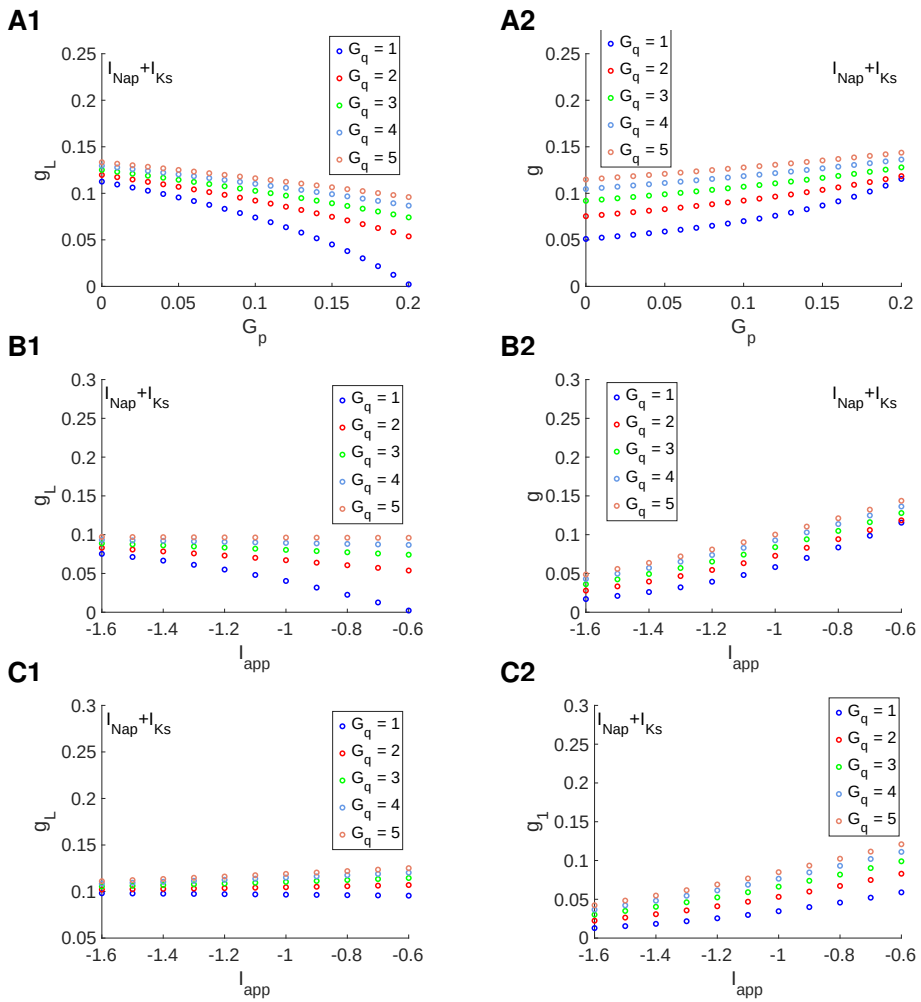

Figure 10: **Dependence of the linearized conductances ($\mathbf{g_L}$ and $\mathbf{g}$) on the biophysical maximal conductances ($\mathbf{G_p}$ and $\mathbf{G_q}$) and $\mathbf{I_{app}}$ for the $\mathbf{I_{Nap}}$+$\mathbf{I_{Ks}}$ model for representative parameter values.** We used the biophysical model (S1)-(S2) with the parameter values presented in Section S1.2 and linear model (1)-(2). The linearization process is described in Section S1.3 **A.** g_L and g as a function of G_p and G_q for $G_L = 0.1$ and $I_{app} = -0.6$. **B.** g_L and g as a function of I_{app} for $G_L = 0.1$ and $G_p = 0.2$. **C.** g_L and g as a function of I_{app} for $G_L = 0.1$ and $G_p = 0.05$.

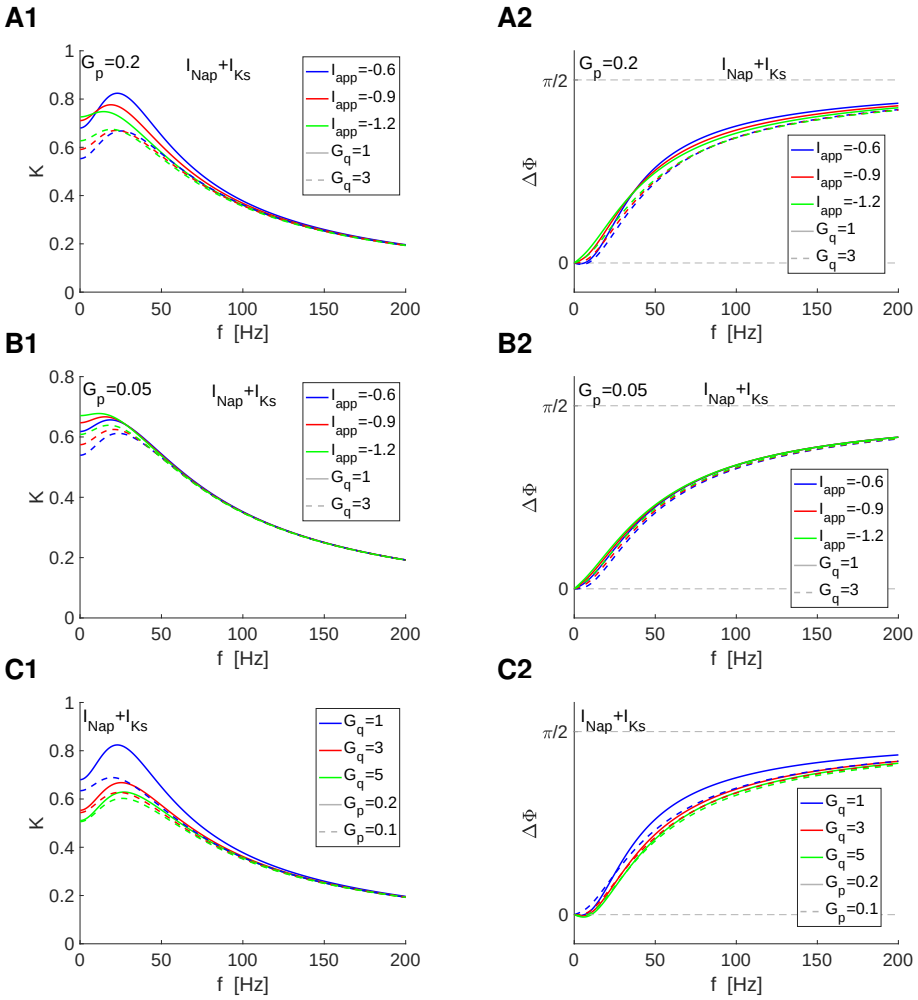

Figure 11: **$\mathbf{K}$- and $\mathbf{\Delta\Phi}$- profiles for the $\mathbf{I_{Nap}}$ + $\mathbf{I_{Ks}}$ model for representative parameter values.** We used eqs. (28)- (29) for the biophysical I_{Nap} + I_{Ks} model (S1)-(S2) with the parameter values presented in Section S1.2. The linearization process leading to the linearized model (1)-(2) is described in Section S1.3. **Left column.** K-profiles. **Right column.** $\Delta\Phi|$-profiles. **A.** $G_p = 0.2$, $G_L = 0.1$. **B.** $G_p = 0.05$, $G_L = 0.1$. **C.** $I_{app} = -0.6$, $G_L = 0.1$.

As X increases		
	I_{Nap} + I_h	I_{Nap} + I_{Ks}
X = I_{app}	- $K(f)$ is amplified (Fig. 9-A1, -B1)	- $K(f)$ is amplified for the lower values of G_q and the higher values of G_p (Fig. 11-A1, solid) - $K(f)$ is attenuated for the higher values of G_q and the higher values of G_p (Fig. 11-A1, dashed) - $K(f)$ is attenuated for all values of G_q and the lower values of G_p (Fig. 11-B1)
	- $f_{res,K}$ decreases (Fig. 9-A1, -B1)	- $f_{res,K}$ increases for the higher values of G_p (Fig. 11-A1, -B1)
	- $\Delta\Phi(f)$ increases (Fig. 9-A2, -B2)	- $\Delta\Phi(f)$ decreases for the lower values of f and increases for the higher values of f (Figs. 11-A2)
	- $f_{phas,K}$decreases (Fig. 9-A2, -B2)	- $f_{phas,K}$ increases* (Fig. 11-A2, -B2)
X = G_h / G_q	- $K(f)$ is amplified for the higher values of G_p (Figs. 9-C1,solid) - $K(f)$ is attenuated for the lower values of G_p (Figs. 9-C1, dashed)	- $K(f)$ is attenuated (Fig. 11-C1)
	- $f_{res,K}$ first increases and then decreases for the higher values of G_p (Figs. 9-C1,solid) - $f_{res,K}$ increases for the lower values of G_p (Figs. 9-C1, dashed)	- $f_{res,K}$ increases (Fig. 11-C1)
	- $\Delta\Phi(f)$ increases for the higher values of G_p (Figs. 9-C2, solid) - $\Delta\Phi(f)$ decreases for the lower values of G_p (Figs. 9-C2, dashed)	- $\Delta\Phi(f)$ decreases (Fig. 11-C2)
	- $f_{phas,K}$ increases (Figs. 9-C2)	- $f_{phas,K}$ increases* (Figs. 11-C2)
X = G_p	- $K(f)$ is amplified (Figs. 9-C1)	- $K(f)$ is amplified (Figs. 11-C1)
	- $f_{res,K}$ decreases (Figs. 9-C1)	- $f_{res,K}$ increases (Figs. 11-C1)
	- $\Delta\Phi(f)$ increases (Figs. 9-C2)	- $\Delta\Phi(f)$ decreases for the lower values of f and increases for the higher values of f (Figs. 11-C2)
	- $f_{phas,K}$ decreases (Figs. 9-C2)	- $f_{phas,K}$ increases* (Figs. 11-C2)

Table 3: **Dependence of the properties of the K profile on the biophysical parameters $\mathbf{I_{app}}$, $\mathbf{G_p}$, and $\mathbf{G_h}$ / $\mathbf{G_q}$.** When appropriate, the changes in $\Delta\Phi$ are reported in absolute value. * When it exists (there are parameter regimes for which $\Delta\Phi(f)$ is always positive).

that is common to both and σ_2 represents the proportion of the total cell are taken up by compartment 2. Specific expressions for these quantities can be computed from eqs. (26) and (27), respectively, when compartment 2 is passive, and by eqs. (28) and (29), respectively when compartment 2 is a 2D resonator.

Because these quantities depend on the quotient g_c/σ_2, it is enough to examine $g_c\,\hat{Z}(f;g_c)$ and $\hat{\Phi}(f;g_c)$ for varying values of g_c and arbitrary extended shapes of the impedance and phase profiles. As mentioned above, the dependence of these expressions on g_c consist of a deformation and an additional rescaling by the same quantity (g_c) for the firsts one. The results of the previous sections for electrically coupled cells extend to two-compartment models in

a straightforward way by performing these operations. They do not affect the relative values of the profiles nor the mechanisms by which they are generated.

As g_c increases, $g_c\,\hat{Z}(f;g_c)$ is amplified and becomes shallower (Fig. 12-A1 to -C1) and $\hat{\Phi}(f;g_c)$ decreases in absolute value (Fig. 12-A2 to -C2). The dependence of these quantities with σ_2 can be inferred from these results for fixed values of g_c as σ_2 decreases. We note that the primary effect of increasing g_c on these extended quantities is to attenuate the impedance profile (Fig. S7-A1 to -C1) and make it shallower, and to decrease (in absolute value) the phase profile (Fig. S7-A1 to -C1).

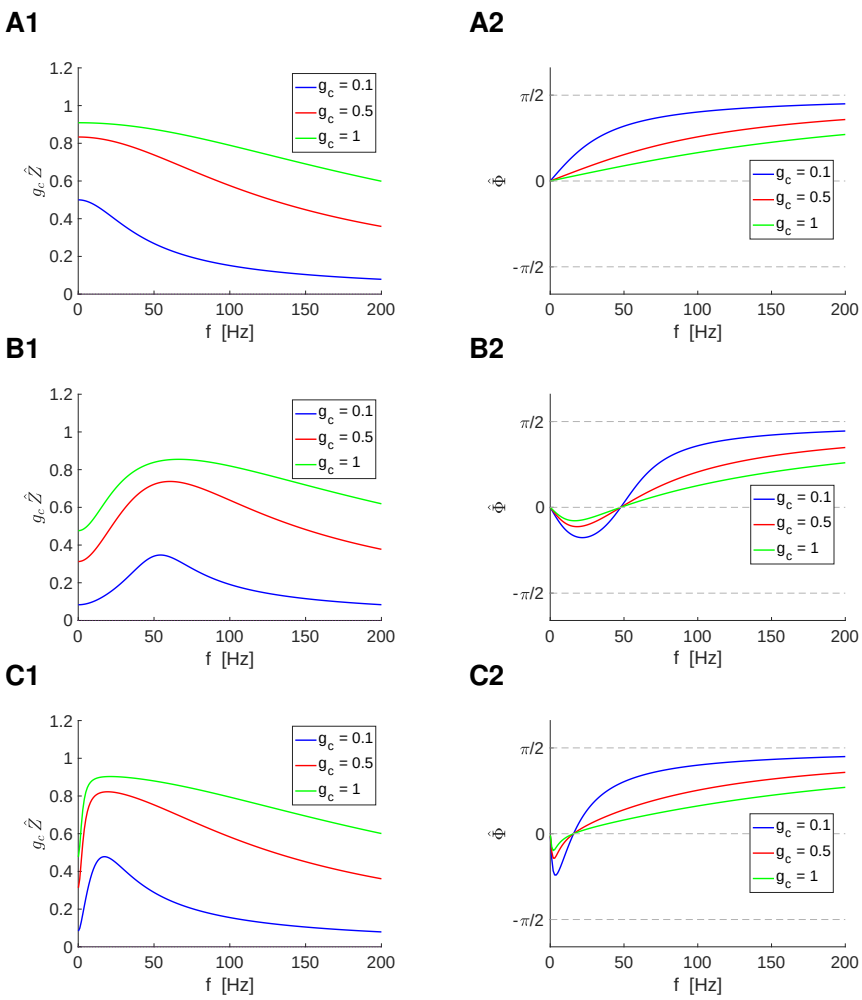

Figure 12: **Extended impedance $\hat{Z}(f,g_c)$ multiplied by g_c and phase $\hat{\Phi}(f,g_c)$ profiles.** We used eqs. (S53)-(S54). For $g=0$, these eqs. reduce to eqs. (S55)- (S56). These quantities are equivalent to the coupling coefficients $K(f)$ and phase-difference coefficient $\Delta\Phi$. **Left columns.** Extended impedance profiles multiplied by g_c. **Right columns.** Extended phase profiles. **A.** $g=0$. **B.** $g=1$, $\tau=10$. **C.** $g=1$, $\tau=100$. We used the additional parameter value: $g_L=0.1$.

3.5 Nonlinear models: The coupling and phase-difference coefficients depend on the interplay of both the pre- and post-J cells

For linear models, both the $K(f)$ and $\Delta\Phi(f)$ profiles depend on the properties of the post-J cell, and are independent of the properties of the pre-J cell and the input amplitude. Analytical results for electrically coupled weakly nonlinear cells show that both the pre- and post-J cell and the input amplitude contribute to shape these two profiles (see Section

S4). Here we test how the $K(f)$ and $\Delta\Phi(f)$ profiles are shaped by the intrinsic nonlinearities of quadratic type (Section 2.2; Fig. 3, Fig. S3) in the pre-J and post-J cells and the input amplitude.

We use the quadratic model (3)-(4) where the connectivity parameters are $g_{c,k} = g_c$ for electrically coupled cells mediated by gap junctions and $g_{c,k} = g_c/\sigma_k$ for two-compartmental models. For the 1D reduced model (no negative feedback), we use a slightly modified version of the model, which is described below. The description of the quadratization process linking the parameters of the quadratic models with these of biophysical models with nonlinearities of parabolic-type in the voltage equation is presented Section S1.4 [70–72].

3.5.1 Electrically coupled 1D quadratic cells: interplay of nonlinear LPFs

For cells with 1D quadratic dynamics, the electrically coupled cell model reads

$$\tau_k \frac{dv_k}{dt} = a_k\, v_k^2 + I_k + g_{c,k}\,(v_j - v_k) + I_{in,k}(t) \tag{31}$$

for $k, j = 1, 2,\ k \neq j$ where I_k represents the level of excitability, and a_k captures the effect of an instantaneously fast amplifying current (e.g., I_{Nap}). As before, the time-dependent oscillatory inputs are given by eq. (5) with $I_{in,2} = 0$.

In the presence of I_{Nap} the cell develops nonlinearities of parabolic-type (Fig. S2). For relatively low levels of I_{Nap}, the nonlinearities are away from the equilibrium and therefore the systems is quasi-linear. As the levels of I_{Nap} increase, the equilibrium becomes closer to the knee of the parabolic nullcline and to the unstable fixed-point (who serves as a threshold for spike generation when the model is supplemented with a spiking mechanism). For a critical level of I_{Nap}, the two fixed-points collide in a bifurcation and disappear. In the quadratic models, the excitability levels are represented by the DC current I_k.

The quadratic 1D model is the subthreshold description of the well-known quadratic integrate-and-fire model [79, 80, 90, 91]. Fig. S3 illustrates the dynamics of an individual quadratic cell ($g_c = 0$ and I representing the DC current). As I increases, the speed (dV/dt vs. V) curve increases, the fixed-point moves to the right and the range of values of v for which the response to oscillatory inputs remains in the subthreshold regime shrinks. We choose values of A_{in} so that the response for all input frequencies remains in the subthreshold regime. The effects of the nonlinearities are apparent in the asymmetry, non-sinusoidal shape of the voltage response (compare the response waveforms in Figs. S3-A2 and -B2 and the V_{max} and V_{min} envelope responses in Figs. S3-A3 and -B3).

In Fig. 13 we compare the $K(f)$ and $\Delta\Phi(f)$ profiles for two identical connected cells (blue) and two different connected cells (red) where cell 2 is the same as for the identical pair and cell 1 has the same parameter values as cell 2, except for one that varies across panels. If the model were linear, we would expect the resulting graphs to be superimposed. The differences observed in Fig. 13 indicate that the $K(f)$ and $\Delta\Phi(f)$ profiles are determined by the interplay of both participating cells. These differences are stronger for the $K(f)$ than for the $\Delta\Phi(f)$ profiles. For the $K(f)$ profiles, the differences are stronger for the lower frequencies and decrease as the frequency increases. Because the two cells are network LPFs (not shown) their voltage response range shrinks as the input frequency increases. For the higher frequencies, the response trajectory (e.g., blue line in Fig. S3) reaches the region where the parabolic nonlinearities are prominent. For the lower frequencies, the response trajectory remains in a close vicinity of the fixed point where the dynamics are quasi-linear. These results persists for two-compartment models (not shown).

3.5.2 Electrically coupled 2D quadratic cells with negative feedback effects: interplay of nonlinear BPFs, LPFs and time scales

Figs. 14 llustrates the nonlinear (amplitude) BPFs (panels A1, C1, D1) and LPFs (panel B1) for the quadratic model for an individual cell for representative parameter values. In addition to resonance, the BPF's systems exhibit phasonance (panels A2, C2, D2), while the LPF's system exhibits no phasonance (panel B2). The filters' nonlinearity is apparent in the lack of symmetry of the peak (upper) and trough (lower) envelopes with respect to the equilibrium (gray dashed horizontal line) and the lack of proportionality with respect to the input amplitude A_{in} (e.g., Fig. 14 -A1, compare the

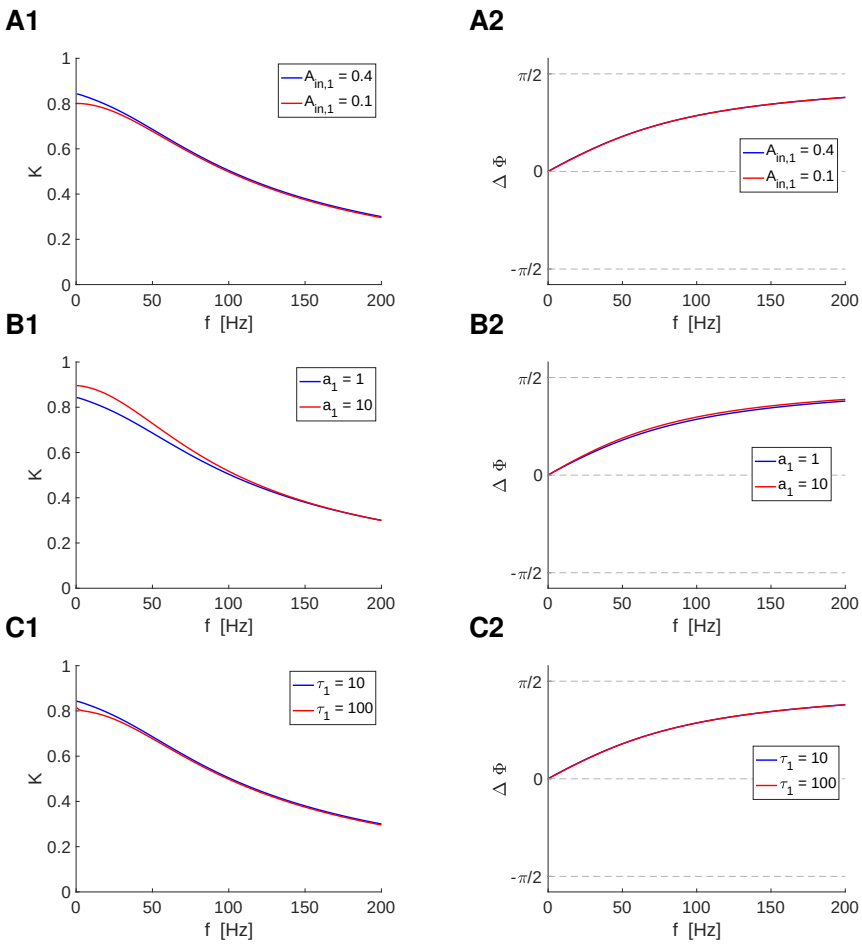

Figure 13: **Electrically coupled quadratic 1D model: Effects of the pre-J cell's properties on the response profiles.** We used the model (31) for the electrically coupled pre- and post-J cells with quadratic nonlinearities (cell 1 is the pre-J cell; $A_{in,2} = 0$) mediated by gap junctions ($g_c = 0.5$). The parameter values for the two cells are identical, except for the ones indicated in the legends. **Left column.** K profiles **Right column.** $\Delta\Phi$ profiles **A.** $a_1 = a_2 = 1$, $\tau_1 = \tau_2 = 10$. **B.** $\tau_1 = \tau_2 = 10$, $A_{in,1} = 0.4$. **C.** $a_1 = 1 = a_2 = 1$, $A_{in,1} = 0.4$. We used the following additional parameter values: $I_1 = I_2 = -0.25$ and $g_c = 4$

solid-blue response to $A_{in} = 0.05$ and the dashed-blue response for $A_{in} = 0.01$). The effects of the model's quadratic nonlinearity are reflected in the shapes of the response limit cycles for the resonant frequency (Figs. 14-A3, solid) [71]. For smaller values of the input amplitude A_{in}, the response limit cycle remains in a close vicinity of the fixed-point (Figs. 14-A3, dashed) and the peak and trough envelopes are symmetric with respect to the equilibrium (Figs. 14-A1, dashed).

The presence of the model's nonlinearities do not necessarily imply a strongly nonlinear response such as the one in Fig. 14-A1 (solid) for $A_{in} = 0.05$. Not only because weakly nonlinear responses (quasi-linear filters) are obtained for lower values of A_{in} that are not necessarily small enough (e.g., Fig. 14-A1, dashed, for $A_{in} = 0.01$), but also because of other factors such as a small enough negative feedback time constant (higher value of ϵ) (e.g., Fig. 14-D1). Comparison between the BPFs in Figs. 14-A1 (solid) and 14-D1 (dashed), for the same value of A_{in} shows that the BPFs are more symmetric and more attenuated, the higher ϵ [71]. This is the result of the interplay of the oscillatory inputs and the underlying vector field [71] (compare Figs. 14-A3 and -D3). BPFs with a comparable peak value requires a higher value of A_{in} for $\epsilon = 0.1$ than for $\epsilon = 0.01$. An increase in the parabolic curvature a (Fig. 14-B3) produces a nonlinear response (Fig. 14-B1). However, the filter's amplitude is smaller as compared to the one for lower values of a (Fig. 14-A1) since the range of voltage values for which the response remains within the subthreshold voltage regime shrinks as a increases.

In our study, we use the parameter values leading to the amplitude BPF in Fig. 14 -A1 as the baseline parameter set ($a = 0.1$, $\alpha = 0.5$ and $\epsilon = 0.01$), and we compare a homogeneous network consisting of two identical baseline cells with heterogenous, mixed-cells networks where one cell is a baseline cell and the other has the same parameter values as the baseline cell, except for one. We use the representative parameter values in Figs. 14-B (increase in a, change in the parabolic nonlinearity), 14-C (decrease in α, LPF), and 14-D (increase in ϵ, change in the negative feedback time constant).

In Fig. 15 we test whether the $K(f)$ and $\Delta\Phi(f)$ profiles depend on the properties of the pre-J cell (Fig. 15-B - D) and the input amplitude A_{in} (Fig. 15-A) in addition to the post-J cell. To this end, we proceed as in the previous section and compare the $K(f)$ and $\Delta\Phi(f)$ profiles of a homogeneous and heterogeneous networks as described above. Our results demonstrate that the $K(f)$ and $\Delta\Phi(f)$ profiles depend on A_{in} and on the properties of the pre-J cell (in addition to the properties of the post-J cell). In some cases, the differences in the profiles between the homogeneous and heterogenous networks is significant, more so than for the quadratic 1D models discussed in the previous section. These differences are more prominent for the lower frequencies and the frequencies in the resonant frequency band where the response amplitude is larger and therefore the response trajectories in the phase-space diagram are able to reach the region of parabolic nonlinearities. For the input frequencies for which the response amplitude is smaller, the trajectories evolve in a closer vicinity of the fixed-point and therefore the dynamics is quasi-linear. In Fig. 14-C we observe that the $K(f)$ profile for the heterogenous network exhibits K-antiresonance in addition of K-resonance, and the $\Delta\Phi(f)$ profile exhibits $\Delta\Phi$-antiphasonance in addition to the $\Delta\Phi$-phasonance. This is the result of a network effect, since neither antiresonance nor antiphasonance are present in any of the participating cells (these phenomena require 3D cellular dynamics).

In Figs. 16 and 17 we extend our results and test the effects of the input location on the $K(f)$ and $\Delta\Phi(f)$ profiles for the heterogeneous networks investigated in Fig. 15. Because in our formulation, the input always arrives to the cell indexed by 1 (the pre-J cell), we switch the parameter values of cells 1 and 2. Specifically, the curves shown in these figures correspond to the homogeneous network of baseline cells (blue), and the two heterogeneous network where cell 2 (cell 1) is a baseline cell and cell 1 (cell 2) has the same parameter values as the baseline cell, except for one, which varies across panels (red and green, respectively). In all three cases in Fig. 16 the $K(f)$ and $\Delta\Phi(f)$ profiles depend on the properties of both the pre-J and post-J cell and are not necessarily dominated by the properties of the post-J cell. This persist for larger values of g_c (Figs. 17) and for two-compartment models where the effects of the compartments' area renders the connectivity asymmetric (Figs. 18 and 19).

For example, in Figs. 16-A, green, the post-J cell is a LPF and the Φ profile is monotonically increasing, but the $K(f)$ and $\Delta\Phi(f)$ profiles exhibit K-resonance and $\Delta\Phi$-phasonance. On the other hand, in Figs. 16-B (green) the $K(f)$ and $\Delta\Phi(f)$ profiles appear to be dominated by the amplitude and phase profiles of the post-J cell since they are

shifted to the right as compared to the other two cases (blue and red). However, the presence of antiresonance and antiphasonance in Figs. 16-B (red) are generated, as mentioned above, by a network mechanism. Similarly, in Figs. 16-C, green, the $K(f)$ and $\Delta\Phi(f)$ profiles are significantly different than the other two cases (blue and red).

Comparison among Figs. 16, 18 and 19 provide a picture of how the interplay of the neuronal biophysical properties and dendritic geometry shape the $K(f)$ and $\Delta\Phi(f)$ profiles. To aid in the comparison, Figs. S8, S9 and S10 shows a rearrangement of the panels shown in Figs. 16, 18 and 19. Each row in Figs. S8, S9 and S10 correspond to a value of σ for the same fixed set of biophysical parameter values.

4 Discussion

The coupling strength between nodes in electrically coupled networks receiving time-dependent inputs is frequency-dependent. The $K(f)$ and $\Delta\Phi(f)$ coupling coefficient (CC) profiles measure the degree to which the pre-J and post-J cells are coupled in terms of their response amplitude and phase profiles, which are shaped by the complex interaction between the biophysical and geometric properties of the participating nodes and the connectivity. The biophysical and dynamic mechanisms that govern the generation of the $K(f)$ and $\Delta\Phi(f)$ profiles were largely unknown beyond electrically coupled passive cells (but see [32, 43, 49, 51–53]), which are 1D and linear, and for which the $K(f)$ profile is a LPF and $\Delta\Phi$ profile is always positive and monotonically increasing [23–29, 36, 40, 41, 43, 44, 46–50]. In addition, for linear systems, the CC profiles are independent of the biophysical properties of the pre-J cell and the input amplitude. Whether and under what conditions the CC profiles exhibit preferred frequencies in response to oscillatory inputs (K-resonance and $\Delta\Phi$ phasonance) and how these profiles depend on the biophysical parameters of the pre-J and post-J cells remained elusive.

In this paper we set out to understand how CC profiles with more intricate frequency-filtering properties than these for passive cells emerge in the more complex electrically coupled networks where the pre-J and post-J nodes are higher-dimensional and nonlinear, and how these CC profiles are shaped by the biophysical properties of these nodes. 2D models incorporate the presence of cellular resonance and phasonance and the associated BPFs and mixed leading-lagging phase responses. Nonlinear models incorporate the dependence of the $K(f)$ and $\Delta\Phi(f)$ profiles on the properties of the pre-J cell and the input amplitude in addition to the properties of the post-J cell and the connectivity.

We used biophysical modeling, numerical simulations, analytical calculations and dynamical systems tools to address these issues. We focused on gap junction connected networks and compartmental models of spatially extended neurons, which belong to the same family of electrically coupled network. The connectivity for gap junction networks is symmetric. Asymmetric connectivity arises in two-compartment models with heterogeneous spatial geometry.

We considered minimal network architectures consisting of two electrically connected nodes receiving oscillatory inputs (Fig. 2). The individual nodes (when disconnected) were either LPFs (e.g., passive cells; Fig. 1-A1) or BPFs (e.g., resonators; Fig. 1-A2) and their phase responses were positive (e.g., passive cells; Fig. 1-C1) or mixed negative-positive (e.g., phasonators; Fig. 1-C2). These choices allowed us to systematically investigate the biophysical and dynamic mechanisms that shape the CC profiles and determine their preferred coupling frequencies ($f_{res,K}$ and $f_{phas,K}$) in several representative scenarios where the same or different types of cellular filters interact. While gap junction connected networks typically involve the same type of pre-J and post-J neuron with the same biophysical properties, compartmental models may involve compartments with heterogeneity in their intrinsic properties [55, 92].

Linear models are amenable to analytical calculations, which we used to understand how the $K(f)$ and $\Delta\Phi(f)$ profiles are shaped by the participating building blocks (e.g., ionic conductances controlling the negative and positive feedback effects) and cellular filtering properties. The $K(f)$ and $\Delta\Phi(f)$ profiles for passive cells transition to BPFs and mixed negative-positive, respectively, in the presence of an added negative feedback term, which transform the nodes into resonators (2D). The shape of these CC profiles are modulated by the linearized leak and negative feedback conductances and the negative feedback time constant, which control the corresponding filtering properties of the post-J cell.

Armed with these results and knowledge, we investigated the dynamics of nonlinear neurons with biophysically

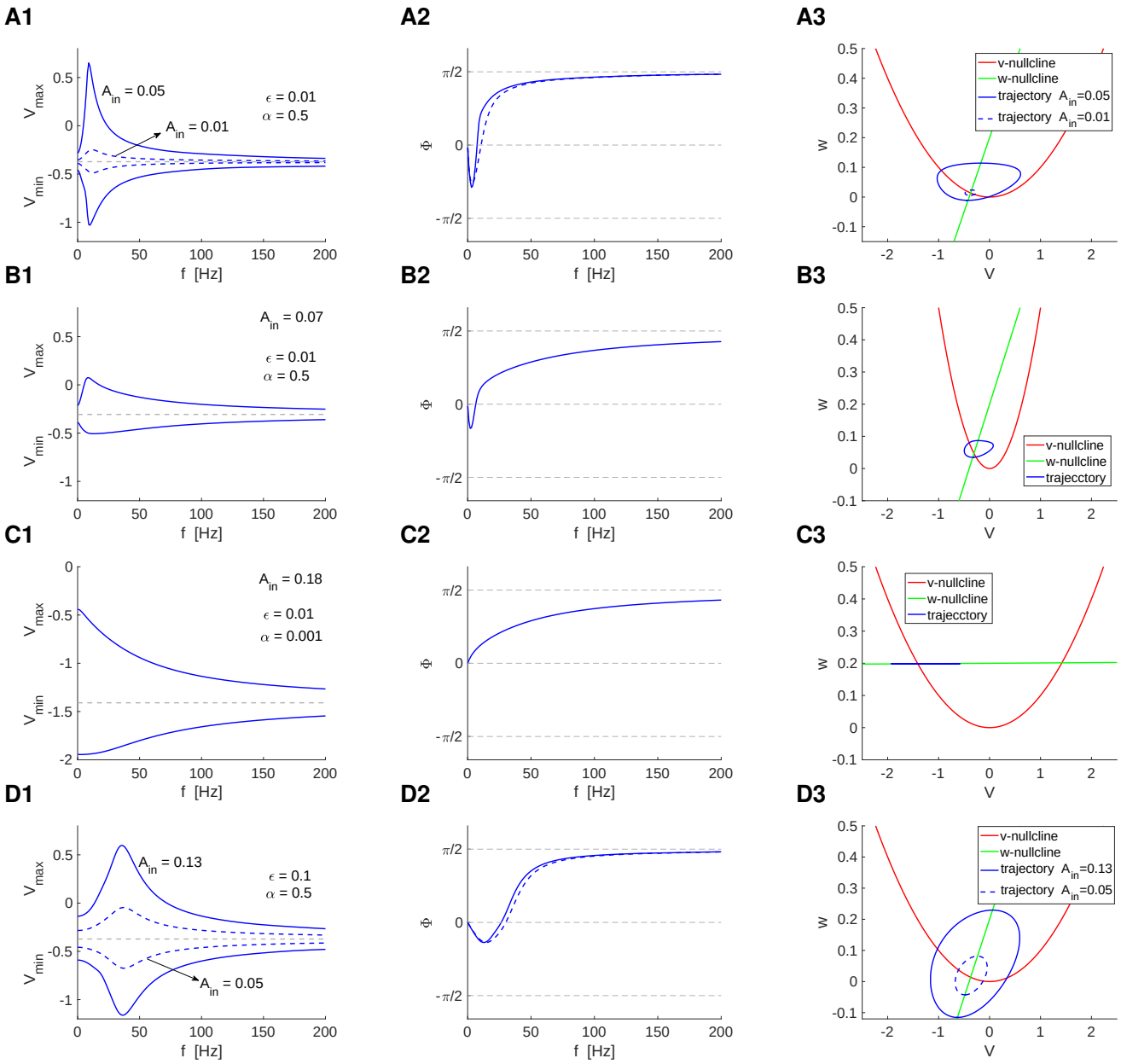

Figure 14: **Response of the individual quadratic 2D cells to oscillatory inputs: Representative nonlinear BPFs and LPFs.** We used the quadratic model for an individual cell (3)-(4) ($k = 1$, $g_c = 0$). **Left column.** Peak (V_{max}) and trough (V_{min}) envelope profiles **Middle column.** Phase (Φ) profiles **Right column.** Phase-space diagrams for the peak / resonant frequency. The v- and w-nullclines are given by $w = a\,v^2$ and $w = \alpha\,v - \lambda$, respectively. The response trajectory is a projection of the three-dimensional space onto the v-w plane. **A.** $\alpha = 0.5$, $\epsilon = 0.01$, $a = 0.1$, $A_{in} = 0.05$ (solid) and $A_{in} = 0.01$ (dashed). The dashed curve is presented for comparison between the responses of the nonlinear (solid) and quasi-linear (dashed) systems for low enough values of A_{in}. The solid curve corresponds to approximately the highest value of A_{in} for which the response remains within the subthreshold regime for all input frequencies.. **B.** $\alpha = 0.5$, $\epsilon = 0.01$ $a = 0.5$ and $A_{in} = 0.01$. The parabolic nonlinearity is more pronounced and the response nonlinear. **C.** $\alpha = 0.001$, $\epsilon = 0.01$, $a = 0.1$ and $A_{in} = 0.18$. The system is quasi-1D as the result of the disruption of the activation of the negative feedback term. For lower values of A_{in} (e.g., $A_{in} = 0.05$ as the one in panel A), the LPF is quasi-symmetric reflecting the response of a quasi-linear system (not shown). **D.** $\alpha = 0.5$, $\epsilon = 0.1$, $a = 0.1$, $A_{in} = 0.13$ (solid) and $A_{in} = 0.05$ (dashed). The BPF is quasi-symmetric reflecting the underlying quasi-linear dynamics. The dashed curve is presented for comparison with the BPF in panel A. We use the following additional parameter values: $a = 0.1$, $\lambda = -0.2$.

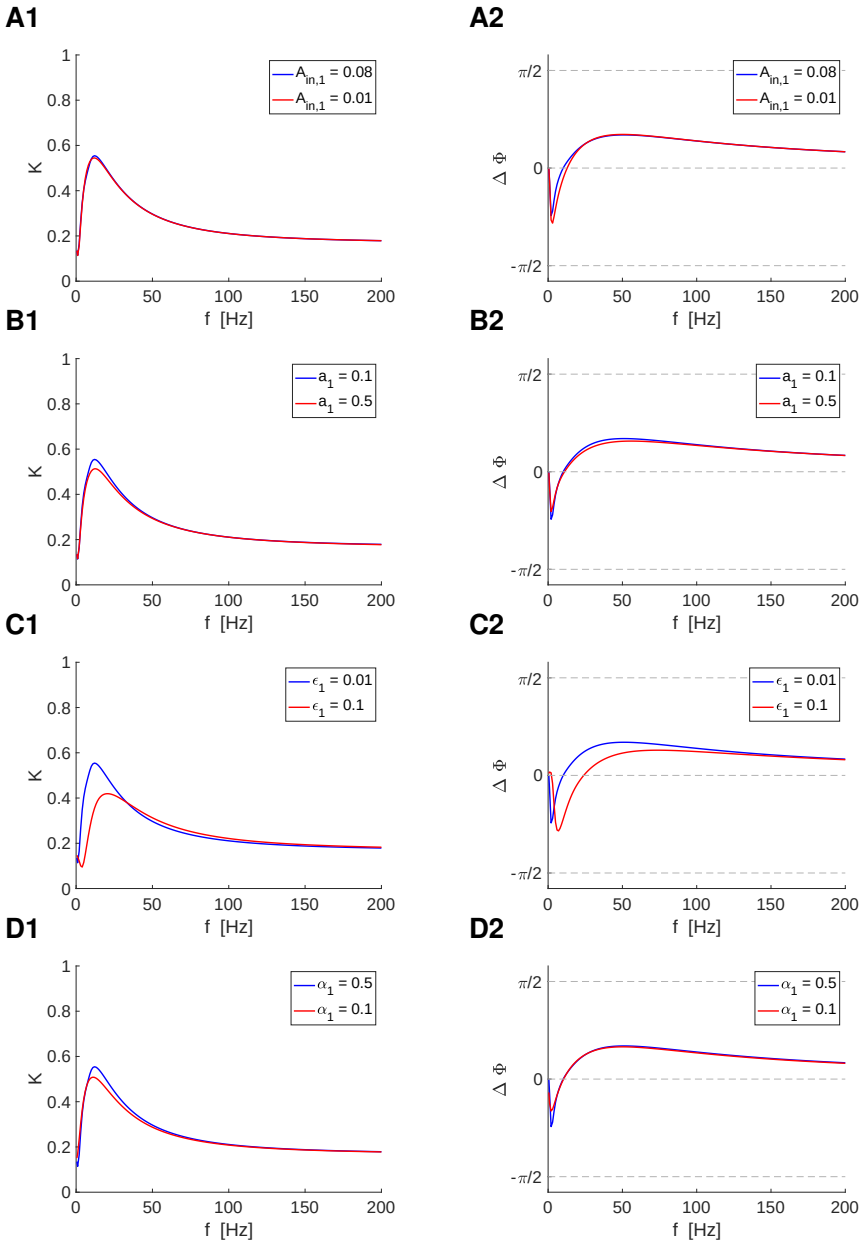

Figure 15: **Electrically coupled quadratic 2D model: Effects of the pre-J cell's properties on the response profiles.** We used the quadratic model (3)-(4) for the electrically coupled pre- and post-J cells with quadratic nonlinearities mediated by gap junctions (cell 1 is the pre-J cell; $A_{in,2} = 0$) . The parameter values for the two cells are identical, except for the ones indicated in the legends. **Left column.** K profiles **Right column.** $\Delta\Phi$ profiles **A.** $a_1 = a_2 = 0.1$, $\alpha_1 = \alpha_2 = 0.5$, $\epsilon_1 = \epsilon_2 = 0.01$. **B.** $a_2 = 0.1$, $\alpha_1 = \alpha_2 = 0.5$, $\epsilon_1 = \epsilon_2 = 0.01$, $A_{in,1} = 0.08$. **C.** $a_1 = a_2 = 0.1$, $\alpha_1 = \alpha_2 = 0.5$, $\epsilon_2 = 0.01$, $A_{in,1} = 0.08$. **D.** $a_1 = a_2 = 0.1$, $\alpha_2 = 0.5$, $\epsilon_1 = \epsilon_2 = 0.01$, $A_{in,1} = 0.08$. We used the following additional parameter values: $\lambda_1 = \lambda_2 = -0.2$, $g_c = 0.1$ and $A_{in,2} = 0$.

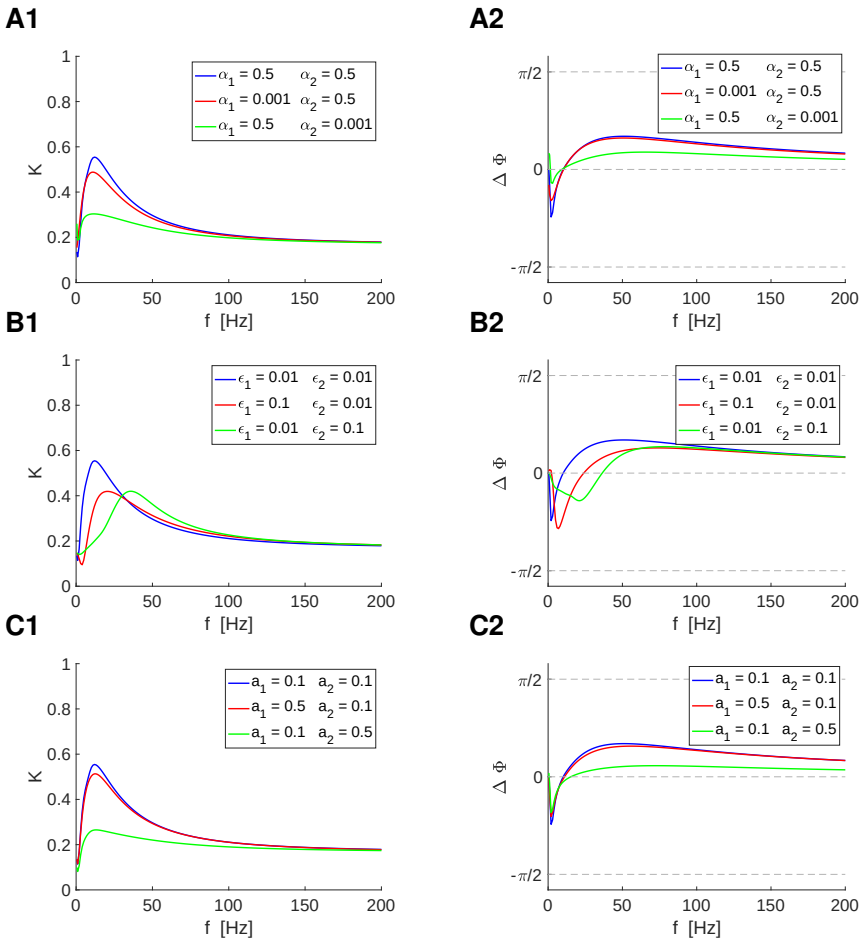

Figure 16: **Electrically coupled quadratic 2D model: Effects of the pre-J and post-J cells' properties on the response profiles.** We used the quadratic model (3)-(4) for the electrically coupled pre- and post-J cells with quadratic nonlinearities mediated by gap junctions (cell 1 is the pre-J cell; $A_{in,2} = 0$) . The parameter values for the two cells are identical, except for the ones indicated in the legends. **Left column.** K profiles **Right column.** $\Delta\Phi$ profiles **A.** Effect of the α (negative feedback / resonant current strength). We used $a_1 = a_2 = 0.1$, $\epsilon_1 = \epsilon_2 = 0.01$. **A-blue.** The pre-J and post-J cells are identical BPFs (Fig. 14-A). **A-red.** The pre-J cell is a LPF (Fig. 14-C) and the post-J cell is a BPF (Fig. 14-A). **A-green.** The pre-J cell is a BPF (Fig. 14-A) and the post-J cell is a LPF (Fig. 14-C). **B.** Effect of ϵ (negative feedback / resonant current time constant). We used $a_1 = a_2 = 0.1$, $\alpha_1 = \alpha_2 = 0.5$. The pre-J and post-J cells are both BPFs (Figs. 14-A and -D). **B-blue.** The pre-J and post-J cells are identical BPFs (Fig. 14-A). **B-red.** The resonant frequency of the pre-J cell (Fig. 14-D) is higher than for the post-J cell (Fig. 14-A). **B-green.** The resonant frequency of the pre-J cell (Fig. 14-A) is lower than for the post-J cell (Fig. 14-D). **C.** Effect of a (curvature of the parabolic nonlinearity). We used $\alpha_1 = \alpha_2 = 0.5$, $\epsilon_1 = \epsilon_2 = 0.01$. **C-blue.** The V-nullcline for the pre-J and post-J cells have identical curvatures (Fig. 14-A). **C-red.** The curvature of the V-nullcline for the pre-J cell is larger (Fig. 14-B) than for the post-J cell (Fig. 14-A). **C-green.** The curvature of the V-nullcline for the pre-J cell is smaller (Fig. 14-A) than for the post-J cell (Fig. 14-B). We used the following additional parameter values:, $\lambda_1 = \lambda_2 = -0.2$, $g_c = 0.1$, $A_{in,1} = 0.06$ and $A_{in,2} = 0$.

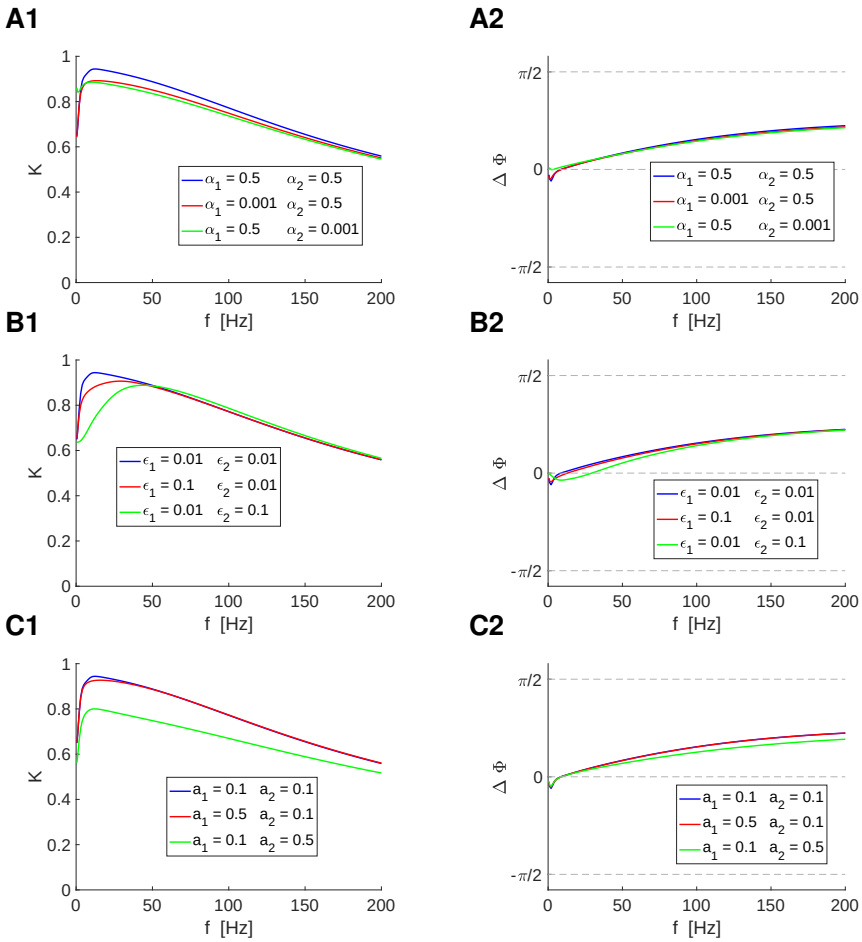

Figure 17: **Electrically coupled quadratic 2D model: Effects of the pre-J and post-J cells' properties on the response profiles.** We used the quadratic model (3)-(4) for the electrically coupled pre- and post-J cells with quadratic nonlinearities mediated by gap junctions (cell 1 is the pre-J cell; $A_{in,2} = 0$) . The parameter values for the two cells are identical, except for the ones indicated in the legends. **Left column.** K profiles **Right column.** $\Delta\Phi$ profiles **A.** Effect of the α (negative feedback / resonant current strength). We used $a_1 = a_2 = 0.1$, $\epsilon_1 = \epsilon_2 = 0.01$. **A-blue.** The pre-J and post-J cells are identical BPFs (Fig. 14-A). **A-red.** The pre-J cell is a LPF (Fig. 14-C) and the post-J cell is a BPF (Fig. 14-A). **A-green.** The pre-J cell is a BPF (Fig. 14-A) and the post-J cell is a LPF (Fig. 14-C). **B.** Effect of ϵ (negative feedback / resonant current time constant). We used $a_1 = a_2 = 0.1$, $\alpha_1 = \alpha_2 = 0.5$. The pre-J and post-J cells are both BPFs (Figs. 14-A and -D). **B-blue.** The pre-J and post-J cells are identical BPFs (Fig. 14-A). **B-red.** The resonant frequency of the pre-J cell (Fig. 14-D) is higher than for the post-J cell (Fig. 14-A). **B-green.** The resonant frequency of the pre-J cell (Fig. 14-A) is lower than for the post-J cell (Fig. 14-D). **C.** Effect of a (curvature of the parabolic nonlinearity). We used $\alpha_1 = \alpha_2 = 0.5$, $\epsilon_1 = \epsilon_2 = 0.01$. **C-blue.** The V-nullcline for the pre-J and post-J cells have identical curvatures (Fig. 14-A). **C-red.** The curvature of the V-nullcline for the pre-J cell is larger (Fig. 14-B) than for the post-J cell (Fig. 14-A). **C-green.** The curvature of the V-nullcline for the pre-J cell is smaller (Fig. 14-A) than for the post-J cell (Fig. 14-B). We used the following additional parameter values:, $\lambda_1 = \lambda_2 = -0.2$, $g_c = 1$, $A_{in,1} = 0.08$ and $A_{in,2} = 0$.

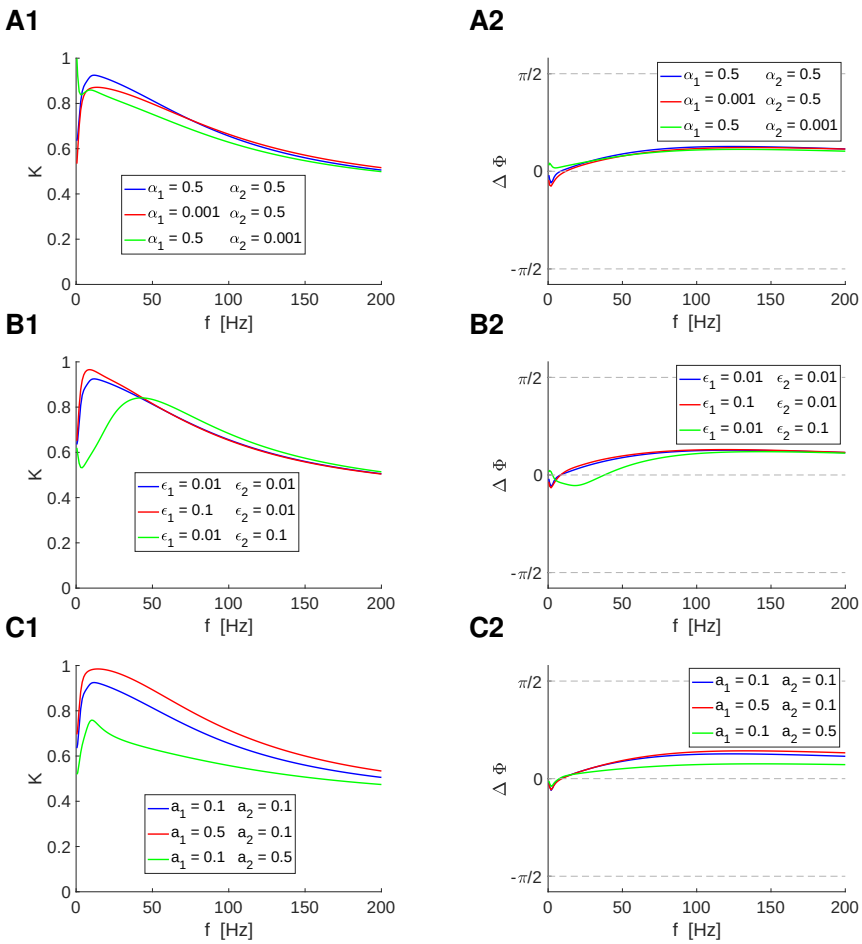

Figure 18: **Two-compartment model with quadratic 2D dynamics : Effects of the pre-J and post-J compartments' properties on the response profiles.** We used the quadratic model (3)-(4) for the electrically coupled pre- and post-J compartments with quadratic nonlinearities where the coupling parameter $g_{c,k}$ was substituted by g_c/σ_k with $\sigma_1 = 0.8$ and $\sigma_2 = 0.2$ (compartment 1 is the pre-J compartment; $A_{in,2} = 0$) . The parameter values for the two compartments are identical, except for the ones indicated in the legends. **Left column.** K profiles **Right column.** $\Delta\Phi$ profiles **A.** Effect of the α (negative feedback / resonant current strength). We used $a_1 = a_2 = 0.1$, $\epsilon_1 = \epsilon_2 = 0.01$. **A-blue.** The pre-J and post-J compartments are identical BPFs (Fig. 14-A). **A-red.** The pre-J compartment is a LPF (Fig. 14-C) and the post-J compartment is a BPF (Fig. 14-A). **A-green.** The pre-J compartment is a BPF (Fig. 14-A) and the post-J compartment is a LPF (Fig. 14-C). **B.** Effect of ϵ (negative feedback / resonant current time constant). We used $a_1 = a_2 = 0.1$, $\alpha_1 = \alpha_2 = 0.5$. The pre-J and post-J compartments are both BPFs (Figs. 14-A and -D). **B-blue.** The pre-J and post-J compartments are identical BPFs (Fig. 14-A). **B-red.** The resonant frequency of the pre-J compartment (Fig. 14-D) is higher than for the post-J compartment (Fig. 14-A). **B-green.** The resonant frequency of the pre-J compartment (Fig. 14-A) is lower than for the post-J compartment (Fig. 14-D). **C.** Effect of a (curvature of the parabolic nonlinearity). We used $\alpha_1 = \alpha_2 = 0.5$, $\epsilon_1 = \epsilon_2 = 0.01$. **C-blue.** The V-nullcline for the pre-J and post-J cells have identical curvatures (Fig. 14-A). **C-red.** The curvature of the V-nullcline for the pre-J cell is larger (Fig. 14-B) than for the post-J cell (Fig. 14-A). **C-green.** The curvature of the V-nullcline for the pre-J cell is smaller (Fig. 14-A) than for the post-J cell (Fig. 14-B). We used the following additional parameter values:, $\lambda_1 = \lambda_2 = -0.2$, $g_c = 0.05$, $A_{in,1} = 0.06$ and $A_{in,2} = 0$.

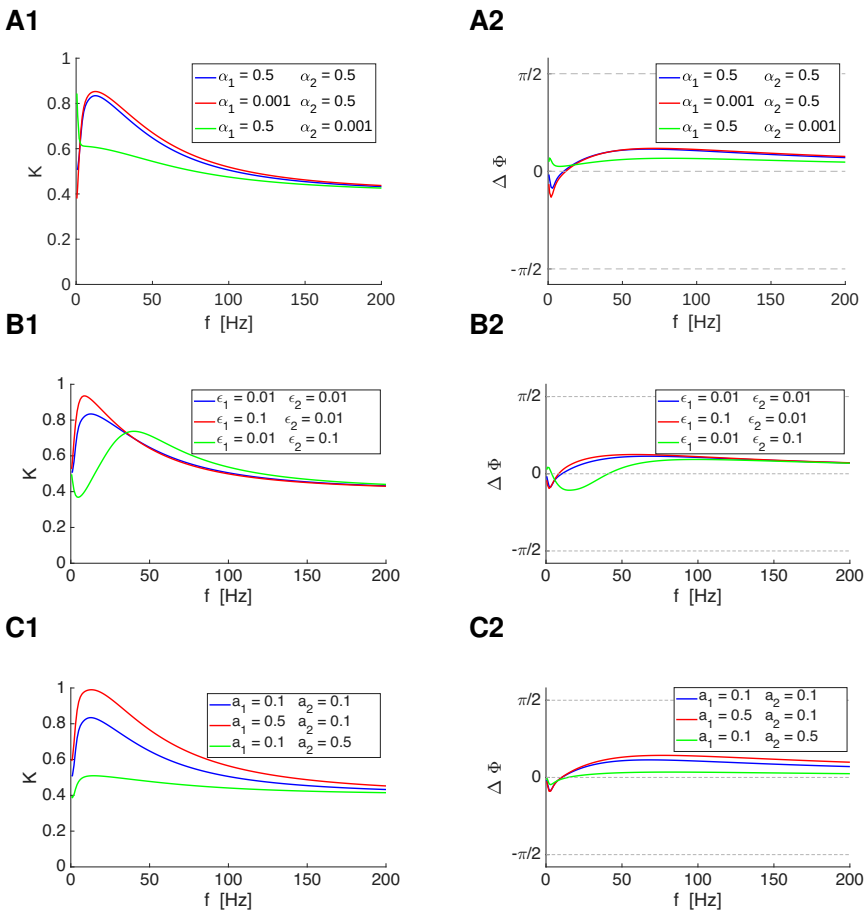

Figure 19: **Two-compartment model with quadratic 2D dynamics : Effects of the pre-J and post-J compartments' properties on the response profiles.** We used the quadratic model (3)-(4) for the electrically coupled pre- and post-J compartments with quadratic nonlinearities where the coupling parameter $g_{c,k}$ was substituted by g_c/σ_k with $\sigma_1 = 0.2$ and $\sigma_2 = 0.8$ (compartment 1 is the pre-J compartment; $A_{in,2} = 0$) . The parameter values for the two compartments are identical, except for the ones indicated in the legends. **Left column.** K profiles **Right column.** $\Delta\Phi$ profiles **A.** Effect of the α (negative feedback / resonant current strength). We used $a_1 = a_2 = 0.1$, $\epsilon_1 = \epsilon_2 = 0.01$. **A-blue.** The pre-J and post-J compartments are identical BPFs (Fig. 14-A). **A-red.** The pre-J compartment is a LPF (Fig. 14-C) and the post-J compartment is a BPF (Fig. 14-A). **A-green.** The pre-J compartment is a BPF (Fig. 14-A) and the post-J compartment is a LPF (Fig. 14-C). **B.** Effect of ϵ (negative feedback / resonant current time constant). We used $a_1 = a_2 = 0.1$, $\alpha_1 = \alpha_2 = 0.5$. The pre-J and post-J compartments are both BPFs (Figs. 14-A and -D). **B-blue.** The pre-J and post-J compartments are identical BPFs (Fig. 14-A). **B-red.** The resonant frequency of the pre-J compartment (Fig. 14-D) is higher than for the post-J compartment (Fig. 14-A). **B-green.** The resonant frequency of the pre-J compartment (Fig. 14-A) is lower than for the post-J compartment (Fig. 14-D). **C.** Effect of a (curvature of the parabolic nonlinearity). We used $\alpha_1 = \alpha_2 = 0.5$, $\epsilon_1 = \epsilon_2 = 0.01$. **C-blue.** The V-nullcline for the pre-J and post-J cells have identical curvatures (Fig. 14-A). **C-red.** The curvature of the V-nullcline for the pre-J cell is larger (Fig. 14-B) than for the post-J cell (Fig. 14-A). **C-green.** The curvature of the V-nullcline for the pre-J cell is smaller (Fig. 14-A) than for the post-J cell (Fig. 14-B). We used the following additional parameter values:, $\lambda_1 = \lambda_2 = -0.2$, $g_c = 0.05$, $A_{in,1} = 0.06$ and $A_{in,2} = 0$.

realistic ionic currents to understand, to the linear level of approximation, how the presence and different types of amplifying and resonant ionic processes shape the CC profiles. Motivated by experimental results and previous theoretical studies, we used the I_{Nap} + I_h and I_{Nap} + I_{Ks} models [21, 55, 66, 67] that exhibit both cellular resonance and phasonance [63–65]. These two models are biophysically different, because they involve different resonant currents, but dynamically similar since their phase-plane diagrams are almost a mirror image of each other [93].

Each parameter in the linearized models is a function of a set of parameters in the (original) biophysical model. The response for each set of parameter values in the linearized model is, obviously, linear. However, the notion of linearity has different meanings and implications depending on the context. On the one hand, linear models are reduced models. In this sense, the response of a linearized models are approximation to the original corresponding biophysical model. On the other hand, linear models have certain properties that become apparent only upon changes in the model parameters (e.g., the amplitudes of the response is proportional to the input for all frequencies). Here, we were interested in processes such as amplification and the modulation of resonance, which materialize when one changes the amplifying and resonant ionic conductances.

In the “linear study" discussed above, we investigated how the $K(f)$ and $\Delta\Phi(f)$ profiles change as we changed the linear parameters independently of any other consideration. In this “linearized" part of the study, in contrast, we changed the biophysical parameters (e.g., ionic conductances) and recalculated the linear parameters for each one of the choices of biophysical parameter values. This process captured the nonlinear effects “to the linear level of approximation" and the differences between the way the two models (I_{Nap} + I_h and I_{Nap} + I_{Ks}) shape the $K(f)$ and $\Delta(f)$ profiles and determine their preferred frequencies. This is summarized in Tables 2 and 3. One salient difference between the results for the two models is that, in the presence of high enough levels of I_{Nap}, increasing levels of I_h amplify the $K(f)$ profile, while increasing values of I_{Ks} attenuate the $K(f)$ profile, while in the presence of low enough levels of I_{Nap}, increasing values of both I_h and I_{Ks} attenuate the $K(f)$ profile. A similar effect has been observed for the impedance profile in single cells [21]. The effects of asymmetry in the connectivity (e.g., for two-compartment models) was inferred from these results by a set of algebraic operations.

While the linearized models capture certain nonlinear properties of the behavior of the biophysical models, the linearized models' CC profiles remain independent of the properties of the pre-J cells and depend only on the properties of the post-J cell and the connectivity. A set of analytical results using regular perturbation theory for electrically coupled weakly nonlinear cells showed that the both the pre-J and post-J cells contribute to shaping the CC profiles. However, while weakly nonlinear models capture the dynamics of the I_{Nap} + I_h and I_{Nap} + I_{Ks} models for at most low levels of I_{Nap}, they fail to do so for the more realistic scenarios with higher levels of I_{Nap} causing the development of voltage nonlinearities of parabolic type in a vicinity of the resting potential. To understand how these nonlinearities affect the properties of the CC profiles, we extended our investigation to networks of electrically coupled quadratized cells, which have a parabolic voltage nonlinearities and linear dynamics for the recovery variable. Similarly to linearization, quadratization of biophysical models produces a quadratic model whose parameters are functions of the biophysical parameters of the original, parabolic-like model. In this case, the I_{Nap} + I_h and I_{Nap} + I_{Ks} models.

We computationally analyzed the biophysical mechanisms of generation of the $K(f)$ and $\Delta(f)$ in the quadratic models and demonstrated computationally that they depend on the properties of both the pre-J and post-J cells and the network connectivity. In some cases, the contribution of the pre-J cells is relatively small, but in others is significant, which is missed by using linearized models. Finally, we showed that these results persists for two-compartment models with the additional dependence on the pre-J and post-J geometric properties and for inputs effectively arriving in different compartments.

Our results advance our knowledge on the response of electrically coupled networks to oscillatory inputs and the frequency-dependent properties of the CC profiles. These results highlight the emergence of preferred CC frequencies at which $K(f)$ peaks (the coupling strength is maximal at the K-resonant frequency $f_{res,K}$) and for which the pre-J and post-J cell peak synchronously in phase ($\Delta\Phi = 0$ at the $\Delta\Phi$-phasonant frequency $f_{phas,K}$). These results have direct implications for spike transmission [32, 52] in electrically coupled networks in response to oscillatory inputs, for the propagation of signals along the somato-dendritic axis in the presence of resonance and phasonance along the dendritic tree [54, 55, 94], for the rhythmic coding of hippocampal pyramidal cells [95] and, more generally, for dendritic

computation [96–101].

The ideas and results developed in this paper can be extended to electrically coupled networks with a larger number of nodes and possibly multiple inputs, to spatially extended multicompartment neuronal models possibly receiving inputs at different locations (e.g., distal and proximal inhibition by oriens lacunosum-moleculare and fast spiking interneurons, respectively, in hippocampal pyramidal cells), to models having combined amplifying and resonant processes such as $I_{Ca,T}$ activation and inactivation, respectively, and to I_{Nap} + I_h and I_{Nap} + I_{Ks} models having nonlinearities of cubic type, instead of parabolic type, in the subthreshold voltage regime [93]. More research is needed to address these issues. Research is also needed to test experimentally the predictions of our study.

Acknowledgments

AB and UC acknowledge support from the Universidad Nacional del Sur grant PGI 24/L131 and CONICET, Argentina. HGR acknowledges support from the National Science Foundation grants DMS-1608077 and IOS-2002863. HGR is a Corresponding Researcher in CONICET, Argentina and a Graduate Faculty Member in the Graduate Program in Neuroscience (GPN) in the Center for Molecular and Behavioral Neuroscience (CMBN) at Rutgers University.

References

[1] B. Hutcheon and Y. Yarom. Resonance, oscillations and the intrinsic frequency preferences in neurons. *Trends Neurosci.*, 23:216–222, 2000.

[2] M. Tsodyks, A. Uziel, and H. Markram. Synchrony generation in recurrent networks with frequency-dependent synapses. *J. Neurosci.*, 20:1–5, 2000.

[3] E. M. Izhikevich, N. S. Desai, E. C. Walcott, and F. C. Hoppensteadt. Bursts as a unit of neural information: Selective communication via resonance. *Trends Neurosci.*, 26:161–167, 2003.

[4] E. Stark, A. Levi, and H. G. Rotstein. Neuronal resonance can be generated independently at distinct levels of organization. *PLoS Comp. Biol.*, 18:e1010364, 2022.

[5] J. Laudansky, B. Torben-Nielsen, I. Segev, and S. Shama. Spatially distributed dendritic resonance selectively filters synaptic input. *PLoS Comp. Biol.*, 8:e1003775, 2014.

[6] T. E. Akam and D. M. Kullmann. Efficient communication through coherence requires oscillations structured to minimize interference between signals. *PLoS Comp. Biol.*, 8:e1002760, 2012.

[7] W. Maass. Searching for principles of brain computation. *Curr. Opin. Neurobiol.*, 11:81–92, 2016.

[8] M. Beiran and S. Ostojic. Contrasting the effects of adaptation and synaptic filtering on the timescales of dynamics in recurrent networks. *PLoS Comp. Biol.*, 15:e1006893, 2019.

[9] E. Fortune and G. Rose. Short-term plasticity as a temporal filter. *Trends Neurosci.*, 24:381–385, 2001.

[10] V. A. Klyachko and C. F. Stevens. Excitatory and feed-forward inhibitory hippocampal synapses work synergistically as an adaptive filter of natural spike trains. *PLoS Comp. Biol.*, 4:e207, 2006.

[11] A. Thomson. Presynaptic frequency- and pattern-dependent filtering. *J. Comp. Neurosci.*, 15:159–202, 2003.

[12] T. E. Akam and D. M. Kullmann. Oscillations and filtering networks support flexible routing of information. *Neuron*, 67:308–320, 2010.

[13] S. Blankenburg, W. Wu, B. Lindner, and S. Schreiber. Information filtering in resonant neurons. *J. Comp. Neurosci.*, 39:349–370, 2015.

[14] R. Rosenbaum, J. Rubin, and B. Doiron. Short term synaptic depression imposes a frequency dependent filter on synaptic information transfer. *PLoS Comp. Biol.*, 8:e1002557, 2012.

[15] N. Brunel, F. S. Chance, N. Fourcaud, and L. F. Abbott. Effects of synaptic noise and filtering on the frequency response of spiking neurons. *Phys. Rev. Lett.*, 86:2186–2189, 2001.

[16] D. Buonomano and W. Maass. State-dependent computations: spatiotemporal processing in cortical networks. *Nat. Rev. Neurosci.*, 10:113–125, 2009.

[17] J. E. Lisman. Bursts as a unit of neural information: making unreliable synapses reliable. *Trends Neurosci.*, 20:38–43, 1997.

[18] J. S. Sherfey, S. Ardid, J. Hass, M. E. Hasselmo, and N. J. Kopell. Flexible resonance in prefrontal networks with strong feedback inhibition. *PLoS Comp. Biol.*, 14:e1006357, 2018.

[19] E. Stark, R. Eichler, L. Roux, S. Fujisawa, H. G. Rotstein, and G. Buzsáki. Inhibition-induced theta resonance in cortical circuits. *Neuron*, 80:1263–1276, 2013.

[20] M. J. E. Richardson, N. Brunel, and V. Hakim. From subthreshold to firing-rate resonance. *J. Neurophysiol.*, 89:2538–2554, 2003.

[21] H. G. Rotstein and F. Nadim. Frequency preference in two-dimensional neural models: a linear analysis of the interaction between resonant and amplifying currents. *J. Comp. Neurosci.*, 37:9–28, 2014.

[22] R. Dermietzel and D. C. Spray. Gap junctions in the brain: where, what type, how many and why? *Trends Neurosci.*, 16:186–192, 1993.

[23] K. Shimizu and M. Stopfer. Gap junctions. *Current Biology*, 23:R1026–R1031, 2013.

[24] E. García-Perez, M. Vargas-Caballero, N. Velazquez-Ulloa, A. Minzoni, and F. F. De-Miguel. Synaptic integration in electrically coupled neurons. *Biophysical J.*, 86:646–655, 2004.

[25] A. E. Pereda, S. Curti, G. Hoge, R. Cachope, C. E. Flores, and J. E. Rash. Gap junction-mediated electrical transmission: regulatory mechannisms and plasticity. *Biochim Biobhys Acta*, 1828:134–146, 2013.

[26] M. V. L. Bennett. Electrical transmission: a functional analysis and comparison to chemical transmission. *In: Handbook of Physiology. The Nervous System. Cellular Biology of Neurons. Bethesda, MD: Am. Physiol. Soc., 1977, sect. 1, vol. I, pt.*, pages 357–416, 1977.

[27] B. W. Connor and M. A. Long. Electrical synapses in the mammalian brain. *Annu. Rev. Neurosci.*, 27:393–418, 2004.

[28] J. R. Gibson, M. Beierlein, and B. W. Connors. Functional properties of electrical synapses between inhibitory interneurons of neocortical layer 4. *J. Neurophysiol.*, 93:467–480, 2005.

[29] C. E. Landisman, M. A. Long, M. Beierlein, M. R. Deans, D. L. Paul, and B. W. Connors. Electrical synapses in the thalamic reticular nucleus. *J. Neurosci.*, 21:2974–2982, 2001.

[30] M. S. Nielsen, L. N. Axelsen, P. L. Sorgen, V. Verma, M. Delmar, and N. H. Holstein-Rathlou. Gap junctions. *Physiol Rev.*, 2:1981–2035, 2012.

[31] J. (Ed.) Jing. *Network Functions and Plasticity: Perspectives from Studying Neuronal Electrical Coupling in Microcircuits*. Academic Press: Cambridge, MA, USA, 2017.

[32] S. Curti, G. Hoge, J. I. Nagy, and A. E. Pereda. Synergy between electrical coupling and membrane properties promotes strong synchronization of neurons of the mesencephalic trigeminal nucleus. *J. Neurosci.*, 32:4341–4359, 2012.

[33] P. Alcamí and A. E. Pereda. Beyond plasticity: The dynamic impact of electrical synapses on neural circuits. *Nat. Rev. Neurosci.*, 20:253–271, 2019.

[34] M. V. L. Bennett and R. S. Zukin. Electrical coupling and neuronal synchronization in the mammalian brain. *Neuron*, 41:495–511, 2004.

[35] G. J. Hoge, K. G. V. Davidson, T. Yasumura, P. E. Castillo, J. E. Rash, and A. E. Pereda. The extent and strength of electrical coupling between inferior olivary neurons is heterogeneous. *J. Neurophysiol.*, 105:1089–1101, 2011.

[36] M. V. L. Bennett. Physiology of electronic junctions. *Ann. N. Y. Acad. Sci.*, 137:509–539, 1966.

[37] G. Weizel and S. Schuster. A direct comparison of different measures for the strength of electrical synapses. *Frontiers in Cellular Neuroscience*, 13:43, 2019.

[38] N. T. Carnevale and D. Johnston. Electrophysiological characterization of remote chemical synapses. *J. Neurophysiol.*, 47:606–621, 1982.

[39] A. Watanabe and H. Grundfest. Impulse propagation at the septal and commissural junctions of crayfish lateral giant axons. *J. Gen. Physiol.*, 45:267–308, 1961.

[40] M. Galarreta and S. Hestrin. A network of fast-spiking cells in the neocortex connected by electrical synapses. *Nature*, 402:72–75, 1999.

[41] M. Galarreta and S. Hestrin. Spike transmission and synchrony detection in networks of GABAergic interneurons. *Science*, 292:2295–2299, 2001.

[42] G. Pernelle, W. Nicola, and C. Clopath. Gap junction plasticity as a mechanism to regulate network-wide oscillations. *PLoS Comp. Biol.*, 14:e1006025, 2018.

[43] S. Curti and J. O'brien. Characteristics and plasticity of electrical synaptic transmission. *BMC Molecular and Cell Biology*, 17:13, 2016.

[44] S. Curti, F. Davoine, and A. Dapino. Function and plasticity of electrical synapses in the mammalian brain: role of non-junctional mechanisms. *Biology*, 11:81, 2022.

[45] M. E. Sira and M. W. Bennett. Synaptic control of electrotonic coupling between neurons. *Brain Res.*, 37:294–300, 1972.

[46] A. Watanabe. The interaction of electrical activity among neurons of lobster cardiac ganglion. *Jpn J Physiol.*, 8:305–318, 1958.

[47] B. W. Connors, T. A. Zolnik, and S. C. Lee. functions of electrical junctions. *Neuron*, 67:354–356, 2010.

[48] M. Galarreta and S. Hestrin. Frequency-dependent synaptic depression and the balance of excitation and inhibition in the neocortex. *Nature Neurosci.*, 1:587–594, 1998.

[49] G. P. Dugué, N. Brunel, V. Hakim, E. Schwartz, M. Chat, M. Lévesque, R. Courtemanche, C. Léna, and S. Dieudonné. Electrical coupling mediates tunable low-frequency oscillations and resonance in the cerebellar Golgi cell network. *Neuron*, 61:126–139, 2009.

[50] M. L. Veruki and E. Hartveit. AII (Rod) amacrine cells form a network of electrically coupled interneurons in the mammalian retina. *Neuron*, 33:935–946, 2002.

[51] S. Curti and A. E. Pereda. Voltage-dependent enhancement of electrical coupling by a subthreshold sodium current. *J. Neurosci.*, 24:3999–4010, 2004.

[52] F. Davoine, S. Curti, and P. Monzon. Spike transmission between electrically coupled sensory neurons is improved by filter properties. *In Proceedings of the 2020 IEEE International Symposium on Circuits and Systems (ISCAS), Institute of Electrical and Electronics Engineers (IEEE)*, pages 1–5, 2020.

[53] X. Li, O. Itani, D. Bucher, H. G. Rotstein, and F. Nadim. Distinct mechanisms underlie electrical coupling resonance and its interaction with membrane potential resonance. *Front. Syst. Biol.*, 3:1122433., 2023.

[54] H. Hu, K. Vervaeke, and J. F. Storm. Two forms of electrical resonance at theta frequencies generated by M-current, h-current and persistent Na^+ current in rat hippocampal pyramidal cells. *J. Physiol.*, 545.3:783–805, 2002.

[55] H. Hu, K. Vervaeke, L. J. Graham, and J. F. Storm. Complementary theta resonance filtering by two spatially segregated mechanisms in CA1 hippocampal pyramidal neurons. *J. Neurosci.*, 29:14472–14483, 2009.

[56] R. Narayanan and D. Johnston. The h channel mediates location dependence and plasticity of intrinsic phase response in rat hippocampal neurons. *J. Neurosci.*, 28:5846–5850, 2008.

[57] S Ostojic, G. Szapiro, E. Schwartz, B. Barbour, N. Brunel, and V. Hakim. Neuronal morphology generates high-frequency firing resonance. *J. Neurosci.*, 35:7056–7068, 2015.

[58] E. Zhuchkova, M. W. H. Remme, and S. Schreiber. Subthreshold resonance and membrane potential oscillations in a neuron with nonuniform active dendrite properties. *In: Cuntz H, Remme MWH, Torben-Nielsen B, editors, The Computing Dendrite, New York, NY: Springer New York*, 2014.

[59] E. Zhuchkova, M. W. H. Remme, and S. Schreiber. Somatic versus dendritic resonance: differential filtering of inputs through non-uniform distributions of active conductances. *PLoS ONE*, 8:e78908, 2013.

[60] R. S. Kasevich and D LaBerge. Theory of electric resonance in the neocortical apical dendrite. *PLoS ONE*, 6:e23412, 2011.

[61] O. Oz, A. Matityahu, A. Mizrahi-Kliger, A. Kaplan, N. Berkowitz, L. Tiroshi, H. Bergman, and J. Goldberg. Non-uniform distribution of dendritic nonlinearities differentially engages thalamostriatal and corticostriatal inputs onto cholinergic interneurons. *eLife*, 11:e76039, 2022.

[62] J. Ladenbauer, M. Augustin, L. Shiau, and K. Obermayer. Impact of adaptation currents on synchronization of coupled exponential integrate-and-fire neurons. *PLoS Comp. Biol.*, 8:e1002478, 2012.

[63] F. G. Pike, R. S. Goddard, J. M. Suckling, P. Ganter, N. Kasthuri, and O. Paulsen. Distinct frequency preferences of different types of rat hippocampal neurons in response to oscillatory input currents. *J. Physiol.*, 529:205–213, 2000.

[64] L. S. Leung and H. W. Yu. Theta-frequency resonance in hippocampal CA1 neurons *in vitro* demonstrated by sinusoidal current injection. *J. Neurophysiol.*, 79:1592–1596, 1998.

[65] R. Zemankovics, S. Káli, O. Paulsen, T. F. Freund, and N. Hájos. Differences in subthreshold resonance of hippocampal pyramidal cells and interneurons: The role of h-current and passive membrane characteristics. *J. Physiol.*, 588:2109–2132, 2010.

[66] H. G. Rotstein. The shaping of intrinsic membrane potential oscillations: positive/negative feedback, ionic resonance/amplification, nonlinearities and time scales. *J. Comp. Neurosci.*, 42:133–166, 2017.

[67] H. G. Rotstein. Spiking resonances in models with the same slow resonant and fast amplifying currents but different subthreshold dynamic properties. *J. Comp. Neurosci.*, 43:243–271, 2017.

[68] P. Dayan and L. F. Abbott. *Theoretical Neuroscience*. The MIT Press, Cambridge, Massachusetts, 2001.

[69] G. B. Ermentrout and D. Terman. *Mathematical Foundations of Neuroscience*. Springer, 2010.

[70] A. G. R. Turnquist and H. G. Rotstein. Quadratization: From conductance-based models to caricature models with parabolic nonlinearities. *In: Jaeger D., Jung R. (Ed.) Encyclop edia of Computational Neuroscience. Springer-Verlag, New York*, 2018.

[71] H. G. Rotstein. Subthreshold amplitude and phase resonance in models of quadratic type: nonlinear effects generated by the interplay of resonant and amplifying currents. *J. Comp. Neurosci.*, 38:325–354, 2015.

[72] U. Chialva, V. Gonzalez Bosca, and H. G. Rotstein. Low-dimensional models of single neurons: A review. *Biol. Cybern.*, 117:163 – 183, 2023.

[73] A. L. Hodgkin and A. F. Huxley. A quantitative description of membrane current and its application to conductance and excitation in nerve. *J. Physiol.*, 117:500–544, 1952.

[74] E. Izhikevich. *Dynamical Systems in Neuroscience: The geometry of excitability and bursting*. MIT Press (Cambridge, Massachusetts), 2006.

[75] H. G. Rotstein, T. Oppermann, J. A. White, and N. Kopell. The dynamic structure underlying subthreshold oscillatory activity and the onset of spikes in a model of medial entorhinal cortex stellate cells. *J. Comp. Neurosci.*, 21:271–292, 2006.

[76] E. M. Izhikevich. Hybrid spiking models. *Philos. Trans. R Soc A*, 368:5061–5070, 2010.

[77] E. M. Izhikevich. Simple model of spiking neurons. *IEEE Transactions of Neural Networks*, 14:1569–1572, 2003.

[78] C. D. Acker, N. Kopell, and J. A. White. Synchronization of strongly coupled excitatory neurons: Relating network behavior to biophysics. *J. Comp. Neurosci.*, 15:71–90, 2003.

[79] P. E. Latham, B. J. Richmond, P. G. Nelson, and S. Nirenberg. Intrinsic dynamics in neuronal networks. I. Theory. *J. Neurophysiol.*, 83:808–827, 2000.

[80] D. Hansel and G. Mato. Existence and stability of persistent states in large neuronal networks. *Phys. Rev. Lett.*, 86:4175–4178, 2001.

[81] H. G. Rotstein. Frequency preference response to oscillatory inputs in two-dimensional neural models: a geometric approach to subthreshold amplitude and phase resonance. *J. Math. Neurosci.*, 4:11, 2014.

[82] R. F. O. Pena and H. G. Rotstein. Oscillations and variability in neuronal systems: Interplay of autonomous transient dynamics and fast deterministic fluctuations. *J. Comp. Neurosci.*, 50:331–355, 2022.

[83] P. Pinsky and J. Rinzel. Intrinsic and network rhythmogenesis in a reduced Traub model of CA3 neurons. *J. Comp. Neurosci.*, 1:30–60, 1994.

[84] A. Kepecs, X.-J. Wang, and J. Lisman. Bursting neurons signal input slope. *J. Neurosci.*, 22:9053–9062, 2002.

[85] A. Kepecs, X.-J. Wang, and J. Lisman. Information encoding and computation with spikes and bursts. *Network: Computation in neural systems*, 14:103–118, 2003.

[86] R. L. Burden and J. D. Faires. *Numerical analysis*. PWS Publishing Company - Boston, 1980.

[87] H. G. Rotstein. Resonance modulation, annihilation and generation of antiresonance and antiphasonance in 3D neuronal systems: interplay of resonant and amplifying currents with slow dynamics. *J. Comp. Neurosci.*, 43:35–63, 2017.

[88] H. G. Rotstein. Subthreshold resonance and phasonance in single cells: 2D models. *In: Jaeger D., Jung R. (Ed.) Encyclopedia of Computational Neuroscience: SpringerReference (www.springerreference.com). Springer-Verlag, New York*, 2018.

[89] H. G. Rotstein. Subthreshold antiresonance and antiphasonance in single cells: 3D models. *In: Jaeger D., Jung R. (Ed.) Encyclopedia of Computational Neuroscience: SpringerReference (www.springerreference.com). Springer-Verlag, New York*, 2018.

[90] G. B. Ermentrout. Type I membranes, phase resetting curves, and synchrony. *Neural Comput.*, 8:979–1001, 1996.

[91] G. B. Ermentrout and N. Kopell. Parabolic bursting in an excitable system coupled with a slow oscillation. *SIAM J. Appl. Math.*, 46:233–253, 1986.

[92] M. Migliore and G. M. Shepherd. Emerging rules for the distributions of active dendritic conductances. *Nat. Rev. Neurosci.*, 3:362–370, 2002.

[93] H. G. Rotstein. Subthreshold amplitude and phase resonance in single cells. *In: Jaeger D., Jung R. (Ed.) Encyclopedia of Computational Neuroscience: SpringerReference (www.springerreference.com). Springer-Verlag, New York*, pages 1–12, 2014.

[94] J. Timofeeva, S. Coombes, and D. Michieleto. Gap junctions, dendrites and resonances: A recipe for tuning network dynamics. *J. Math. Neurosci.*, 3:15, 2013.

[95] E. Lowett, R. A. Mount, U. Chialva, R. F. O. Pena, S. Xiao, S. L. Zhou, D. J. Sheenan, H.-A. Tseng, H. Gritton, S. Shroff, K. Kondabolu, C. Cheung, J. Mertz, M. E. Hasselmo, H. G. Rotstein, and X. Han. Theta and gamma rhythmic coding through two spike output modes in the hippocampus during spatial navigation. *Cell Rep*, 42:112906, 2023.

[96] M. London and M. Hausser. Dendritic computation. *Annu. Rev. Neurosci.*, 28:503–532, 2005.

[97] P. Poirazi. Dendritic computation. *In: Jaeger, D., Jung, R. (eds) Encyclopedia of Computational Neuroscience. Springer, New York, NY.*, 2014.

[98] S. Li, N. Liu, X. Zhang, D. McLaughlin, D. W.and Zhou, and D. Cai. Dendritic computations captured by an effective point neuron model. *Proc. Natl. Acad. Sci. USA*, 116:15244–15252, 2019.

[99] S. Li, D. W. McLaughlin, and D. Zhou. Mathematical modeling and analysis of spatial neuron dynamics: Dendritic integration and beyond. *Commun. Pure Appl. Math*, 76:114–161, 2021.

[100] R. D. Cazé, M. Humphries, and B. S. Gutkin. Passive dendrites enable single neurons to compute linearly non-separable functions. *PLoS Comp. Biol.*, 9:e1002867, 2013.

[101] R. D. Cazé, A. Tran-Van-Minh, B. S. Gutkin, and D. A. DiGregorio. Demonstration that sublinear dendrites enable linearly non-separable computations. *Sci. Rep.*, 14:18226, 2024.

[102] A. Bel and H. G. Rotstein. Frequency-dependent communication of information in networks of non-oscillatory neurons in response to oscillatory inputs. *bioRxiv*, 2025.07.09.664007, 2025.

[103] R. J. Leiser and H. G. Rotstein. Emergence of localized patterns in globally coupled networks of relaxation oscillators with heterogeneous connectivity. *Phys. Rev. E.*, 96:022303, 2017.

[104] M. W. H. Remme, M. Lengyel, and B. S. Gutkin. A theoretical framework for the dynamics of multiple intrinsic oscillators in single neurons. *In Phase Response Curves in Neuroscience: Theory, Experiments and Analysis. N. W. Schultheiss, A. A. Prinz and R. A. Butera, Eds. (Springer)*, pages 53–72, 2012.

Supplementary Material

Frequency-dependent coupling in responses to oscillatory inputs in networks of electrically coupled nodes: Gap junction networks and spatially extended neurons

Andrea Bel Ulises Chialva and Horacio G. Rotstein

S1. Linearization and quadratization of conductance-based (biophysically plausible) models of Hodgkin-Huxley type

S2. Impedance amplitude and phase profiles for 2D linear systems: individual cells

S3. Network impedance profiles for linear systems: networks with linear nodes and connectivity

S4. Networks of electrically coupled weakly nonlinear (quasi-linear) cells: Stationary and frequency-dependent coupling coefficient

S5. Impedance amplitude and phase profiles for 2D linear systems: general calculation

S6. Additional Figures.

Part of the supplementary material has been used in other publications (e.g., [102, 103])

S1 Linearization and quadratization of conductance - based (biophysically plausible) models of Hodgkin-Huxley type

S1.1 Conductance-based models of single cells

We use the following biophysical (conductance-based) models of Hodgkin-Huxley type [69,73] to describe the neuronal subthreshold dynamics

$$C\,\frac{dV}{dt} = -I_L - \sum_j I_j + I_{app} + I_{in}(t), \tag{S1}$$

$$\frac{dx_j}{dt} = \frac{x_{j,\infty}(V) - x_j}{\tau_{j,x}(V)}, \qquad j = 1, 2. \tag{S2}$$

In the current-balance equation (S1), V is the membrane potential (mV), t is time (ms), C is the membrane capacitance (μF/cm^2), I_{app} is the applied bias (DC) current (μA/cm^2), $I_L = G_L\,(V - E_L)$ is the leak current, and $I_j = G_j\,x_j,(V - E_j)$ are generic expressions for ionic currents (with j an index) with maximal conductance G_j (mS/cm^2) and reversal potentials E_j (mV) respectively. The dynamics of the gating variables x_j obey the kinetic equations (S2) where $x_{j,\infty}(V)$ and $\tau_{j,x}(V)$ are the voltage-dependent activation/inactivation curves and time constants respectively. For simplicity, the generic ionic currents I_j we consider here are restricted to have a single gating variable x_j and to be linear in x_j. This is typically the case for persistent sodium (I_{Nap}), h- (hyperpolarization-activated, mixed-cation, inward; I_h), and slow-potassium (M-type) (I_{Ks}) currents (see Section S1.2). Our discussion and results can be easily adapted and generalized to include ionic currents having two gating variables [20, 87–89] raised to powers different from one such as T-type calcium and A-type potassium currents [1]. The input current $I_{in}(t)$ (μA/cm^2) in eq. (S1) has the form (5), $I_{in}(t) = A_{in}\,sin(\Omega\,t)$ with $\Omega = 2\,\pi\,f\,/\,1000$ (f is the input frequency in Hz).

Here we focus on 2D models describing the dynamics of V and the gating variable (x_1) associated to the ionic current I_1. Additional currents whose gating variables evolve on a very fast time scale (as compared to the other variables) can be included by using the adiabatic approximation $x_j = x_{j,\infty}(V)$. Here we include one such fast current $I_2 = G_2\,x_{2,\infty}(V)\,(V - E_2)$. Additional fast currents can be included without significantly changing the formalism used here.

S1.2 Two examples: I_{Nap} + I_h and I_{Nap} + I_{Ks} models in the subthreshold regime

The I_{Nap} + I_h and I_{Nap} + I_{Ks} models [66, 71] are adapted versions of the models presented in [75, 78] (see also [66,67,70–72]). The I_{Nap} + I_h involves the interaction between a persistent sodium ($I_{Nap} = I_2$) and a hyperpolarization -activated (or h-) ($I_h = I_1$) currents. The I_{Nap} + I_{Ks} model involves the interaction between a persistent sodium ($I_{Nap} = I_2$) and an M-type slow potassium ($I_{Ks} = I_1$) currents. The formulation of these currents is

$$I_{Nap} = G_p\,p_\infty(V)\,(V - E_{Na}) \tag{S3}$$

$$I_h = G_h\,r\,(V - E_h) \tag{S4}$$

and

$$I_{Ks} = G_q\,q\,(V - E_k) \tag{S5}$$

The activation and inactivation curves we used for these currents are given, respectively, by the following functions

$$p_\infty(V) = 1/(1 + e^{-(V+38)/6.5}), \tag{S6}$$

$$r_\infty(V) = 1/(1 + e^{(V+79.2)/9.78}), \tag{S7}$$

$$q_\infty(V) = 1/(1 + e^{-(V+40)/5.5}), \tag{S8}$$

that have the general form

$$x_\infty(V) = \left(1 + e^{\frac{V - V_{1/2}}{V_{slp}}}\right)^{-1}. \tag{S9}$$

Graphs of these functions are shown in Fig. S1 (see also [70], Fig. 1)).

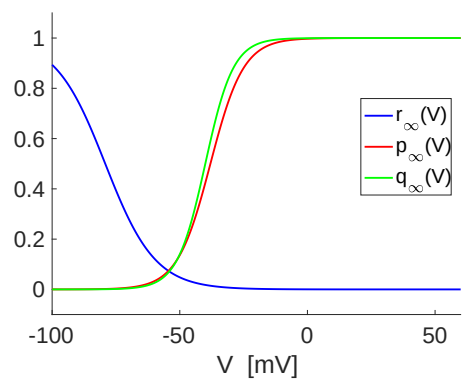

Figure S1: **Activation and inactivation curves for the I_{Nap} + I_h and I_{Nap} + I_{Ks} models.** We used eqs. (S6)-(S8) in Section S1.2.

S1.2.1 Parameter values for the $\mathbf{I_{Nap}}$ + $\mathbf{I_h}$ model

We used the following parameter values unless stated otherwise: $C = 1$, $E_L = -65$, $E_h = -20$, $E_{Na} = 55$, $G_L = 0.5$, $V_{p,1/2} = -38$, $V_{p,slp} = -65$, $V_{r,1/2} = -79.2$, $V_{r,slp} = 9.78$, $\tau_r = 100$, $G_p = 0.5$, $G_h = 1.5$, $I_{app} = -2.5$. The values of G_L, G_p, G_h and I_{app} are the baseline parameter values and were varied in our simulations.

For our calculations using the generic model (S1)-(S2), we used the following notation: $E_1 = E_h$, $E_2 = E_{Na}$, $G_1 = G_h$, $G_2 = G_p$, $V_{1,1/2} = V_{h,1/2}$, $V_{1,slp} = V_{h,slp}$, $V_{2,1/2} = V_{p,1/2}$, $V_{2,slp} = V_{p,slp}$, $\tau_1 = \tau_r$.

S1.2.2 Parameter values for the $\mathbf{I_{Nap}}$ + $\mathbf{I_{Ks}}$ model

We used the following parameter values: $C = 1$, $E_L = -54$, $E_K = -90$, $E_{Na} = 55$, $G_L = 0.1$, $V_{p,1/2} = -38$, $V_{p,slp} = -65$, $V_{q,1/2} = -40$, $V_{q,slp} = -5.5$, $\tau_q = 100$, $G_p = 0.21$, $G_q = 1$, $I_{app} = -0.6$. The values of G_L, G_p, G_q and I_{app} are the baseline parameter values and were varied in our simulations.

For our calculations using the generic model (S1)-(S2), we used the following notation: $E_1 = E_K$, $E_2 = E_{Na}$, $G_1 = G_q$, $G_2 = G_p$, $V_{1,1/2} = V_{q,1/2}$, $V_{1,slp} = V_{q,slp}$, $V_{2,1/2} = V_{p,1/2}$, $V_{2,slp} = V_{p,slp}$, $\tau_1 = \tau_q$.

S1.2.3 Parameter values for the $\mathbf{I_{Nap}}$ model

We used the following parameter values: $C = 1$, $E_L = -65$, $E_{Na} = 55$, $G_L = 0.1$, $V_{p,1/2} = -38$, $V_{p,slp} = -65$, $G_p = 0.1$, $I_{app} = 0$. The values of G_L, G_p, and I_{app} are the baseline parameter values and were varied in our simulations. Fig. S2 illustrates the dynamics for representative scenarios.

For our calculations using the generic model (S1)-(S2), we used the following notation: $E_2 = E_{Na}$, $G_2 = G_p$, $V_{2,1/2} = V_{p,1/2}$ and $V_{2,slp} = V_{p,slp}$.

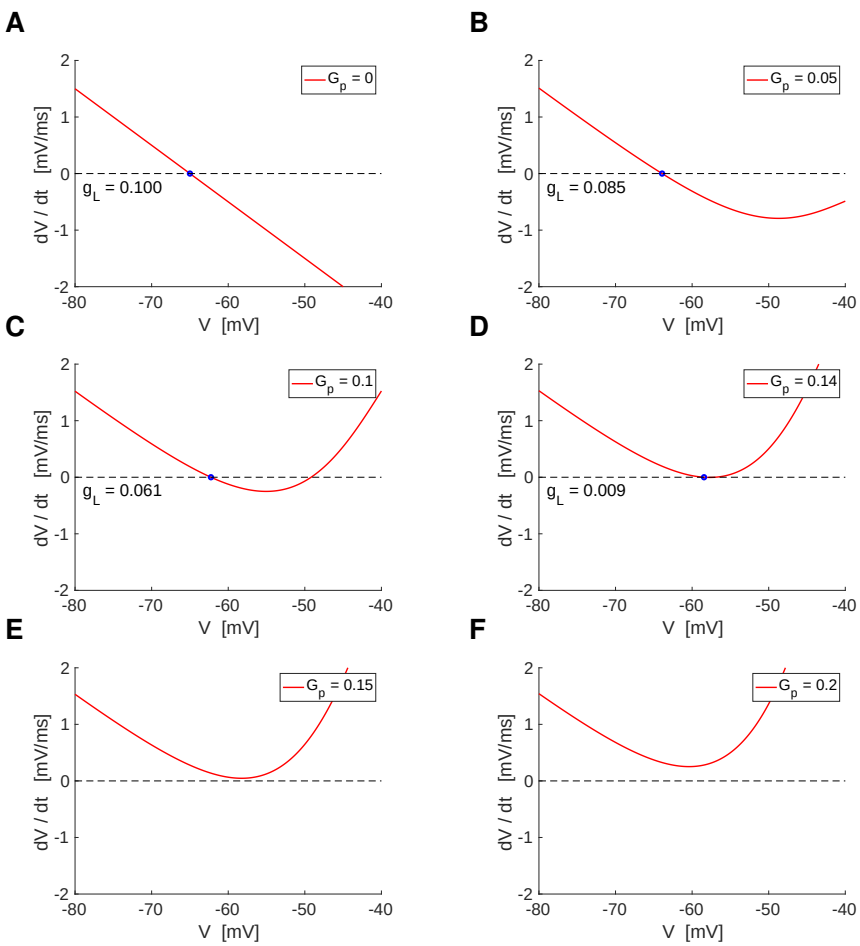

Figure S2: **Phase-space diagrams for the I_{Nap} model (subthreshold regime) for representative parameter values.** dV/dt vs. V curves for representative parameter values of G_p and G_L and $I_{app} = 0$. We used the parameter values presented in Section 4. This model can be thought of as a 1D reduced version of the 2D models illustrated in Fig. S6. See additional details there. The trajectories (not shown) move along the V axis and converge to the stable fixed points (blue dots) (A - D) or escape the subthreshold regime (E, F). For $G_p = 0$ the modes is a passive cell, which is linear (A) . As G_p increases, nonlinearities of parabolic type develop and become more pronounced in a vicinity of the stable fixed-point (B-D). The unstable fixed-point serves as a threshold for spike generation. If the model is supplemented with a return mechanism to the subthreshold regime, it becomes a model of quadratic integrate-and-fire type [72]. For the saddle-node bifurcation value of G_p, the fixed-points cease to exist (E, F). The associated quadratic integrate-and-fire model produces periodic spiking.

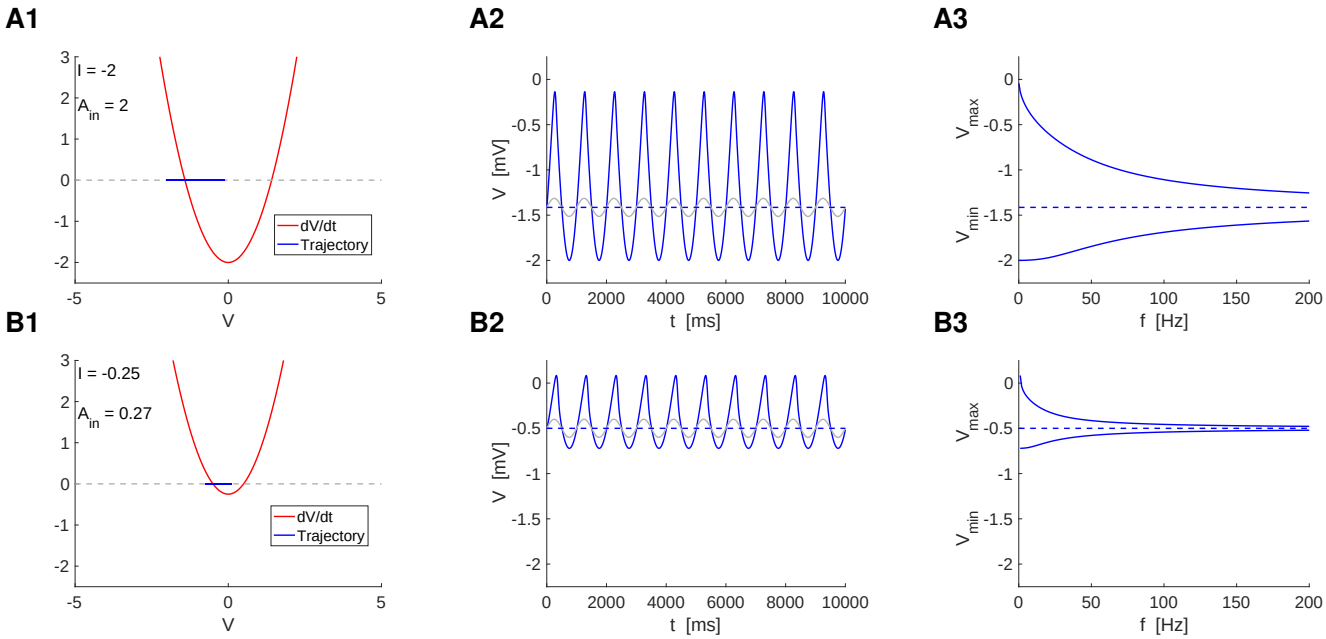

Figure S3: **Quadratic 1D model (subthreshold regime) for representative parameter values.** We used the model given by eq. (31) with $a = 1$, $\tau = 10$ and $g_c = 0$ (isolated cell). **Left column.** Phase-space diagrams: dV/dt vs. V curves (red) and voltage trajectory corresponding to the voltage trace in the middle column (blue). **Middle column.** Voltage trace (blue) in response to an oscillatory input of frequency equal to 1 and amplitude A_{in} (gray; the input signal is rescaled). The value of A_{in} is the threshold value above which v increases unboundedly (escapes the subthreshold regime). **Right column.** Voltage envelope profile in response to oscillatory inputs with the same amplitude as in the left and middle panels.

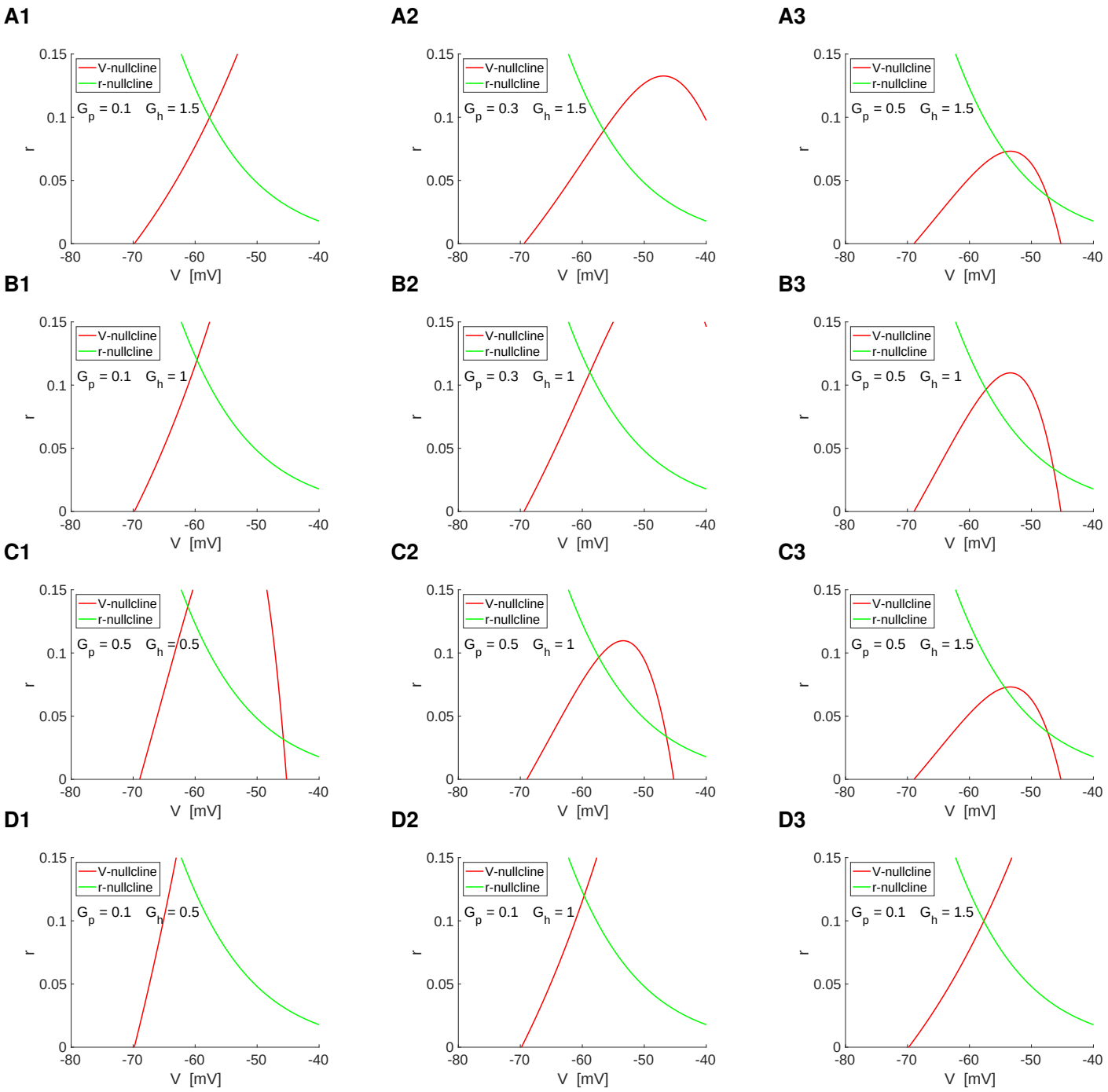

Figure S4: **Phase-space diagram for the $\mathbf{I_{Nap}}$+$\mathbf{I_h}$ model (subthreshold regime) for representative parameter values of the $\mathbf{I_{Nap}}$ and $\mathbf{I_h}$ maximal conductances.** The V- and r-nullclines were computed from eqs. (S1)-(S2) for the parameter values showed in each panel, $G_L = 0.5$, $I_{app} = -2.5$ and the remaining parameter values presented in Section S1.2. When there is a single fixed-point, it is stable. When there are two fixed-points, the one with the smaller value of V (left) is stable and the one with the larger values of V (right) is unstable. Trajectories (not shown) evolve towards the stable fixed-point (e.g., Fig. 3). **A.** Increasing values of G_p and $G_h = 1.5$. **B.** Increasing values of G_p and $G_h = 1$. **C.** Increasing values of G_h and $G_p = 0.5$. **C.** Increasing values of G_h and $G_p = 0.1$. **A, B, C.** The system transitions from quasi-linear (in a vicinity of the stable fixed-point) to parabolic-like. Increasing values of certain parameters (e.g., I_{app}, G_h, G_p) cause Hopf bifurcation where the fixed-point loses stability and moves to the "right branch" of the parabolic-like nullcline. Trajectories leaving the subthreshold regime is interpreted as the onset of a spike and if the model is supplemented with a return mechanism to the subthreshold regime, it becomes a model of quadratic integrate-and-fire type with adaptation [72, 74, 76]. **D.** The system remains quasi-linear.

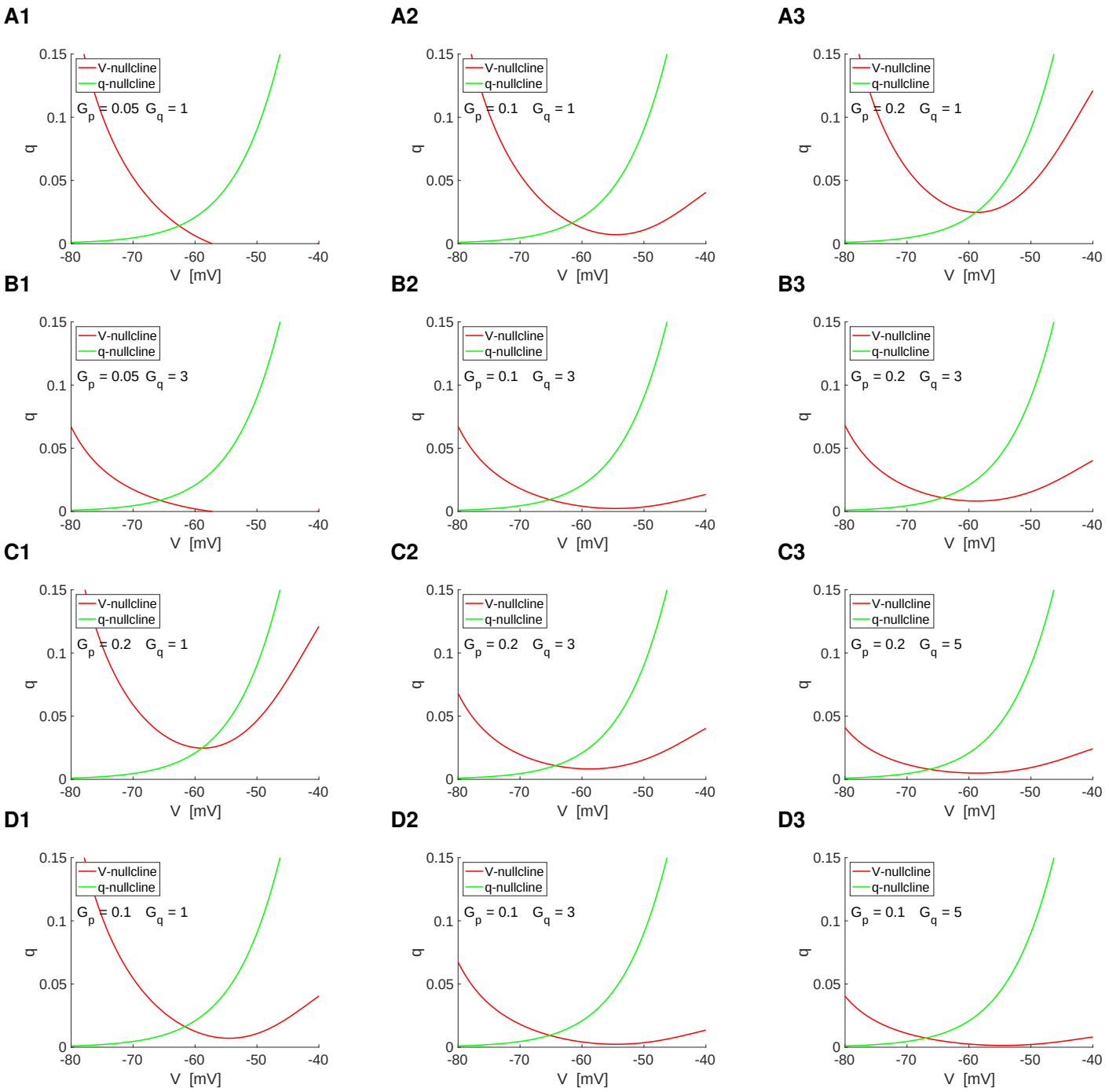

Figure S5: **Phase-space diagram for the $\mathbf{I_{Nap}}$+$\mathbf{I_{Ks}}$ model (subthreshold regime) for representative parameter values of the $\mathbf{I_{Nap}}$ and $\mathbf{I_{Ks}}$ maximal conductances.** The V- and q-nullclines were computed from eqs. (S1)-(S2) for the parameter values showed in each panel, $G_L = 0.5$, $I_{app} = -2.5$ and the remaining parameter values presented in Section S1.2. When there is a single fixed-point, it is stable. When there are two fixed-points, the one with the smaller value of V (left) is stable and the one with the larger values of V (right) is unstable. Trajectories (not shown) evolve towards the stable fixed-point (e.g., Fig. 3). **A.** Increasing values of G_p and $G_q = 1$. **B.** Increasing values of G_p and $G_q = 3$. **C.** Increasing values of G_q and $G_p = 0.2$. **C.** Increasing values of G_q and $G_p = 0.1$. **A, B.** The system transitions from quasi-linear (in a vicinity of the stable fixed-point) to parabolic-like. Increasing values of certain parameters (e.g., I_{app}, G_q, G_p) causes Hopf bifurcation where the fixed-point loses stability and moves to the "right branch" of the parabolic-like nullcline. Trajectories leaving the subthreshold regime is interpreted as the onset of a spike and if the model is supplemented with a return mechanism to the subthreshold regime, it becomes a model of quadratic integrate-and-fire type with adaptation [72, 74, 76]. **C, D.** The system transitions from parabolic-like to quasi-linear (in a vicinity of the stable fixed-point).

S1.2.4 Dynamic structure of the $\mathbf{I_{Nap}}$ + $\mathbf{I_h}$ and $\mathbf{I_{Nap}}$ + $\mathbf{I_{Ks}}$ models in the subthreshold regime with nonlinearities of quadratic type

The two models have V-nullclines of quadratic type in the subthreshold regime or are quasi-linear for the parameter sets considered (Figs. S4, and S6-A1 and -B1) (see also [70], Fig. 2, and [72], Fig. 7). However, while this is a rather general property of models of HH type having regenerative (amplifying) ionic currents (e.g., I_{Nap} or inward-rectifying potassium I_{Kir}) [66, 67, 74]), we note that in certain, also rather general parameter regimes, both models can have V-nullclines of cubic-type [66, 67, 104] around which, not around the parabolic component of the cubic-like nullcline relevant subthreshold behavior such as subthreshold oscillations are generated.

The I_{Nap} model, which can be thought of as a 1D reduced version of the 2D models discussed above has a parabolic-like dV/dt vs. V curve.

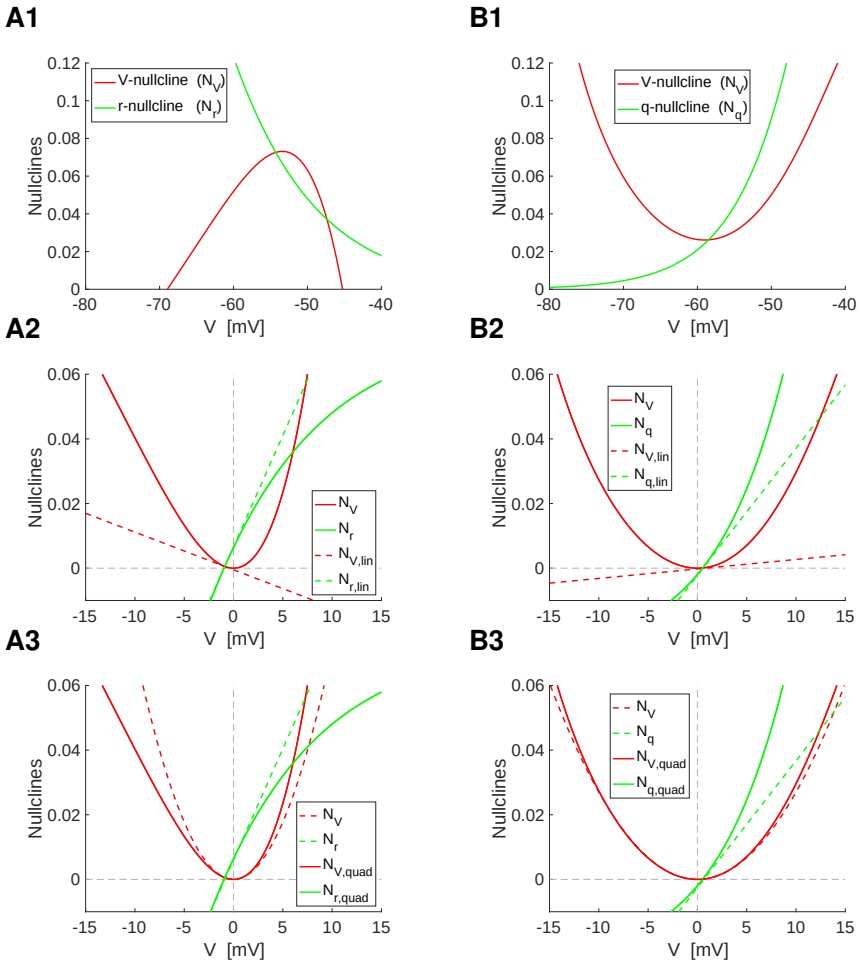

Figure S6: **Linearization and quadratization of the I_{Nap}+I_h and I_{Nap}+I_{Ks} models with voltage nonlinearities of parabolic type in the subthreshold regime. A.** I_{Nap}+I_h model. We used the parameter values presented in Section S1.2 **B.** I_{Nap}+I_{Ks}. We used the parameter values presented in Section 4. A detailed description of the process for 3D models of HH type including time-dependent external currents and synaptic inputs is presented in [70] and also discussed in [72] in the context of reduced neuronal models. We note that while the presence of voltage nonlinearities of parabolic type are a rather general property of models of HH type having regenerative (amplifying) ionic currents (e.g., I_{Nap} or inward-rectifying potassium I_{Kir}) [66, 67, 74]), in other, also rather general parameter regimes, both models can have V-nullclines of cubic-type [66, 67, 104] around which, not around the parabolic component of the cubic-like nullcline relevant subthreshold behavior such as subthreshold oscillations are generated.

S1.3 Linearization: conductance-based linearized models

Linearization of the autonomous part ($I_{in}(t) = 0$) of system (S1)-(S2) around the fixed-point $(\bar{V}, \bar{x}_1)$ yields [20, 21, 88]

$$C\,\frac{dv}{dt} = -g_L v - g_1 w_1 + I_{in}(t), \tag{S10}$$

$$\bar{\tau}_1 \frac{dw_1}{dt} = v - w_1, \tag{S11}$$

where

$$v = V - \bar{V}, \qquad w_1 = \frac{x_1 - \bar{x}_1}{x'_{1,\infty}(\bar{V})}, \tag{S12}$$

$$\bar{x}_1 = x_{1,\infty}(\bar{V}), \qquad \bar{\tau}_1 = \tau_{x,1}(\bar{V}), \tag{S13}$$

$$g_j = G_j\, x'_{j,\infty}(\bar{V})\,(\bar{V} - E_j), \qquad j = 1, 2, \tag{S14}$$

and

$$g_L = G_L + G_1\, x_{1,\infty}(\bar{V}) + G_2\, x_{2,\infty}(\bar{V}) + g_2. \tag{S15}$$

Note that the gating variables w_1 and w_2 in (S12) have units of voltage ($[v] = [w_1] =$V). A Comparison between the original (biophysical) I_{Nap} + I_h and I_{Nap} + I_{Ks} models and their linearization are presented in Figs. S6-A2 and -B2 (see also [72], Fig. 7).

The effective leak conductance g_L (S15) contains information about the biophysical leak conductance G_L, the ionic conductances, and their associated voltage-dependent activation / inactivation curves. The fast ionic current I_2 contributes to g_L with an additional term g_2. The signs of the effective ionic conductances g_j determine whether the associated gating variables are resonant ($g_j > 0$) or amplifying ($g_j < 0$) [1, 20]. Specific examples are the gating variables associated to I_h (resonant), I_{Ks} (resonant), I_{Nap} (amplifying) and I_{Kir} (amplifying). All terms in g_L are positive except for the last one that can be either positive or negative. Specifically, g_L can become negative for negative enough values of g_2.

All the linearized conductances are affected not only by the respective biophysical conductances, but also by the magnitudes and signs of the activation ($\sigma < 0$) and inactivation ($\sigma > 0$) curves and their derivatives, which are typically given by expressions of the form

$$x_\infty(V) = \left(1 + e^{\sigma\,\frac{V - V_{1/2}}{V_{slp}}}\right)^{-1} \tag{S16}$$

and

$$x'_\infty(V) = -\frac{\sigma}{V_{slp}}\,\left(1 + e^{\sigma\,\frac{V - V_{1/2}}{V_{slp}}}\right)^{-2}\, e^{\sigma\,\frac{V - V_{1/2}}{V_{slp}}} \tag{S17}$$

where $V_{1/2}$ and $V_{slp} > 0$ are constants (see the examples shown in Section S1.2).

S1.4 Quadratization: conductance-based linearized models

Quadratization of biophysically plausible models of HH type (S1)-(S2) extends the notion of linearization to include the parabolic-like properties of the V-nullcline in the subthreshold regime and therefore capture more realistic aspects of the dynamics of these models, which can be missed by the corresponding linearization [70–72]. In contrast to linearization, which is carried out around the model's fixed point (determined by the intersection of the model's nullclines), quadratization is done around the extremum (minimum or maximum) of the V-nullcline of quadratic type.

One important assumption is that the V-nullcline is parabolic-like in the subthreshold regime (e.g., Fig. 2 in [70] and Fig. 7 in [72]). This is a rather general property of neuronal models of HH type having regenerative (amplifying) ionic currents [66, 67, 74].

The process of quadratization [70, 71] consists of expanding the right-side of the model differential equations into Taylor series around the minimum/maximum (V_e, $x_{1,e}$) of the parabolic-like V-nullcline in the subthreshold regime, neglecting all the terms with power bigger than two in the equation for V and bigger than one in the equation for x_1, and translating the minimum/maximum of the V-nullcline to the origin. Details are provided in [70–72] for 2D and 3D models.

The quadratized 2D model (S1)-(S2) around (V_e,$x_{1,e}$) is given by

$$\frac{dv}{dt} = \sigma a v^2 - w, \tag{S18}$$

$$\frac{dw}{dt} = \epsilon\,[\,\alpha\, v - \lambda - w\,], \tag{S19}$$

where

$$v = V - V_e - \frac{g_L}{2\,\sigma\, g_c}, \tag{S20}$$

$$w = \frac{g_1}{C}\,\frac{x_1 - x_{1,e}}{x'_{1,\infty}(V_e)} - \frac{F_e}{C} + \frac{g_L^2}{4\,\sigma\, g_c\, C}, \tag{S21}$$

$$g_L = G_L + G_1\, x_{1,e} + G_2\, x_{2,\infty}(V_e) + g_2, \tag{S22}$$

$$g_j = G_j\,(V_e - E_j)\, x'_{j,\infty}(V_e), \qquad j = 1, 2 \tag{S23}$$

$$\sigma\, a = -\frac{G_2\, x''_{2,\infty}(V_e)\,(V_e - E_2) + 2\, G_2\, x'_{2,\infty}(V_e)}{2\, C}, \tag{S24}$$

$$\epsilon = \frac{1}{\tau_1}, \qquad \alpha = \frac{g_1}{C}, \qquad \beta = \frac{x_{1,\infty}(V_e) - x_{1,e}}{x'_{1,\infty}(V_e)}, \tag{S25}$$

$$\lambda = \frac{F_e}{C} - \frac{g_L^2}{4\,\sigma\, a\, C} - \frac{g_1\,\beta}{C} - \frac{g_1\, g_L}{2\,\sigma\, a\, C}, \tag{S26}$$

and

$$F_e = F(V_e, x_{1,e}) = I_{app} - G_L\,(V_e - E_L) -$$

$$-G_1\, x_{1,e}\,(V_e - E_1) - G_2\, x_{2,\infty}(V_e)\,(V_e - E_2). \tag{S27}$$

A Comparison between the original (biophysical) I_{Nap} + I_h and I_{Nap} + I_{Ks} models and their quadratization is presented in Figs. S6-A3 and -B3 (see also [72], Figs. 3 and 4). A detailed description of the process for 3D models of HH type including time-dependent external currents and synaptic inputs is presented in [70] and also discussed in [72] in the context of reduced neuronal models.

S2 Impedance amplitude and phase profiles for 2D linear systems: individual cells

For a linear system

$$C\,\frac{dv}{dt} = -g_L\,v - g\,w + I_{in}(t), \tag{S28}$$

$$\tau\,\frac{dw}{dt} = v - w, \tag{S29}$$

receiving a sinusoidal input current of the form (5)

$$I_{in}(t) = A_{in}\,\sin(\Omega\,t) \qquad \text{with} \qquad \Omega = \frac{2\pi f}{1000}, \tag{S30}$$

the voltage response is given by

$$V_{out}(t;f) = A_{out}(f)\,\sin\left(\Omega\,t - \Phi(f)\right) \tag{S31}$$

where $A_{out}(f)$ is the amplitude and $\Phi(f)$ is the phase-shift (or phase), which captures the difference between the peaks of $I_{in}(t)$ and $V_{out}(t;f)$ normalized by the period. For the linear system (S28)-(S29), the impedance is given by [20, 21, 88])

$$\mathbf{Z}(f) = \frac{A_{out}(f)}{A_{in}} = \frac{1 + i\,\tau\Omega}{(g_L + i\,C\Omega)(1 + i\,\tau\Omega) + g}. \tag{S32}$$

The Z- and Φ- profiles are given, respectively by

$$Z(f) = C\,\sqrt{\frac{1 + \tau^2\,\Omega^2}{(g_L + g - C\,\tau\,\Omega^2)^2 + (g_L\,\tau + C)^2\,\Omega^2}}, \tag{S33}$$

and

$$\Phi(f) = \tan^{-1}\left(\frac{C - \tau g + C(\tau\,\Omega)^2}{g_L + g + g_L(\tau\,\Omega)^2}\Omega\right). \tag{S34}$$

System (S28)-(S29) exhibits *resonance* (BPF) if $Z(f)$ peaks at a non-zero (resonant) frequency f_{res} (Figs. 1-A2) and *phasonance* if $\Phi(f)$ vanishes at a non-zero (phasonant) frequency f_{phas} (Figs. 1-C2).

From (S33), the resonant frequency is given by

$$f_{res} = \frac{1000}{2\,\pi\,\tau}\sqrt{-1 + \frac{\tau}{C}\,\sqrt{g^2 + 2\,g_L\,g + 2\,\frac{Cg}{\tau}}}, \tag{S35}$$

and the impedance peak Z_{max} is given by

$$Z_{max}^2 = Z^2(f_{res}) = \left(g_L^2 - \frac{1}{\tau^2} - 2\,\frac{g}{\tau} + \frac{2}{\tau}\,\sqrt{g^2 + 2g_L g + 2\frac{g}{\tau}}\,\right)^{-1}, \tag{S36}$$

where for simplicity we used $C = 1$. From (S34), the phasonant frequency is given by

$$f_{phas} = \frac{1000}{2\,\pi\,\tau}\sqrt{-1 + \frac{\tau g}{C}}. \tag{S37}$$

For passive (one-dimensional) cells ($g = 0$), the Z-profile reduces to a low-pass filter

$$Z(f) = \frac{C}{\sqrt{g_L^2 + C^2\,\Omega^2}} \tag{S38}$$

and the Φ-profile reduces to the positive increasing function

$$\Phi(f) = \tan^{-1}\left(\frac{C\,\Omega}{g_L}\right). \tag{S39}$$

The eigenvalues for the autonomous part of system (S28)-(S29) (no inputs) are given by

$$r_{1,2} = \frac{1}{2\,C\tau}\left(-(g_L\,\tau + C) \pm \sqrt{(g_L\,\tau - C)^2 - 4\,Cg\,\tau}\right), \tag{S40}$$

and the natural frequency, if it exists, is given by

$$f_{nat} = 4\,Cg\,\tau - (g_L\tau - C)^2 \tag{S41}$$

provided this quantity is positive.

S3 Network impedance profiles for linear systems: networks with linear nodes and connectivity

We consider networks consisting of N nodes with 2D linear dynamics and linear connectivity. The dynamics are described by

$$x_k' = a\,x_k + b\,y_k + \sum_{j=1}^{N} \Gamma_{kj}\,x_j + A_{in,k}\,e^{i\,\Omega\,t}, \tag{S42}$$

$$y_k' = c\,x_k + d\,y_k, \tag{S43}$$

for $k = 1, \ldots, N$. In (S42)-(S43), a, b, c and d are constant, $\Omega > 0$ is the input frequency and $A_{in,k} \geq 0$ are the input amplitudes. The connectivity coefficients Γ_{kj} indicate a connection from cell j to cell k. The coefficients a, b, c and d may be different in different nodes in the network. For simplicity in the notation we omit the subindex, which will be reintroduced later in the notation for the impedance profiles.

We use the notation $\mathbf{Z_k}(\Omega)$, $Z_k(\Omega)$ and $\Phi_k(\Omega)$ ($k = 1, \ldots, N$) to refer to the (complex) impedance, impedance amplitude (or simply, impedance) and phase profiles, respectively, of the individual nodes. The analytical expressions for 2D and 1D ($b = 0$) models are given in the Appendix S2.

The equation (S42) can be rewritten as

$$x_k' = \hat{a}\,x_k + b\,y_k + \sum_{j=1,\,j\neq k}^{N} \Gamma_{kj}\,x_j + A_{in,k}\,e^{i\,\Omega\,t}, \tag{S44}$$

for $k = 1, \ldots, N$ where $\hat{a} = a + \Gamma_{kk}$ includes the coefficient (Γ_{kk}) of the autonomous component of the coupling term ($\Gamma_{kk}\,x_k$). We use the notation $\hat{\mathbf{Z}}_\mathbf{k}(\Omega)$ to refer to the (extended) impedance profile of the individual nodes including this term; i.e., the impedance profiles of the system consisting of the autonomous component in (S44) and equation (S43). Similarly, $\hat{Z}_k(\Omega)$ and $\hat{\Phi}_k(\Omega)$ refer to the extended impedance amplitude and phase profiles of these systems, respectively.

The particular solution to system (S42)-(S43) has the form

$$x_k(t) = \mathbf{A_k}(\Omega)\,e^{i\,\Omega\,t} \qquad \text{and} \qquad y_k(t) = \mathbf{B_k}(\Omega)\,e^{i\,\Omega\,t} \tag{S45}$$

for $k = 1, \ldots, N$. Substituting (S45) into (S43)-(S44) and rearranging terms we obtain

$$\frac{(-\hat{a}\,+i\,\Omega)\,(-d+i\,\Omega) - b\,c}{(-d+i\,\Omega)}\,\mathbf{A_k}(\Omega) - \sum_{j=1,\,j\neq k}^{N} \Gamma_{kj}\,\mathbf{A_j}(\Omega) = A_{in,k} \tag{S46}$$

for $k = 1, \ldots, N$. From (S82) in the Appendix S2 with a substituted by $\hat{a}$ we obtain

$$\frac{1}{\hat{\mathbf{Z}}_\mathbf{k}(\Omega)}\,\mathbf{A_k}(\Omega) - \sum_{j=1,\,j\neq k}^{N} \Gamma_{kj}\,\mathbf{A_j}(\Omega) = A_{in,k} \tag{S47}$$

for $k = 1, \ldots, N$.

This is a complex linear system of algebraic equations that can be written in compact form as

$$\mathbf{J}(\Omega)\,\mathbf{A}(\Omega) = A_{in} \tag{S48}$$

where

$$\mathbf{J} = \begin{bmatrix} \hat{\mathbf{Z}}_1^{-1} & -\Gamma_{12} & \dots & -\Gamma_{1N} \\ -\Gamma_{21} & \hat{\mathbf{Z}}_2^{-1} & \dots & -\Gamma_{2N} \\ \vdots & \vdots & & \vdots \\ -\Gamma_{N1} & -\Gamma_{N2} & \dots & \hat{\mathbf{Z}}_N^{-1} \end{bmatrix}, \qquad \mathbf{A} = \begin{bmatrix} \mathbf{A_1} \\ \mathbf{A_2} \\ \vdots \\ \mathbf{A_N} \end{bmatrix} \qquad \text{and} \qquad A_{in} = \begin{bmatrix} A_{in,1} \\ A_{in,2} \\ \vdots \\ A_{in,N} \end{bmatrix}. \tag{S49}$$

Note that for simplicity the explicit dependence of $\mathbf{J}$ and $\mathbf{A}$ on Ω has been omitted in (S49).

The solution to (S48) is formally given by

$$\mathbf{A}(\Omega) = \mathbf{J}(\Omega)^{-1}\, A_{in}. \tag{S50}$$

In order to invert the complex matrix $\mathbf{J}(\Omega)$ one needs to express $\hat{\mathbf{Z}}_\mathbf{k}(\Omega) = \hat{Z}_k(\Omega)\, e^{i\hat{\Phi}_k}$ as $\hat{\mathbf{Z}}_\mathbf{k}(\Omega) = \hat{Z}_k(\Omega)\, \cos\hat{\Phi}(\Omega) + i\, \hat{Z}_k(\Omega)\, \sin\hat{\Phi}(\Omega)$ and $\mathbf{A_k}(\Omega) = A_{k,real}(\Omega) + i\, A_{k,imag}(\Omega)$. Alternatively, $\mathbf{A_k} = |A_k(\Omega)|\, e^{i\Psi(\Omega)} = |A_k(\Omega)| \cos\Psi(\Omega) + i|A_k(\Omega)| \sin\Psi(\Omega)$.

The vector $\mathbf{A}(\Omega)$ represents the response of the network to the oscillatory inputs. For a two-cell network ($N = 2$) we obtain

$$\mathbf{A}_1(\Omega) = \frac{A_{in,1} + \Gamma_{12}\, \hat{\mathbf{Z}}_2(\Omega)\, A_{in,2}}{1 - \Gamma_{12}\, \Gamma_{21}\, \hat{\mathbf{Z}}_1(\Omega)\, \hat{\mathbf{Z}}_2(\Omega)}\, \hat{\mathbf{Z}}_1(\Omega) \qquad \text{and} \qquad \mathbf{A}_2(\Omega) = \frac{\Gamma_{21}\, \hat{\mathbf{Z}}_1(\Omega)\, A_{in,1} + A_{in,2}}{1 - \Gamma_{12}\, \Gamma_{21}\, \hat{\mathbf{Z}}_1(\Omega)\, \hat{\mathbf{Z}}_2(\Omega)}\, \hat{\mathbf{Z}}_2(\Omega). \tag{S51}$$

In order to extend the concept of impedance to networks we need to find an appropriate normalization. In the impedance for the individual neurons, this normalization is given by the input amplitude. If the input arrives only to one node in the network, it is natural to choose this input amplitude as the normalization constant. Otherwise, one has to choose an appropriate one among the various input amplitudes. Here we choose the largest of all and we index the sequence of input amplitudes in decreasing order of magnitude. Thus, eq. (S50) reads

$$\mathbf{Z}_{ntwk} = \frac{\mathbf{A}(\Omega)}{A_{in,1}} = \mathbf{J}(\Omega)^{-1}\, \Sigma_{in} \tag{S52}$$

where $\Sigma_{in} = [1, \sigma_2, \dots, \sigma_N]^T$ with $\sigma_k = A_{in,k}/A_{in,1}$ ($k = 2, \dots, N$). For a two-cell network, we obtain eqs. (7)-(8).

Assuming we have chosen an appropriate normalization, we call the $Z_{ntwk,k}(\Omega)$ and $\Phi_{ntwk,k}(\Omega)$ ($k = 1, \dots, N$) the network impedance amplitude and phases, respectively. While one could conceive other, global measures of the voltage response, such as the addition of the responses of the two cells or the quotient between the two, the one we choose is the most informative for the purpose of this paper.

S3.1 Extended impedance

The extended $\hat{Z}$- and $\hat{\Phi}$- profiles are given, respectively by

$$\hat{Z}(f) = \hat{Z}(f; g_c) = C \sqrt{\frac{1 + \tau^2\, \Omega^2}{(g_L + g_c + g - C\, \tau\, \Omega^2)^2 + [(g_L + g_c)\, \tau + C\,]^2\, \Omega^2}}, \tag{S53}$$

and

$$\hat{\Phi}(f) = \hat{\Phi}(f; g_c) = \tan^{-1}\left[\frac{C - \tau g + C(\tau\, \Omega)^2}{g_L + g_c + g + (g_L + g_c)\, (\tau\, \Omega)^2}\Omega\right]. \tag{S54}$$

For passive (one-dimensional) cells ($g = 0$), the extended $\hat{Z}$- and $\hat{\Phi}$- profiles reduce to

$$\hat{Z}(f) = \hat{Z}(f; g_c) = \frac{C}{\sqrt{(g_L + g_c)^2 + C^2\, \Omega^2}} \tag{S55}$$

and the Φ-profile reduces to the positive increasing function

$$\hat{\Phi}(f) = \hat{Z}(f; g_c) = \tan^{-1}\left(\frac{C\,\Omega}{g_L + g_c}\right). \tag{S56}$$

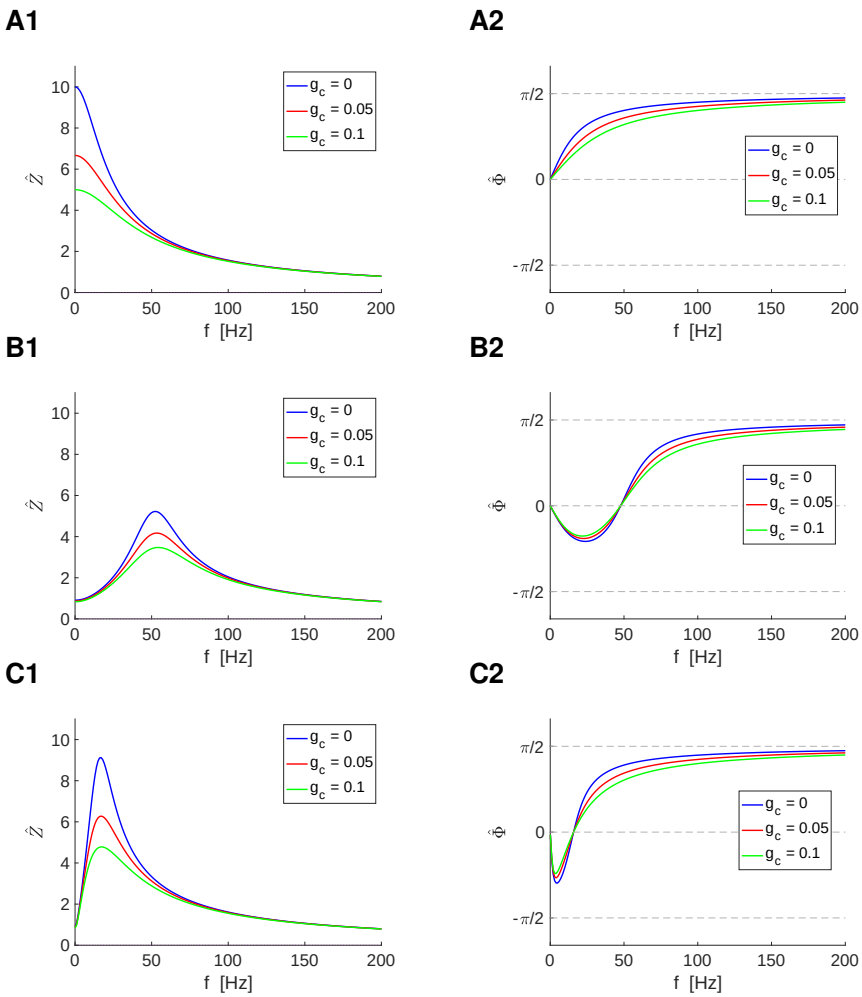

Figure S7: **Extended impedance $\hat{Z}(f, g_c)$ and phase $\hat{\Phi}(f, g_c)$ profiles.** We used eqs. (S53)-(S54). For $g = 0$, these eqs. reduce to eqs. (S55)- (S56). **Left columns.** Extended impedance profiles. **Right columns.** Extended phase profiles. **A.** $g = 0$. **B.** $g = 1$, $\tau = 10$. **C.** $g = 1$, $\tau = 100$. We used the additional parameter value: $g_L = 0.1$.

S3.2 Characteristic polynomial for a two-cell network

The characteristic polynomial for a two-cell network of the form (S42)-(S43) is given by

$$(r^2 - \Lambda_1\, r + \Delta_1)\,(r^2 - \Lambda_2\, r + \Delta_2) - \Gamma_{12}\Gamma_{21}\,(r - d_1)\,(r - d_2) = \tag{S57}$$

$$= r^4 - [\,\Lambda_1 + \Lambda_2\,]\, r^3 + [\,\Delta_1 + \Delta_2 + \Lambda_1\Lambda_2 - \Gamma_{12}\Gamma_{21}\,]\, r^2 - \tag{S58}$$

$$-[\,\Lambda_1\,\Delta_2 + \Lambda_2\,\Delta_1 - \Gamma_{12}\Gamma_{21}\,(d_1 + d_2)\,]\, r + \Delta_1\Delta_2 - \Gamma_{12}\Gamma_{21}\, d_1\, d_2 = 0 \tag{S59}$$

where

$$\Delta = \hat{a}\, d - b\, c, \qquad \text{and} \qquad \Lambda = a + d. \tag{S60}$$

For two-cell networks of 1D cells, the characteristic polynomial reduces to

$$r^2 - (a_1 + a_2)\, r + a_1 a_2 - \Gamma_{12}\Gamma_{21} \tag{S61}$$

S4 Networks of electrically coupled weakly nonlinear (quasi-linear) cells: Stationary and frequency-dependent coupling coefficient

The weakly nonlinear networks are an extension of the linear model (1)-(2) to include weak cellular nonlinearities in the current balance equation

$$C_k \frac{dv_k}{dt} = -g_{L,k}\, v_k - g_k\, w_k + \epsilon\, F_k(v_k, w_k) + g_c\,(v_j - v_k) + I_{in,k}(t), \tag{S62}$$

$$\tau_k \frac{dw_k}{dt} = v_k - w_k, \tag{S63}$$

for $k, j = 1, 2$ where $\epsilon \ll 1$. The functions F_k are arbitrary well-behaved functions.

S4.1 Response to constant inputs

The steady-state response of the quasi-linear system (S62)-(S63) to a constant (DC) inputs I_1 ($I_2 = 0$) can be written as

$$\bar{v}_1 = \bar{v}_{1,0} + \epsilon\, \bar{v}_{1,1} + \mathcal{O}(\epsilon^2) \qquad \text{and} \qquad \bar{v}_2 = \bar{v}_{2,0} + \epsilon\, \bar{v}_{2,1} + \mathcal{O}(\epsilon^2) \tag{S64}$$

where $\bar{v}_{1,0}$ and $\bar{v}_{2,0}$ are given by (S66) and (S67), respectively. The $\mathcal{O}(\epsilon)$ approximations are the solutions to

$$\begin{cases} (g_{L,1} + g_1 + g_c)\, \bar{v}_{1,1} - g_c\, \bar{v}_{2,1} = F(\bar{v}_{1,0}, \bar{w}_{1,0}) = \bar{F}_{1,0} \\ \\ -g_c\, \bar{v}_{1,1} + (g_{L,2} + g_2 + g_c)\, \bar{v}_{2,1} = F(\bar{v}_{2,0}, \bar{w}_{2,0}) = \bar{F}_{2,0} \end{cases} \tag{S65}$$

given by

$$\bar{v}_{1,1} = \frac{(g_{L,2} + g_2 + g_c)\, \bar{F}_{1,0} + g_c\, \bar{F}_{2,0}}{(g_{L,1} + g_1 + g_c)\,(g_{L,2} + g_2 + g_c) - g_c^2} \tag{S66}$$

and

$$\bar{v}_{2,1} = \frac{g_c\, \bar{F}_{1,0} + (g_{L,1} + g_1 + g_c)\, \bar{F}_{2,0}}{(g_{L,1} + g_1 + g_c)\,(g_{L,2} + g_2 + g_c) - g_c^2}. \tag{S67}$$

By substituting into (S64),

$$K = \frac{v_2}{v_1} = \frac{g_c\, I_1 + \epsilon\,[\, g_c\, \bar{F}_{1,0} + (g_{L,1} + g_1 + g_c)\, \bar{F}_{2,0}\,]}{(g_{L,2} + g_2 + g_c)\, I_1 + \epsilon\,[\, g_{L,2} + g_2 + g_c)\, \bar{F}_{1,0} + g_c\, \bar{F}_{2,0}\,]}. \tag{S68}$$

For linear models, K is independent of the input current and the intrinsic properties of the pre-J cell [43, 44] (see also Section 3.1.1). For networks of 2D linear cells, K is affected by $g_{L,2}$ and also by g_2, but it remains independent of the intrinsic properties of the pre-J cell (see Section 3.1.1). As the result of the presence of the nonlinearities ($\epsilon > 0$), K is no longer independent of I_1 and is affected by the intrinsic properties of both the pre- and post-J cells.

S4.2 Response to oscillatory inputs

The stationary solution of the quasi-linear system (S62)-(S63) to an oscillatory input current $I_1(t) = A_{in}\, e^{i\,\Omega\, t}$ to cell 1 (the pre-J cell) and no input to cell 2 (the post-J cell; $I_2 = 0$) can be written as

$$v_k(t) = v_{k,0}(t) + \epsilon\, v_{k,1}(t) + \mathcal{O}(\epsilon^2) = [\,\mathbf{A}_{k,0}(\Omega) + \epsilon\, \mathbf{A}_{k,1}(\Omega)\,]\, e^{i\,\Omega\, t} + \mathcal{O}(\epsilon^2) \tag{S69}$$

and

$$w_k(t) = w_{k,0}(t) + \epsilon\, w_{k,1}(t) + \mathcal{O}(\epsilon^2) = [\,\mathbf{B}_{k,0}(\Omega) + \mathbf{B}_{k,1}(\Omega)\,]\, e^{i\,\Omega\, t} + \mathcal{O}(\epsilon^2) \tag{S70}$$

for $k = 1, 2$, where

$$\mathbf{A}_{1,0}(\Omega) = \frac{1}{1 - g_c^2\, \hat{\mathbf{Z}}_{\mathbf{1}}^{\mathbf{0}}(\Omega)\, \hat{\mathbf{Z}}_{\mathbf{2}}^{\mathbf{0}}(\Omega)}\, \hat{\mathbf{Z}}_{\mathbf{1}}^{\mathbf{0}}(\Omega)\, A_{in} \tag{S71}$$

and

$$\mathbf{A}_{2,0}(\Omega) = \frac{g_c\, \hat{\mathbf{Z}}_{\mathbf{1}}^{\mathbf{0}}(\Omega)}{1 - g_c^2\, \hat{\mathbf{Z}}_{\mathbf{1}}^{\mathbf{0}}(\Omega)\, \hat{\mathbf{Z}}_{\mathbf{2}}^{\mathbf{0}}(\Omega)}\, \hat{\mathbf{Z}}_{\mathbf{2}}^{\mathbf{0}}(\Omega)\, A_{in}. \tag{S72}$$

and $\hat{\mathbf{Z}}_{\mathbf{k}}^{\mathbf{0}}(\Omega)$, $k = 1, 2$ are given by (9)-(11).

For simplicity, we assume that F_k is independent of w_k ($k = 1, 2$) and we expand

$$F_k(v_{k,0}) = \sum_{n=0}^{\infty} \alpha_{k,n}\, v_{k,0}^n = \sum_{n=0}^{\infty} \alpha_{k,n}\, [\mathbf{A}_{k,0}(\Omega)]^n\, e^{i\,n\,\Omega\, t}. \tag{S73}$$

The $\mathcal{O}(\epsilon)$ approximations are the stationary solutions of the following system

$$C_k\, \frac{dv_{k,1}}{dt} = -g_{L,k}\, v_{k,1} - g_k\, w_{k,1} + g_c\, (v_{j,1} - v_{k,1}) + \sum_{n=0}^{\infty} \alpha_{k,n}\, [\mathbf{A}_{k,0}(\Omega)]^n\, e^{i\,n\,\Omega\, t}, \tag{S74}$$

and

$$\tau_k\, \frac{dw_{k,1}}{dt} = v_{k,1} - w_{k,1}, \tag{S75}$$

for $k, j = 1, 2$. By solving this system, one obtains

$$v_{k,1}(t) = \sum_{n=0}^{\infty} \mathbf{A}_{k,1}(n\,\Omega)\, e^{i\,n\,\Omega\, t} \tag{S76}$$

where

$$\mathbf{A}_{1,1}(n\,\Omega) = \frac{\alpha_{1,n}\, [\mathbf{A}_{1,0}(\Omega)]^n + g_c\, \alpha_{2,n}\, [\mathbf{A}_{2,0}(\Omega)]^n\, \hat{\mathbf{Z}}_{\mathbf{2}}^{\mathbf{0}}(n\Omega)}{1 - g_c^2\, \hat{\mathbf{Z}}_{\mathbf{1}}^{\mathbf{0}}(n\Omega)\, \hat{\mathbf{Z}}_{\mathbf{2}}^{\mathbf{0}}(n\Omega)}\, \hat{\mathbf{Z}}_{\mathbf{1}}^{\mathbf{0}}(n\Omega) \tag{S77}$$

$$\mathbf{A}_{2,1}(n\,\Omega) = \frac{\alpha_{2,n}\, [\mathbf{A}_{2,0}(\Omega)]^n + g_c\, \alpha_{1,n}\, [\mathbf{A}_{1,0}(\Omega)]^n\, \hat{\mathbf{Z}}_{\mathbf{1}}^{\mathbf{0}}(n\Omega)}{1 - g_c^2\, \hat{\mathbf{Z}}_{\mathbf{1}}^{\mathbf{0}}(n\Omega)\, \hat{\mathbf{Z}}_{\mathbf{2}}^{\mathbf{0}}(n\Omega)}\, \hat{\mathbf{Z}}_{\mathbf{2}}^{\mathbf{0}}(n\Omega) \tag{S78}$$

for $n = 1, 2, \ldots$. The solution to the constant input term ($n = 0$) is provided in the previous section.

For linear networks, the frequency-dependent coupling coefficient is independent of the input current amplitude (A_{in}) and the intrinsic properties of the pre-J cell and only depends on g_c and the intrinsic properties of the post-J cell via its extended impedance. As the result of the presence of cellular nonlinearities, the coupling coefficient is no longer independent of the input amplitude A_{in} and is affected by the intrinsic properties of both the pre-J and post-J cells.

S5 Impedance amplitude and phase profiles for 2D linear systems: general calculation

In order to analytically compute the impedance amplitude and phase profiles for 2D linear systems motivated by neuronal models we use

$$\left\{ \begin{array}{l} x' = a\,x + b\,y + A_{in}\,e^{i\,\Omega\,t}, \\ y' = c\,x + d\,y \end{array} \right. \tag{S79}$$

where a, b, c and d are constant, $\Omega > 0$ and $A_{in} \geq 0$ is the input amplitude.

Impedance and phase profiles

The particular solution to system (S79) has the form

$$x_p(t) = A_{out}\,e^{i\,\Omega\,t} \qquad \text{and} \qquad y_p(t) = B_{out}\,e^{i\,\Omega\,t}. \tag{S80}$$

Substituting (S80) into (S79) and rearranging terms we obtain

$$\left((-a\,+i\,\Omega) - \frac{b\,c}{-d+i\,\Omega} \right) A_{out} = A_{in}. \tag{S81}$$

The impedance results

$$\mathbf{Z}(\Omega) = \frac{A_{out}}{A_{in}} = \frac{(-d+i\,\Omega)}{(-a\,+i\,\Omega)\,(-d+i\,\Omega)\,-b\,c}, \tag{S82}$$

which is a complex quantity with amplitude $|\mathbf{Z}(\Omega)|$ and phase $\Phi(f)$. For simplicity in the notation we use $Z(\Omega)$ for the impedance amplitude.

The impedance amplitude and phase are given, respectively, by

$$Z^2(\Omega) = \frac{d^2+\Omega^2}{(a\,d-b\,c-\Omega^2)^2+(a+d)^2\,\Omega^2} \tag{S83}$$

and

$$\Phi(\Omega) = \tan^{-1}\left(\frac{(a\,d-b\,c-\Omega^2)-(a+d)\,d}{(a\,d-b\,c-\Omega^2)\,d+(a+d)\,\Omega^2}\,\Omega \right). \tag{S84}$$

The resonance frequency, if it exists, is given by

$$\Omega_{res} = \sqrt{-d^2+\sqrt{b^2c^2-2\,a\,b\,c\,d-2\,d^2b\,c}}. \tag{S85}$$

Impedance and phase profiles: 1D linear systems

For 1D linear systems, by making $b=0$ in (S82) the impedance $\mathbf{Z}$ reduces to

$$\mathbf{Z}(\Omega) = \frac{1}{(-a\,+i\,\Omega)}. \tag{S86}$$

The impedance amplitude and phase are given, respectively, by

$$Z(\Omega) = \frac{1}{\sqrt{a^2+\Omega^2}} \qquad \text{and} \qquad \Phi(\Omega) = -\tan^{-1}\left(\frac{\Omega}{a}\right). \tag{S87}$$

Characteristic polynomial for the autonomous system

The characteristic polynomial for the corresponding homogeneous 2D system ($A_{in} = 0$) is given by

$$r^2 - (a + d)\, r + (a\, d - b\, c), \tag{S88}$$

and the roots are

$$r_{1,2} = \frac{(a + d) \pm \sqrt{(a - d)^2 + 4bc}}{2}. \tag{S89}$$

From the above equation, if $4bc + (a - d)^2 < 0$, the natural frequency of system (S79) is given by

$$\Omega_{nat} = \sqrt{\frac{-(a - d)^2}{2} - bc}. \tag{S90}$$

S6 Additional Figures

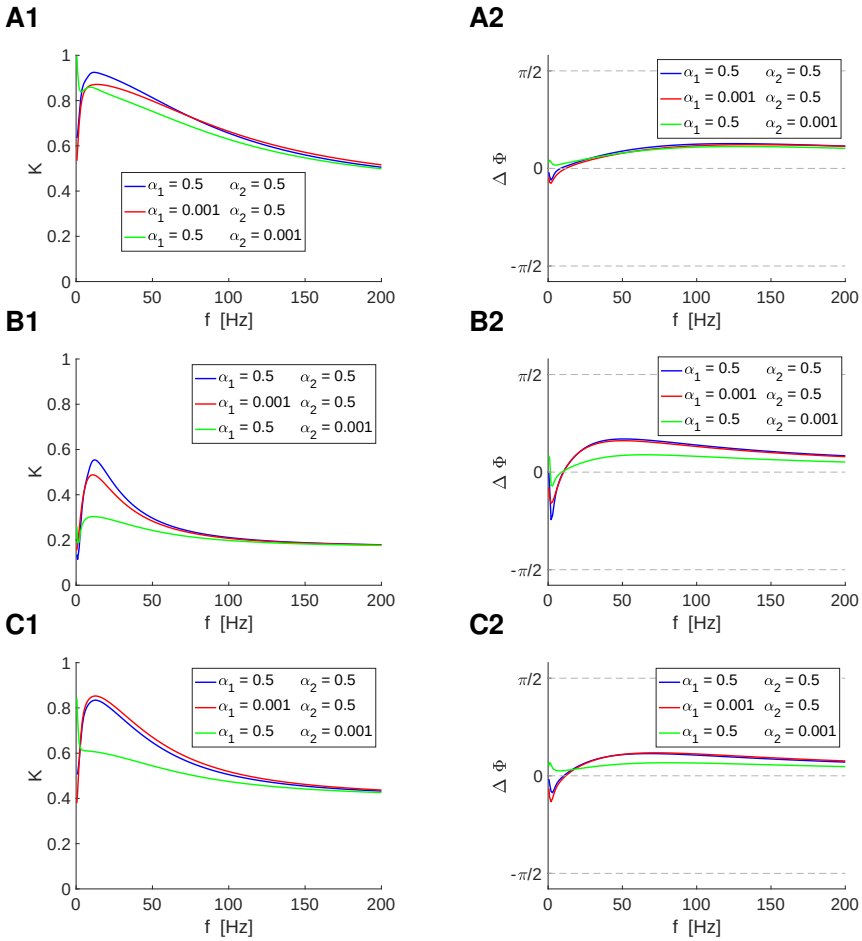

Figure S8: **Electrically coupled quadratic 2D model: Effects of the interplay of the biophysical properties of the pre-J and post-J cells and the dendritic geometry on the response profiles.** This figure is a rearrangement of Figs. 18-A, 16-A and 19-A to capture the effect of the dendritic geometry for fixed choices of the biophysical parameters. The description of the model is provided in the captions of these figures. We used $a_1 = a_2 = 0.1$, $\epsilon_1 = \epsilon_2 = 0.01$. **A.** Fig. 18-A ($\sigma = 0.2$). **B.** Fig. 16-A ($\sigma = 0.5$). **C.** Fig. 19-A ($\sigma = 0.8$).

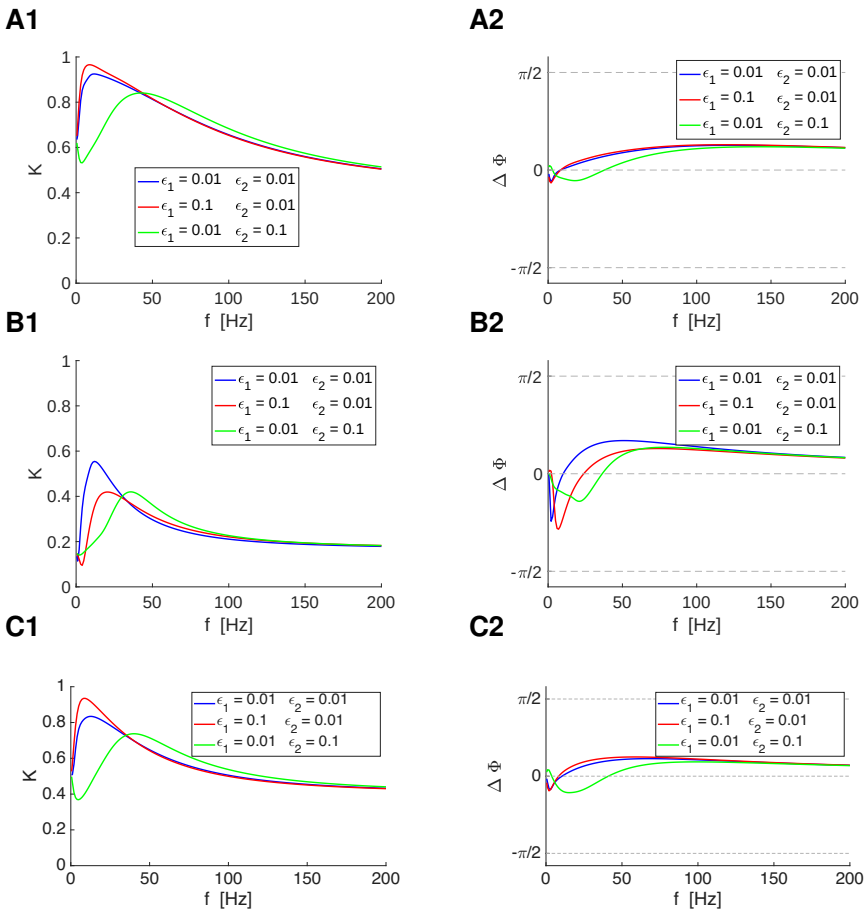

Figure S9: **Electrically coupled quadratic 2D model: Effects of the interplay of the biophysical properties of the pre-J and post-J cells and the dendritic geometry on the response profiles.** This figure is a rearrangement of Figs. 18-B, 16-B and 19-B to capture the effect of the dendritic geometry for fixed choices of the biophysical parameters. The description of the model is provided in the captions of these figures. We used $a_1 = a_2 = 0.1$, $\alpha_1 = \alpha_2 = 0.5$. **A.** Fig. 18-B ($\sigma = 0.2$). **B.** Fig. 16-B ($\sigma = 0.5$). **C.** Fig. 19-B ($\sigma = 0.8$).

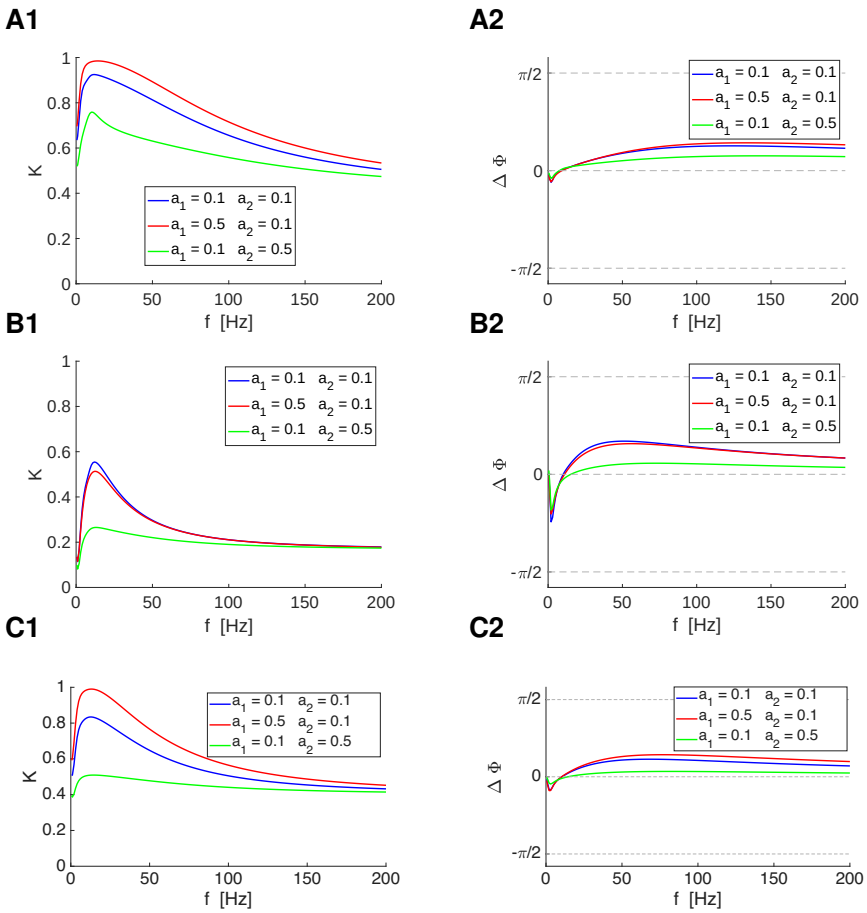

Figure S10: **Electrically coupled quadratic 2D model: Effects of the interplay of the biophysical properties of the pre-J and post-J cells and the dendritic geometry on the response profiles.** This figure is a rearrangement of Figs. 18-C, 16-C and 19-C to capture the effect of the dendritic geometry for fixed choices of the biophysical parameters. The description of the model is provided in the captions of these figures. We used $\alpha_1 = \alpha_2 = 0.5$, $\epsilon_1 = \epsilon_2 = 0.01$. **A.** Fig. 18-C ($\sigma = 0.2$). **B.** Fig. 16-C ($\sigma = 0.5$). **C.** Fig. 19-C ($\sigma = 0.8$). We used the following additional parameter values:, $\lambda_1 = \lambda_2 = -0.2$, $g_c = 0.05$, $A_{in,1} = 0.06$ and $A_{in,2} = 0$.